

## EDITORIAL BOARD

### Editor-in-Chief

I.V. Krivtsun E.O. Paton Electric Welding Institute, Kyiv, Ukraine

### Deputy Editor-in-Chief

S.V. Akhonin E.O. Paton Electric Welding Institute, Kyiv, Ukraine

### Deputy Editor-in-Chief

L.M. Lobanov E.O. Paton Electric Welding Institute, Kyiv, Ukraine

### Editorial Board Members

O.M. Berdnikova	E.O. Paton Electric Welding Institute, Kyiv, Ukraine
Chang Yunlong	School of Materials Science and Engineering, Shenyang University of Technology, Shenyang, China
V.V. Dmitrik	NTUU «Kharkiv Polytechnic Institute», Kharkiv, Ukraine
Dong Chunlin	China-Ukraine Institute of Welding of Guangdong Academy of Sciences, Guangzhou, China
M. Gasik	Aalto University Foundation, Finland
A. Gumenyuk	Bundesanstalt für Materialforschung und –prüfung (BAM), Berlin, Germany
V.V. Knysh	E.O. Paton Electric Welding Institute, Kyiv, Ukraine
V.M. Korzhyk	E.O. Paton Electric Welding Institute, Kyiv, Ukraine
V.V. Kvasnytskyi	NTUU «Igor Sikorsky Kyiv Polytechnic Institute», Kyiv, Ukraine
Yu.M. Lankin	E.O. Paton Electric Welding Institute, Kyiv, Ukraine
S.Yu. Maksymov	E.O. Paton Electric Welding Institute, Kyiv, Ukraine
Yupiter HP Manurung	Smart Manufacturing Research Institute, Universiti Teknologi MARA, Shah Alam, Malaysia
M.O. Pashchin	E.O. Paton Electric Welding Institute, Kyiv, Ukraine
Ya. Pilarczyk	Welding Institute, Gliwice, Poland
V.D. Poznyakov	E.O. Paton Electric Welding Institute, Kyiv, Ukraine
U. Reisgen	Welding and Joining Institute, Aachen, Germany
I.O. Ryabtsev	E.O. Paton Electric Welding Institute, Kyiv, Ukraine
V.M. Uchanin	Karpenko Physico-Mechanical Institute, Lviv, Ukraine
Yang Yongqiang	South China University of Technology, Guangzhou, China
<b>Executive Director</b>	O.T. Zelnichenko, International Association «Welding», Kyiv, Ukraine

### Address of Editorial Board

E.O. Paton Electric Welding Institute, 11 Kazymyr Malevych Str., 03150, Kyiv, Ukraine  
Tel./Fax: (38044) 205 23 90, E-mail: [journal@paton.kiev.ua](mailto:journal@paton.kiev.ua)  
<https://patonpublishinghouse.com/eng/journals/tpwj>

**State Registration Certificate** 24933-14873 ПП from 13.08.2021

ISSN 0957-798X, DOI: <http://dx.doi.org/10.37434/tpwj>

**Subscriptions**, 12 issues per year:

\$384 — annual subscription for the printed (hard copy) version, air postage and packaging included;

\$312 — annual subscription for the electronic version (sending issues in pdf format or providing access to IP addresses).

### Representative Office of «The Paton Welding Journal» in China:

China-Ukraine Institute of Welding, Guangdong Academy of Sciences

Address: Room 210, No. 363 Changxing Road, Tianhe, Guangzhou, 510650, China.

Zhang Yupeng, Tel: +86-20-61086791, E-mail: [patonjournal@gwi.gd.cn](mailto:patonjournal@gwi.gd.cn)

The content of the journal includes articles received from authors from around the world in the field of welding, metallurgy, material science and selectively includes translations into English of articles from the following journals, published in Ukrainian:

- Automatic Welding (<https://patonpublishinghouse.com/eng/journals/as>);
- Electrometallurgy Today (<https://patonpublishinghouse.com/eng/journals/sem>);
- Technical Diagnostics & Nondestructive Testing (<https://patonpublishinghouse.com/eng/journals/tdnk>).

## CONTENTS

### ORIGINAL ARTICLES

<b>V.V. Holovko, O.O. Shtofel, V.A. Kostin</b> FRACTAL EVALUATION OF GRAIN BOUNDARIES BRANCHING IN THE STRUCTURE OF WELD METAL OF LOW-ALLOY STEELS* .....	3
<b>A.Yu. Barvinko, Yu.P. Barvinko, A.M. Yashnyk</b> USE OF STRUCTURAL STEELS IN STORAGE TANK CONSTRUCTION AFTER NORMALIZED ROLLING* .....	8
<b>S.V. Akhonin, V.Yu. Bilous, R.V. Selin, V.V. Pashynskiy, S.L. Shvab</b> NARROW-GAP TIG WELDING OF THICK STEEL 20* .....	18
<b>N.V. Vihilianska, C. Senderowski, K.V. Yantsevych, O.I. Dukhota</b> PROPERTIES OF COATINGS PRODUCED BY HVOF SPRAYING OF COMPOSITE POWDERS BASED ON AMORPHIZING FeMoNiG13 ALLOY* .....	24
<b>O.V. Makhnenko, O.S. Milenin, O.F. Muzhychenko, S.M. Kandala, O.M. Savytska, G.Yu. Saprykina</b> MATHEMATICAL MODELING OF RESIDUAL STRESS RELAXATION DURING PERFORMANCE OF POSTWELD HEAT TREATMENT* .....	32
<b>V.O. Berezos, D.S. Akhonin</b> ELECTRON BEAM MELTING OF TITANIUM ALLOYS FOR MEDICAL PURPOSES** .....	41
<b>M.V. Iurzenko, M.O. Kovalchuk, V.Yu. Kondratenko, V.L. Demchenko, K.G. Guskova, V.S. Verbovskiy, G.V. Zhuk, K.P. Kostogryz, I.A. Gotsyk</b> INFLUENCE OF HYDROGEN-METHANE GAS MIXTURES ON THE PHYSICAL AND CHEMICAL STRUCTURE OF POLYETHYLENE PIPES OF THE OPERATING GAS-DISTRIBUTION NETWORKS OF UKRAINE*** .....	49

\*Translated Article(s) from "Automatic Welding", No. 6, 2023.

\*\*Translated Article(s) from "Electrometallurgy Today", No. 2, 2023.

\*\*\*Translated Article(s) from "Technical Diagnostics & Nondestructive Testing", No. 2, 2023.

DOI: <https://doi.org/10.37434/tpwj2023.06.01>

# FRACTAL EVALUATION OF GRAIN BOUNDARIES BRANCHING IN THE STRUCTURE OF WELD METAL OF LOW-ALLOY STEELS

**V.V. Holovko, O.O. Shtofel, V.A. Kostin**E.O. Paton Electric Welding Institute of the NASU  
11 Kazymyr Malevych Str., 03150, Kyiv, Ukraine**ABSTRACT**

Nonmetallic inclusions, which are an integral part of welds, can facilitate the reduction in the sizes of structural grains, playing the role of crystallization centers of the weld pool metal. This helps to increase the strength values of the weld metal on the one hand. On the other hand, the crystalline lattice of grains on the grain boundaries is influenced by the force fields of both tangent crystallites, saturated with nonmetallic inclusions, impurity atoms, dislocations, vacancies, has an increased energy of grain boundaries. These circumstances contribute to the fact that namely grain boundaries are the places of the highest probability of crack origination and propagation. For the numerical description of the dualism of the influence of nonmetallic inclusions on the weld metal structure, it is proposed to use methods of fractal analysis and metallographic analysis based on artificial intelligence.

**KEYWORDS:** low-alloy steel, welding, weld metal, microstructure, fractal analysis, metallographic analysis, MIPAR software

**INTRODUCTION**

The structure of steels used for manufacture of welded metal structures is characterized by a polycrystalline structure. In polycrystalline materials, grains or subgrains of different orientation and/or composition are separated from each other by interfaces (boundaries). Depending on the angle of inclination to each other, in the metal structure, small-angle (up to 15°) or large-angle (more than 60°) boundaries are determined. In some cases, when not all, but only individual boundary atoms coincide, the so-called “special” boundaries are formed. These “inner” interfaces play an important and most often dominant role in determination of mechanical properties of materials [1]. It is known that the main mechanical properties of the weld metal of low-alloy steels are tensile strength, ductility and fracture toughness, where grain refinement is a particularly important mechanism that provides the required level of properties. Branching of grain boundaries provides some advantages in terms of strength and fracture toughness, both at room and negative temperatures [2].

The crystalline structure of low-alloy steel consists of many individual crystallites connected with each other by grain boundaries. On these boundaries, the atomic structure of two connected crystalline lattices is strongly damaged, so grain boundaries usually have a high energy, which significantly affects the mechanical properties of the material. The impact of grain boundaries is the basis, for example, of the Hall–Petch ratio, which establishes the dependence of metal strength on grain size (the more branching of grain boundaries, the

stronger the metal), but they also determine the indices of their ductility and crack resistance.

$$\sigma_y = \sigma_0 + Kd^{-1/2}, \quad (1)$$

where  $\sigma_0$  is a certain friction stress required for sliding dislocations in the single-crystal;  $K$  is the constant individual for each material, which is also called “Hall–Petch ratio”;  $d$  is the grain size in the metal structure.

The whole technological process of welding steels is based on understanding the mechanisms of control of welded metal structure and structure parameters (sizes of grains, phases and inclusions) in the structure of welded joints metal. The more control is performed over this process, the higher level of their mechanical properties may be obtained.

There are two different categories of inner interfaces distinguished in crystalline materials: homophase boundaries and heterophase boundaries. The first are usually called grain boundaries, and the latter are often referred to as heterophase boundaries. Grain boundaries include boundaries of twins and domain boundaries. Heterophase boundaries, on the contrary, divide crystallites of two thermodynamically different phases. For heterophase boundaries, unlike grain boundaries, it is necessary to take into account their tendency to chemical reactions and diffusion processes. The behaviour of steels during fracture, for example, changes significantly as a result of segregation of certain impurities (especially sulphur, phosphorus) to the grain boundaries, which change adhesion between adjacent crystallites. If an increase in branching of grain boundaries is accompanied by improved strength values of metal, then the presence

of liquation elements and nonmetallic inclusions on the boundaries, as a rule, causes a decrease in its resistance against brittle fracture [2].

Moreover, to determine the degree of elements liquation along the grain boundaries and the binding energy of alloy boundaries is a difficult task. It is known that grain boundaries are a thin layer of about one nanometer thick with a low level of the orderly arranged atoms [3, 4], which divides two regions of the crystalline lattice with different orientation. During etching of the specimens of low-alloy steels, grain boundaries appear to be much wider, which indicates both the high level of dislocation density in these regions, as well as the presence of segregated elements and nonmetallic inclusions in these regions [5]. I.e., it seems that it is possible to establish a relation between the width of grain boundaries, the degree of their alloying and the energy of boundaries.

It is well known that branching of grain boundaries, on the one hand, as well as their clogging, on the other, significantly affect the mechanical properties of weld metal of low-alloy steels [6]. I.e., the properties of grain boundaries directly determine the properties of both the steels themselves as well as their welded joints, and the further studies of their structure suggest prospective opportunities for the development of new materials. The modern methods of metallographic examinations allow distinguishing the features of dualism of such an impact.

The aim of the work was to study the capabilities of a numerical description of grain boundaries that allows visualizing the dualistic nature of their structure.

## PROCEDURE AND RESEARCH MATERIALS

The studies were conducted on the specimens of weld metal, which were manufactured according to the procedure [3] in arc welding in shielding gas environment (82 % Ar, 18 % CO<sub>2</sub>) using flux-cored wire of 1.6 mm diameter of type «metalcore» at a direct current of  $200 \pm 5$  A, arc voltage of  $30 \pm 2$  V with input energy of  $21 \pm 2$  kJ/cm. To determine the nature of distribution of nonmetallic inclusions in the weld metal, to a “cold” part of the welding pool, a flux-cored wire of 1.6 mm diameter was introduced, the core of which contained a mixture with 10 % of particles of refractory compounds of 0.040–0.200 mm and 90 % of iron powder of grade PZhV according to DSTU 9849. As inoculants, the following titanium based compounds were selected: titanium oxide (TiO<sub>2</sub> weld), titanium carbide (TiC weld), titanium nitride (TiN weld), as well as aluminium oxide (Al<sub>2</sub>O<sub>3</sub> weld) and silicon carbide (SiC weld). The obtained results were compared with the data from the specimens of the weld metal, produced during welding using flux-cored wire, into the core of which ferrotitanium (Base weld) was introduced.

According to their physicochemical indices, non-metallic inclusions may affect the formation of grain structure in the process of metal cooling, playing the role of crystallization centers (TiN), microcoolants (TiO<sub>2</sub>) and phases that change energy at the crystallization front (Al<sub>2</sub>O<sub>3</sub>), or inhibit the carbon diffusion during decomposition of austenite (SiC, TiC). Accordingly, nonmetallic inclusions have a different effect on branching of grain boundaries in the structure of weld metal. The aim of the studies was to establish the possibilities of evaluating branching of grain boundaries of the metal matrix using the methods of fractal parametrization.

Metallographic examinations were performed on the transverse sections cut out from welded joints. The structure of the weld metal was examined in the optical microscope Neophot 32. Microstructure in the specimens was revealed by chemical etching in a 4 % alcohol solution of nitric acid. The specimens for examinations were made according to standard procedures using diamond pastes of different dispersion. The size of structural components was determined in accordance with GOST 5639.

The MIPAR (USA) v.4.2.1 software for image analysis was used to determine the structure parameters. The MIPAR software uses the technology of deep learning of artificial intelligence that allows teaching the software to adapt to the obtained microphotos, which are characterized by different contrast, brightness and texture features, as well as the technique of preparing specimens for examinations.

The latest versions of the MIPAR software (later than v.4.2) use a large library of procedures (recipe) to determine grain sizes, volumetric fraction and distribution of phases and inclusions, determination of orientation and heterogeneity of the structure, texture features, etc. The work used standard procedures (recipe) of the MIPAR software for determination of size and branching of grain boundaries in low-alloy steels.

## RESEARCH RESULTS

Table 1 shows the results of determining the chemical composition of the metal of the studied welds, and Table 3 shows the content of structural components in the specimens of the welds.

The data of optical microscopy showed that the secondary microstructure of the weld metal consists of a bainitic-martensitic mixture with a small fraction of the ferritic component (Figure 1). The composition of the secondary structure and the size of structural grains are given in Table 2. Bainite is represented by morphological shapes of upper, lower and intragranular bainite and ferrite by torn polygonal precipitates and Widmanstätten ferrite outside the grain boundaries. Martensite was formed as a traditional acicular structure.

**Table 1.** Chemical composition of weld metal

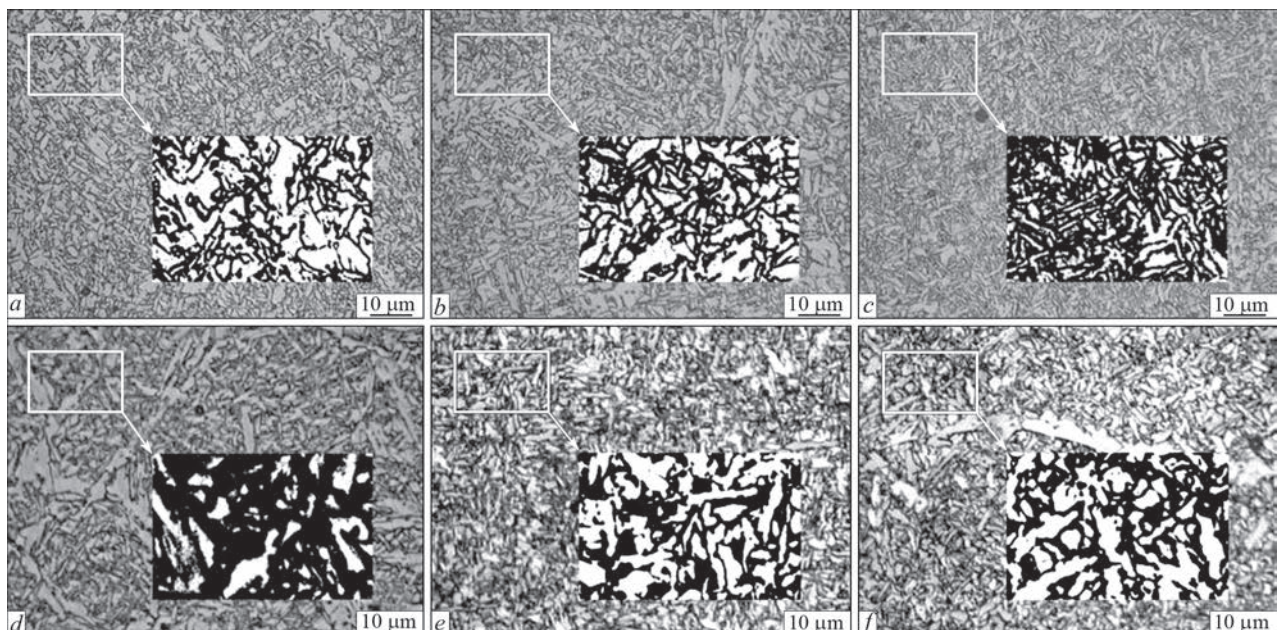
Weld	Chemical element, wt.%										
	C	Si	Mn	S	P	Cr	Ni	Mo	Cu	Al	Ti
Base	0.050	0.290	1.32	0.024	0.014	0.16	2.19	0.27	0.36	0.039	0.019
TiC	0.054	0.263	1.28	0.025	0.011	0.13	2.22	0.26	0.49	0.035	0.009
TiN	0.035	0.317	1.40	0.019	0.009	0.14	2.29	0.26	0.56	0.036	0.011
SiC	0.066	0.370	0.92	0.016	0.024	0.14	1.72	0.23	0.54	0.021	0.005
TiO <sub>2</sub>	0.035	0.405	1.24	0.016	0.021	0.11	1.97	0.27	0.72	0.032	0.015
Al <sub>2</sub> O <sub>3</sub>	0.034	0.424	1.40	0.017	0.023	0.12	2.15	0.29	0.60	0.023	0.030

**Table 2.** Composition of secondary structure of weld metal

Weld	Averaged fraction of components in the microstructure of welds, vol.%				Size of structural grains, $\mu\text{m}$
	Lower bainite	Upper bainite	Martensite	Ferrite	
Base	50	30	10	10	15 $\pm$ 1
TiN	30	57	10	3	15 $\pm$ 0.7
SiC	30	50	10	10	19 $\pm$ 1
TiO <sub>2</sub>	25	45	10	10	20 $\pm$ 1
Al <sub>2</sub> O <sub>3</sub>	15	50	15	15	16 $\pm$ 1
TiC	25	60	10	5	18 $\pm$ 1

For fractal analysis, five optical images of the secondary structure at a magnification  $\times 1000$  for each weld metal were selected (Figure 1). After processing with the use of the ImegeJ software, binary images of the corresponding structures (Figure 2) were obtained, for which the fractal parameter was determined. The results of fractal parameterization are given in Table 3.

The cell method was used to calculate fractal dimensions. [7]. According to this method, the prepared fractal image (Figure 1) is covered with grids of square cells (“box counting method”) with the grid step  $d$  scaled to  $1\text{px} = 0.0377\ \mu\text{m}$  and a number of cells  $N(d)$  is calculated, in which information boundary (grain boundary) of the investigated fractal object — structure was captured. The fractal dimensions of the image  $D$  are determined as a result of approx-


**Figure 1.** Microstructure of metal and binarized weld microstructure: *a* — base; *b* — SiC; *c* — TiN; *d* — TiC; *e* — TiO<sub>2</sub>; *f* — Al<sub>2</sub>O<sub>3</sub>

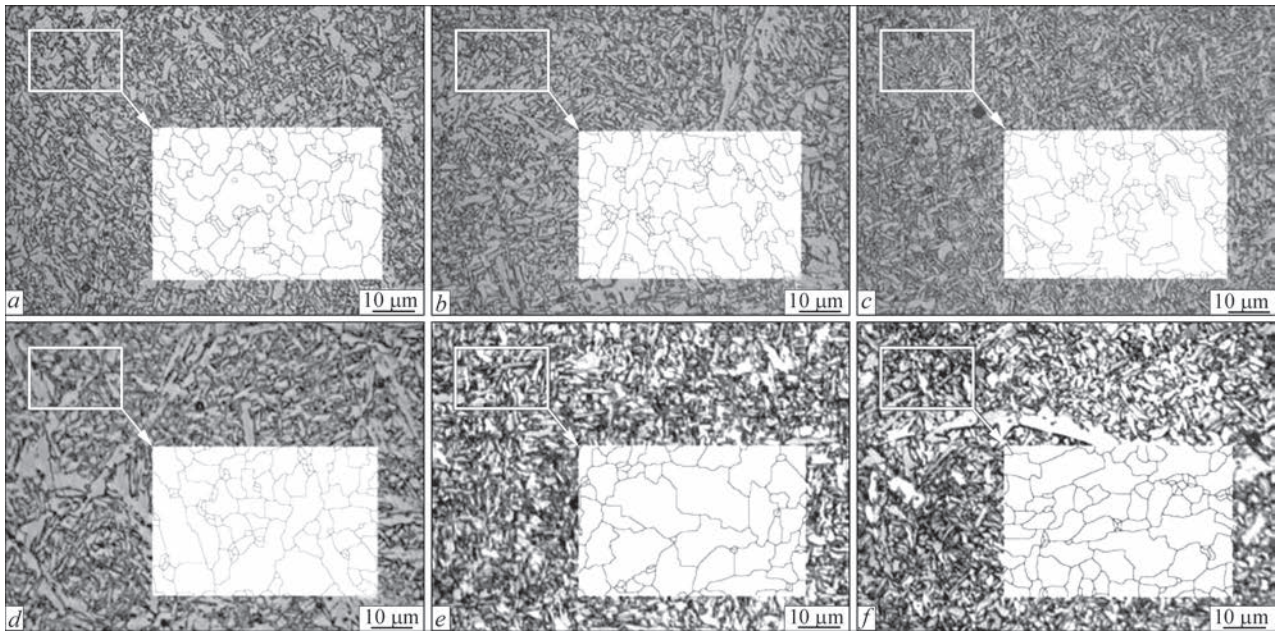


**Figure 2.** Microstructure and grain boundaries of weld metal modified by compounds: *a* — base; *b* — SiC; *c* — TiN; *d* — TiC; *e* — TiO<sub>2</sub>; *f* — Al<sub>2</sub>O<sub>3</sub>

imation of the obtained set of points using the least squares method according to the expression (2).

$$D = \lim_{d \rightarrow 0} \frac{\ln N(d)}{\ln \frac{1}{d}} \quad (2)$$

The results of the analysis of optical images of the metal structure of the studied welds according to the MIPAR software (Figure 2), which allowed determining the total length of grain boundaries, are given in (Table 4).

**DISCUSSION OF RESEARCH RESULTS**

The fractal parametrization of the structure is preceded by the binarization of its black and white images, which is based on the determination of a certain level of black colour as a carrier of information. Therefore, the images shown in Figure 1 should be considered as information grain boundaries. In the images, black colour shows the regions of metal corrosion of elevated intensity in the process of etching. Due to the fact that etching pits coin-

cide with the places of elevated concentration of dislocations and liquation elements, the highlighted boundaries can be considered as regions with an increased tendency to brittle fracture of the metal.

The MIPAR software detects “pure” idealized grain boundaries. The total length of grain boundaries calculated based on this software can be used to find the medium grain size (*d*) in the formula (1) to determine the values of metal strength.

The analysis of the obtained results showed (Figure 3) that there is a fairly simple dependence between the fractal parameter *D<sub>gb</sub>* of grain boundaries branching and the total length of grain boundaries *L<sub>gb</sub>* (correlation coefficient *R*<sup>2</sup> = 0.93), which can be described by a quadratic expression. I.e., at a relatively low level of the fractal parameter *D<sub>gb</sub>* ≤ 1.86, its change has almost no impact on the total perimeter of grain boundaries, whereas when approaching this parameter to *D<sub>gb</sub>* = 2.0, the total perimeter of boundaries increases sharply.

The results of the analysis shown in Figure 3, allow visualizing the dualism of the impact of nonmetallic in-

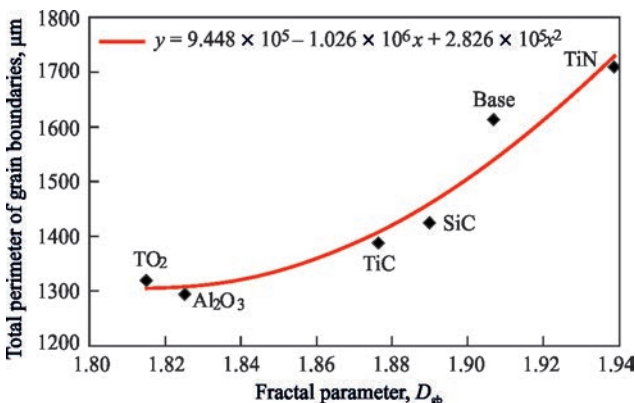


**Figure 3.** Impact of the fractal parameter on the total perimeter of grain boundaries

**Table 3.** Fractal parameter *D<sub>gb</sub>* of grain boundaries branching obtained as a result of analysis of optical images of weld metal structure

Weld	Base	SiC	TiN	TiC	TiO <sub>2</sub>	Al <sub>2</sub> O <sub>3</sub>
Fractal parameter ( <i>D<sub>gb</sub></i> )	1.9069	1.8916	1.9387	1.8765	1.8149	1.8252

**Table 4.** Total length of grain boundaries (*L<sub>gb</sub>*) in the regions of weld metal

Weld	Base	SiC	TiN	TiC	TiO <sub>2</sub>	Al <sub>2</sub> O <sub>3</sub>
<i>L<sub>gb</sub></i> , μm	16112.14	14226.94	17078.15	13893.75	13174.61	12949.53

clusions on the indices of grain boundaries in the structure of weld metal. Thus, for example, during inoculation of  $\text{TiO}_2$  and  $\text{Al}_2\text{O}_3$  particles to the welding pool, both the total perimeter of the boundaries, as well as the size of the region with an increased tendency to brittle fracture are noticeably reduced compared to the Base variant. The introduction of TiN particles to the welding pool leads to an increase in these two indices relative to the Base variant. The presence of SiC and TiC particles in the welding pool make it possible to raise the index  $L_{\text{gb}}$  without a significant growth in the index  $D_{\text{gb}}$ .

Thus, the given example of the system analysis indicates the possibility of expanding the knowledge base on the features of the impact of nonmetallic inclusions on grain boundaries in the structure of weld metal and making a more reasonable choice of welding consumables in the manufacture of metal structures of high-strength low-alloy steels.

## CONCLUSIONS

The studies on the visualization of the dualism of the influence of nonmetallic inclusions on the indices of grain boundaries in the structure of weld metal of low-alloy steels were carried out. To analyze the impact of nonmetallic inclusions  $\text{TiO}_2$ , TiC, TiN, SiC,  $\text{Al}_2\text{O}_3$  and  $\text{TiO}_2$ , the procedure of fractal analysis and the MIPAR software were involved. As a result of the conducted investigations, it was found that:

1. Involvement of the MIPAR software for analyzing optical images of the structure allows carrying out a numerical description of boundaries of structural grains by setting the value of the total perimeter of boundaries  $L_{\text{gb}}$ .

2. The methods of fractal analysis can be used to perform a numerical description of grain boundaries through the fractal parameter  $D_{\text{gb}}$ .

3. Parameter  $L_{\text{gb}}$  describes the idealized (“pure”) size of grain boundaries.

4. Parameter  $D_{\text{gb}}$  describes information grain boundaries.

5. The system analysis of indices  $L_{\text{gb}}$  and  $D_{\text{gb}}$  allows expanding the idea of dualism of the influence of non-metallic inclusions on the structure of grain boundaries.

## REFERENCES

1. Priester, L. (2012) *Grain Boundaries: From Theory to Engineering*. Springer Science & Business Media, Dordrecht.
2. Reiser, J., Hartmaier, A. (2020) Elucidating the dual role of grain boundaries as dislocation sources and obstacles and its impact on toughness and brittle-to-ductile transition. *Scientific Reports*, **10**, 2739.
3. Sinha, S., Kim, D-I., Fleury, E. et al. (2015) Effect of grain boundary engineering on the microstructure and mechanical properties of copper containing austenitic steel. *Mater. Sci. Eng.*, **626**, 175–185.
4. Zhang, I., Lu, C., Tieu, K. (2016) A review on atomistic simulation of grain boundary behaviors in face-centered cubic metals. *Computer Mater. Sci.*, **118**, 180–191.
5. Pogrebna, N.E., Kutsova, V.Z., Kotova, T.V. (2021) *Mechanical stability of materials: Tutorial*. Dnipro, NmetAU [in Ukrainian].
6. Vasyliiev, O.D., Brodnikovska, I.V., Brodnikovskiyi, Ie.M. et al. (2018) Interfaces and their influence on properties of polycrystals. Pt 1 (Review). *Metaloznavstvo ta Obrobka Metaliv*, **1**, 44–51 [in Ukrainian].
7. Usov, V.V., Rakkina, M.D., Shkatulyak, N.M. et al. (2014) Fractal dimension of grain boundaries and mechanical properties of oxygen containers. *Fiz.-Khimich. Mekhanika Materialiv*, **4**, 117–124 [in Ukrainian].

## ORCID

V.V. Holovko: 0000-0002-2117-0864,  
O.O. Shtofel: 0000-0003-0965-6340

## CONFLICT OF INTEREST

The Authors declare no conflict of interest

## CORRESPONDING AUTHOR

V.V. Holovko

E.O. Paton Electric Welding Institute of the NASU  
11 Kazymyr Malevych Str., 03150, Kyiv, Ukraine.

E-mail: v\_golovko@ukr.net

## SUGGESTED CITATION

V.V. Holovko, O.O. Shtofel, V.A. Kostin (2023) Fractal evaluation of grain boundaries branching in the structure of weld metal of low-alloy steels. *The Paton Welding J.*, **6**, 3–7.

## JOURNAL HOME PAGE

<https://patonpublishinghouse.com/eng/journals/tpwj>

Received: 31.05.2023  
Accepted: 17.07.2023

### Save the Date!



“SCHWEISSEN & SCHNEIDEN”, the world’s leading international trade fair for joining, cutting, and surfacing, will take place on September 11–15, 2023 at the Messe Essen Conference Center.



Visit Paton Welding Institute in Hall 8 at Stand 8B29.1 and check out our new and proven solutions for welding and allied technologies.

DOI: <https://doi.org/10.37434/tpwj2023.06.02>

# USE OF STRUCTURAL STEELS IN STORAGE TANK CONSTRUCTION AFTER NORMALIZED ROLLING

**A.Yu. Barvinko, Yu.P. Barvinko, A.M. Yashnyk**

E.O. Paton Electric Welding Institute of the NASU  
11 Kazymyr Malevych Str., 03150, Kyiv, Ukraine

## ABSTRACT

The work investigates the structure and ductility of sheet rolled steels of the strength class 355 and 420 in the plane  $X$ - $Y$ . It is shown that the use of normalized rolling does not provide sheet rolled steel S355+N the state, which is equivalent to the state after normalization. As a result of carrying out normalized rolling, due to the additional compression of the sheet in the temperature region near the temperature  $A_{c3}$ , a banded structure is formed in steel, which has a high anisotropy of mechanical properties. The formation of such a fibrous structure leads to a brittle state of the metal in the plane  $X$ - $Y$  at a calculation temperature. To prevent brittle layered fracture, it is necessary to use structural steels of the strength class S355 and S420, produced in accordance with the standard DSTU EN 10025-3:2007 in a state after normalization and limit the content of sulphur  $S \leq 0.10$  %. In the case of using the mentioned steels in the state after normalized rolling, it is recommended to use a metal with a thickness of not more than 15 mm, which will provide a safe service of a metal in welded assemblies over the direction of thickness. An additional criterion for stability of sheet rolled steels S355 and S420 to the brittle layered fracture, in addition to the rolled metal Z quality group, it is proposed to use such an indice as impact work, which is determined on the specimens with a V-shaped notch in the rolling plane  $X$ - $Y$  (along the sheet axis).

**KEYWORDS:** structural steels of strength class 355 and 420, normalized rolling, brittle layered fracture, vertical cylindrical steel tanks

## INTRODUCTION

Due to the transition of the construction industry on using structural steels, which are manufactured in accordance with the standards DSTU EN 10025, the problem of compliance of the mechanical properties of these steels and their welded joints with the requirements of the current regulatory framework of Ukraine is relevant. Traditionally, in Ukraine for welded metal structures, a carbon steel St3sp5-zv [1] (strength class S255) and a low-alloy steel 09G2S-12 [2] (strength class S325 at a thickness  $10 \leq t \leq 20$  mm) were used, which were delivered in a hot-rolled state or after normalization. The mentioned steels have a high ductility, a sufficient level of cold resistance and a good weldability, which led to their widespread use in critical structures [3], in particular, for vertical cylindrical tanks [4]. Structural steels, according to DSTU EN 10025-2-S355J2+N [5], DSTU EN 10025-S-355N(NL)) [6] and DSTU EN 10025-3-S420N(NL) [6], refer to a higher strength class and quite often are delivered after normalized rolling. The peculiarity of the mentioned steels is their production by metallurgical plants with a low content of sulphur:  $S \leq 0.010$  % and phosphorus:  $P \leq 0.015$  %, which should provide their high cold resistance [3].

The standards [5, 6] indicate that the state of steel after normalized rolling is equivalent to the state after normalization. At the same time, the works [7–9] note

that unlike normalization, in the process of normalized rolling at the final stage, an additional metal deformation is performed in the austenitic zone at values of temperature close to the point  $A_{c3}$ , which at sufficient compression allows obtaining a fine-grained structure due to a multiple full recrystallization [9]. In this case, additional deformation should lead to greater structural heterogeneity compared to the normalized state and, accordingly, to greater anisotropy of mechanical properties of the metal [10]. From this point of view, it is appropriate to carry out additional studies of the properties of sheet rolled steels made in accordance with DSTU EN [5, 6] in a state of normalized rolling, which are widely used in construction in order to take into account their features. In the case of vertical cylindrical tanks, it is necessary to take into account the work of the metal in the direction of thickness ( $Z$ -direction), which occurs in welding-in branch-pipes (overlapped welded joint, which reinforces the sheet-wall; T-joint by welding-on the wall to the branch-pipe) and in the assembly of the joint “wall-contour sheets of the bottom”. In order to prevent the emergence of a layered metal fracture, postweld heat treatment (PWHT) is carried out to remove welding residual stresses in places of welding-in branch-pipes and hatches into the wall in order to offset their influence during the metal work in the direction of thickness [11–13]. The conditions under which it is necessary to carry out PWHT of places of welding-in branch-

**Table 1.** Standard requirements for carrying out postweld heat treatment (PWHT) of places of cutting-in of branch-pipes and hatches into the wall of vertical cylindrical tanks

Design standard	Grade of steel	Thickness of the girth, mm	Diameter of the branch-pipe, mm
API 650-13 [11]	S235	$t > 25$	$\geq 300$
	S275J0; S355J0; S355(J2 а6о K2); A841M, grade A, class 1, 2 (ReH $\geq 461$ MPa)	$t > 13$	$\geq 50$
EN 14015 [12]	S275; S355	$t > 25$	$\geq 300$
	S420	$t > 20$	All diameters
DSTU B V.2.6-183:2011 [13]	ReH $\geq 345$ MPa	$t > 25$	$\geq 300$

Notes. 1. In table the requirements for an incomplete list of steel grades are provided. 2. ReH is the minimum guaranteed yield strength.

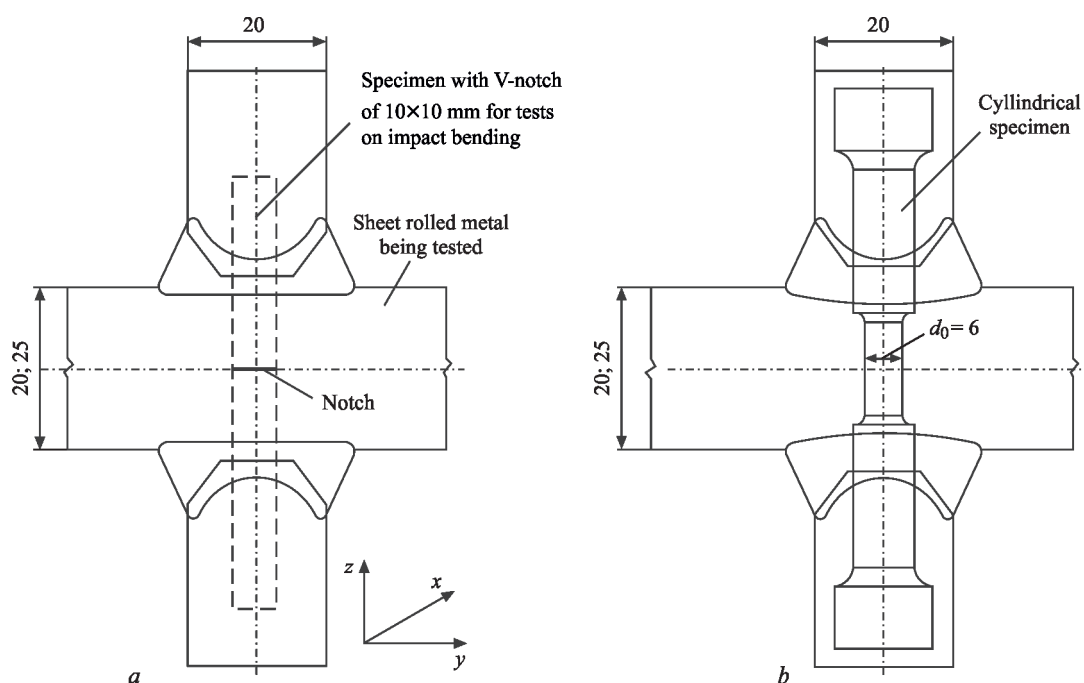
pipes in the wall differ significantly depending on the design standard (Table 1).

The data analysis given in Table 1 shows that there is no single approach to solving the problem of selecting the conditions, under which it is necessary to carry out PWHT. The main factors affecting the need for its conducting are the strength class of steel and the hole diameter. The most rigid requirements are specified in the standard API 650-13 [11]: for the steel of strength class S275J0 and more than the thickness of the sheet  $t \geq 13$  mm, PWHT is already required. In the standard EN 14015 [12]: for the steels S275 and S355 at a thickness  $t \geq 25$  mm, and for the steel of strength class S420 at a thickness  $t \geq 20$  mm. The least rigid requirements are contained in the domestic standard DSTU B V.2.6-183:2011 [13], which requires carrying out additional studies for the conditions of PWHT treatment.

One of the criteria for the quality of sheet rolled metal and its resistance to layered fracture, which has

become widespread in practice, is its guaranteed compliance with the quality class Z15, Z25, Z35 based on the results of tensile tests of the specimens in the direction of sheet thickness [14, 15]. However, it should be noted that the size of reduction in area  $\psi_z$  is mainly affected by the presence of nonmetallic inclusions in steel [3, 16, 17]. In our case, it is possible to expect an increased structural banding of metal and a low content of globular nonmetallic inclusions. Taking into account that propagation of cracks is determined by the toughness of metal matrix [16], the use of the specified criterion may be insufficient. In addition, the determination of reduction in area  $\psi_z$  occurs at a positive temperature that does not correspond to the calculated operation temperature, which also cannot fully guarantee the absence of brittle layered fracture of welded metal structure during its further operation.

Considering the abovementioned, the evaluation of the resistance to brittle layered fracture of the sheet rolled steels S355 and S420 in the rolling plane X–Y


**Figure 1.** Scheme of cutting out specimens from cruciform welded joints: *a* — on impact bending with notches in the plane X–Y; *b* — on tension to determine the quality class of steel

**Table 2.** Chemical composition of sheet rolled steels S355J2+N, P355NL2 and S420NL

Data source	Mass fraction, %											
	C	Mn	Si	P	S	Cr	Ni	Cu	Al	V	Nb	Ti
S355J2+N, $t = 25$ mm, normalized rolling												
Control analysis of PWI	0.14	1.34	0.18	0.022	0.016	0.036	0.03	0.05	0.028	<0.005	0.023	0.015
S355J2+N, $t = 20$ mm, normalized rolling												
Control analysis of PWI	0.15	1.37	0.20	0.017	0.009	Was not determined		0.028	–	0.023	0.017	
DSTU EN10025-2:2007, Table 4	$\leq 0.23$	$\leq 1.70$	$\leq 0.60$	$\leq 0.35$	$\leq 0.35$	–		–	$\leq 0.55$	–	$\leq 0.13$	
P355NL2, $t = 20$ mm, normalization												
Control analysis of PWI	0.17	1.33	0.33	0.009	0.002	0.036	0.045	0.010	0.033	0.006	0.033	0.003
DSTU EN10028-3:2018, Table 1	$\leq 0.18$	1.10–1.70	$\leq 0.50$	$\leq 0.020$	$\leq 0.005$	$\leq 0.30$	$\leq 0.50$	$\leq 0.70$	0.025	$\leq 0.10$	$\leq 0.05$	$\leq 0.03$
S420NL, $t = 25$ mm, normalization												
Control analysis of PWI	0.13	1.50	0.26	0.015	$\leq 0.002$	0.07	0.07	0.05	0.041	0.054	0.035	<0.005
DSTU EN 10025-3:2007, Table 3	$\leq 0.22$	0.95–1.80	$\leq 0.65$	$\leq 0.030$	$\leq 0.025$	$\leq 0.35^*$	$\leq 0.85$	$\leq 0.60$	–	V+Nb+Ni $\leq 0.26$ %		

\*Mo+Cr  $\leq 0,38$  %.**Table 3.** Mechanical properties of base metal of tested specimens of steels S355J2+N, P355NL2 and S420NL

Data source	$\sigma_y$ , MPa	$\sigma_m$ , MPa	$\sigma_y/\sigma_t$	$\delta_5$ , %	$\psi$ , %	Impact toughness $KCV_{x-y}$ , J/cm <sup>2</sup> , at a temperature					
						–20 °C		–30 °C		–50 °C	
						L	T	L	T	L	T
S355J2+N, $t = 25$ mm											
Tests of PWI	345.1	495.3	0.69	35.9	72.9	265; 352; 214	168; 192; 185	163; 170; 171; 179	63; 60; 58; 57	–	–
	346.8	492.8	0.70	35.0	73.9	277	182	171	59,5	–	–
S355J2+N, $t = 20$ mm											
Tests of PWI	410	530	0.77	33	67	282; 275; 291	131; 163; 127	306; 287; 304	141; 134; 140	–	–
	402	526	0.76	37	71	283	140	299	138	–	–
DSTU EN 10025-2:2007	$\geq 345$	470–630	–	$\geq 22$	–	$\geq 34$	Is not normalized	–	–	–	–
P355NL2, $t = 20$ mm											
Tests of PWI	414	544	0.76	31	–	–	–	–	–	241; 282; 329	73; 104; 113
	410	549	0.75	33	–	–	–	–	–	284	97
DSTU EN 10028-3:2018	$\geq 345$	490–630	–	$\geq 22$	–	–	–	–	–	–	$\geq 34$
S420NL, $t = 25$ mm											
Tests of PWI	430	583	0.73	33	66.2	–	–	327; 344; 338	246.4–333.6	160; 120; 138; 139	–
	433	589	0.74	33	67.3	–	–	336	294,1	139	–
DSTU EN 10025-3:2007	$\geq 400$	520–680	–	$\geq 19$	–	–	–	–	$\geq 29$	$\geq 34$	–

Note. L — tests on longitudinal specimens, T — tests on transverse specimens.

**Table 4.** Investigations for the Z quality group of sheet rolled steels S355J2+N, P3555NL2 and S420NL

Specimen number	Grade of steel, thickness of the sheet	As-delivered steel	$\psi_z$ , %	Z quality group	Mass fraction of sulphur, %
1	S355J2+N, $t = 25$ mm	Normalized rolling	22.0	Z15	0.016
2					
3					
1	S355J2+N, $t = 20$ mm	Normalized rolling	41	> Z35	0.009
2			42		
1	P355NL2, $t = 20$ mm	Normalization	69.1	> Z35	0.002
2			73.2		
1	S420 NL, $t = 25$ mm	Normalization	66.2	> Z35	0.002
2			67.3		

was carried out on the basis of evaluating the value of impact toughness according to the results of testing standard Charpy specimens with a V-notch.

### CHARACTERISTICS OF SOURCE MATERIALS AND RESEARCH PROCEDURE

To study the resistance of the sheet rolled steels S355 and S420 to brittle layered fracture, cruciform billets were made [18] (Figure 1), from which the specimens were cut out to determine the impact toughness  $KCV_{X-Y}$  with a notch in the plane  $X-Y$  and the specimens to determine the size of transverse reduction in area during tension in the direction of metal thickness [15].

The specimens of the sheet rolled steels S355J2+N [5], P355NL2 [19] and S420NL [6] with a thickness  $t = 20$  mm and  $t = 25$  mm were investigated. The chemical composition and type of heat treatment of the steels are given in Table 2. The mentioned steels are microalloyed with niobium Nb and aluminum Al, and the steel S420NL is additionally alloyed with vanadium V. The actual sulphur content for the steels P3555NL2 and S420NL is  $S = 0.003$  wt.%. For the steel S355J2+N, the sulphur content  $S = 0.016$  wt.% at  $t = 25$  mm and  $S = 0.009$  wt.% at  $t = 20$  mm. The mechanical properties of the mentioned steels are given in Table 3.

The microsections for metallographic examinations were cut out along the rolling direction and polished to the purity class 14 using diamond pastes. To reveal microstructure, the specimens were etched in a 4 % alcohol solution of nitric acid. The microstructure was examined with the use of the NEOPHOT-32 microscope. The Vickers hardness was measured by the M-400 LECO hardness meter at 98 mN and 9.8 N. The content of nonmetallic inclusions in the studied specimens was determined on polished unetched microsections [21].

The analysis of experimental data of Tables 2, 3 shows that the chemical composition and mechanical properties of the steels S355J2+N, PS3555NL2 and S420NL meet the requirements [5, 6, 19]. The value of the ratio of yield/ultimate strength  $\sigma_y/\sigma_m \leq 0.75$  is

close to the requirements [13]. Moreover, at a temperature  $T = -30$  °C, the value of impact toughness  $KCV_{-30}$  for the steel S355J2+N of 25 mm thick, which is determined with the use of transverse specimens, meets the requirements [6] for the steel S355NL. According to the results of reference tests, the steels PS355NL2 and S420NL can be attributed to the same strength class S420.

### RESEARCH RESULTS AND DISCUSSION

The results of studies of the quality of the rolled steels S355J2+N, P3555NL2 and S420NL in the direction of thickness [15] are presented in Table 4. Analysis of these data shows that to the lowest quality group Z15, the steel S355J2+N with a thickness  $t = 25$  mm belongs, which is delivered in a state of normalized rolling with a high sulphur content of 0.016 %. The structural steel S355J2+N ( $t = 20$  mm) after normalized rolling and the normalized steels P3555NL2 and S420NL belong to a high-quality group Z35, which is associated with a lower sulphur content:  $S \leq 0.010$  % [3]. From the given data it can be concluded that the main factor that affects the quality of the abovementioned rolled steels (Z group) is the content of sulphur in steel, not the type of heat treatment [3].

At the second stage of investigations, the impact toughness of the mentioned steels in the rolling plane  $KCV_{X-Y}$  (Tables 5, 6) and the impact of high-temperature tempering  $T = 650$  °C (PWHT simulation) on it for the steel S355J2+N were determined (Table 6).

The analysis of the results given in Tables 5, 6 indicates that in the case of sulphur content  $S \leq 0.010$  %, the main factor affecting the toughness of the rolled metal in the plane  $X-Y$  is the type of heat treatment of steel. Thus, based on the results of impact bending tests, the steel S355J2+N,  $t = 20$  mm after normalized rolling has a low impact toughness in the plane  $X-Y$ :  $KCV_{-20} = 9.7$  J/cm<sup>2</sup> (Table 6), which is less than required by the standard —  $KCV_{-20} \geq 35$  J/cm<sup>2</sup> [13]. Here, sheet rolled metal belongs to the quality class Z35:  $\psi_z = 41$  %, with a low sulphur content:  $S = 0.009$  %.

**Table 5.** Impact of the type of heat treatment (state of delivery) on impact toughness  $KCV_{X-Y}$  of sheet rolled steels S355J2+N, P3555NL2 and S420NL2 when the notch is placed in the plane  $X-Y$ 

Standard, grade of steel, sheet thickness	Mass fraction of sulphur, %	Type of heat treatment	Impact toughness $KCV_{X-Y}$ , J/cm <sup>2</sup> , at a temperature	
			-30 °C	-50 °C
DSTU EN 10025-2 S355J2+N. $t = 25$ mm	0.016	Normalized rolling	<u>11.4; 9.6; 8.1</u> 9.7	–
DSTU EN10028-3 P355NL2. $t = 20$ mm	0.002	Normalization	<u>58.9; 51.6; 67.4</u> 59.3	<u>26.9; 13.4; 27.7</u> 22.7
DSTU EN 10025-3 S420NL. $t = 25$ mm	0.002	Normalization	<u>19.9; 18.2; 16.3</u> 18.1	<u>21.0; 21.7; 19.9</u> 20.9
DSTU Б B.2.6-183:2011	≤ 0.010	Any	≥ 35.0; at $R_y \leq 360$ MPa; ≥ 50.0; at $R_y > 360$ MPa transverse specimens*	
DSTU EN 10025-2:2007	≤ 0.035	Normalized rolling	≥ 34.00 (27 J) longitudinal specimens*	–
DSTU EN 10025-3:2007	≤ 0.025	Normalization/ Normalized rolling	≥ 29.00 (23 J) transverse specimens*	≥ 20.00 (16 J) transverse specimens*
DSTU EN10028-3:2018	≤ 0.005	Normalized rolling	≥ 37.50 (30 J) transverse specimens*	≥ 34.00 (27 J) transverse specimens*

\*Impact toughness (impact work) in the plane  $X-Y$  is not normalized.

**Table 6.** Impact toughness  $KCV_{X-Y}$  of sheet rolled steel S3555J2+N with a thickness  $t = 20$  mm after different types of heat treatment

Standard, grade of steel	Type of heat treatment	Impact toughness $KCV_{X-Y}$ , J/cm <sup>2</sup> , at a temperature		
		-20 °C	0 °C	+20 °C
DSTU EN 10025-2:2007 S355J2+N	Normalized rolling	<u>28; 5; 5.5</u> 9.7	<u>5.5; 26; 24</u> 18.5	<u>26; 37; 15</u> 26
	Normalized rolling + high-temperature tempering ( $T = 650$ °C, 1 h)	<u>11; 13; 7</u> 10.3	<u>7; 27; 23</u> 19	–
Requirements of the standard DSTU B V.2.6-183:2011 [13] to the value of $KCV$	For all types of heat treatment	≥ 35.0 transverse specimens*	–	–
Requirements of the standard DSTU EN 10025-2:2007 [5] to the value of $KCV$ ( $KV$ )	Normalized rolling	≥ 34.75 (27 J) longitudinal specimens*	–	–

\*Impact toughness (impact work) in the plane  $X-Y$  is not normalized.

**Table 7.** Impact toughness  $KCV_{X-Y}$  in the plane  $X-Y$  of sheet rolled steel S420NL with a thickness  $t = 25$  mm after normalization and high-temperature tempering

Temperature of testing specimens, °C	Impact toughness $KCV$ , J/cm <sup>2</sup>	
	AS-delivered (normalization)	After high-temperature tempering ( $T = 650$ °C, 1 h)
0	<u>104; 105; 95</u> 101	<u>33; 81; 39</u> 51
-10	<u>51; 74; 48</u> 58	<u>82; 91; 62</u> 78
-20	<u>51; 97; 45</u> 64	<u>48; 61; 38</u> 49
-30	<u>20; 16; 29; 31</u> 24	<u>65; 37; 38</u> 47
-50	<u>21; 22; 20</u> 21	<u>20; 11; 9</u> 13

A high level of toughness in the plane  $X-Y$  that meets the requirements [19] is inherent to the normalized steel P3555NL2,  $t = 20$  mm, the content of sulphur  $S = 0.002$  %:  $KCV_{-30} = 59.3$  J/cm<sup>2</sup> (Table 5), which is also confirmed by tensile tests in the direction of thickness:  $\psi_z = 69$  %. For the steel S420NL2,  $t = 25$  mm, in the normalization state at a sulphur content:  $S = 0.002$  % and a high ductility in the direction of the plane  $\psi_z = 66$  % (Tables 4, 7), impact toughness in the plane  $X-Y$  is equal to  $KCV_{-30} = 18-24$  J/cm<sup>2</sup> (Tables 5, 7), which does not meet the requirements of  $KCV_{-30} \geq 29.75$  J/cm<sup>2</sup> [6]. However, unlike the steel S355J2+N, the metal of the the axial zone after normalization maintains a sufficient toughness [6, 13] to a temperature  $T = -20$  °C, and in the case of carrying out high-temperature tempering, the critical temperature drops to  $T = -30$  °C (Table 7).

The studies of the dependences of impact toughness  $KCV_{x-y}$  in the axial zone of the steel S355J2+N,  $t = 20$  mm, the sulphur content  $S = 0.009$  % (Table 6) on the temperature showed that even at a temperature  $T = +20$  °C, it is located in the lower zone of the S-shaped curve, respectively, and the risk of forming lamellar cracks even during welding in factory con-

ditions at a positive temperature can be sufficiently high. A high-temperature tempering does not affect the toughness of the steel S355J2+N in the plane  $X-Y$ .

Based on the results of metallographic examinations, it was established, that microstructure of the steels S355J2+N, P355NL2 and S420NL is ferritic-pearlitic (Figure 2). The evaluation of banding [20]

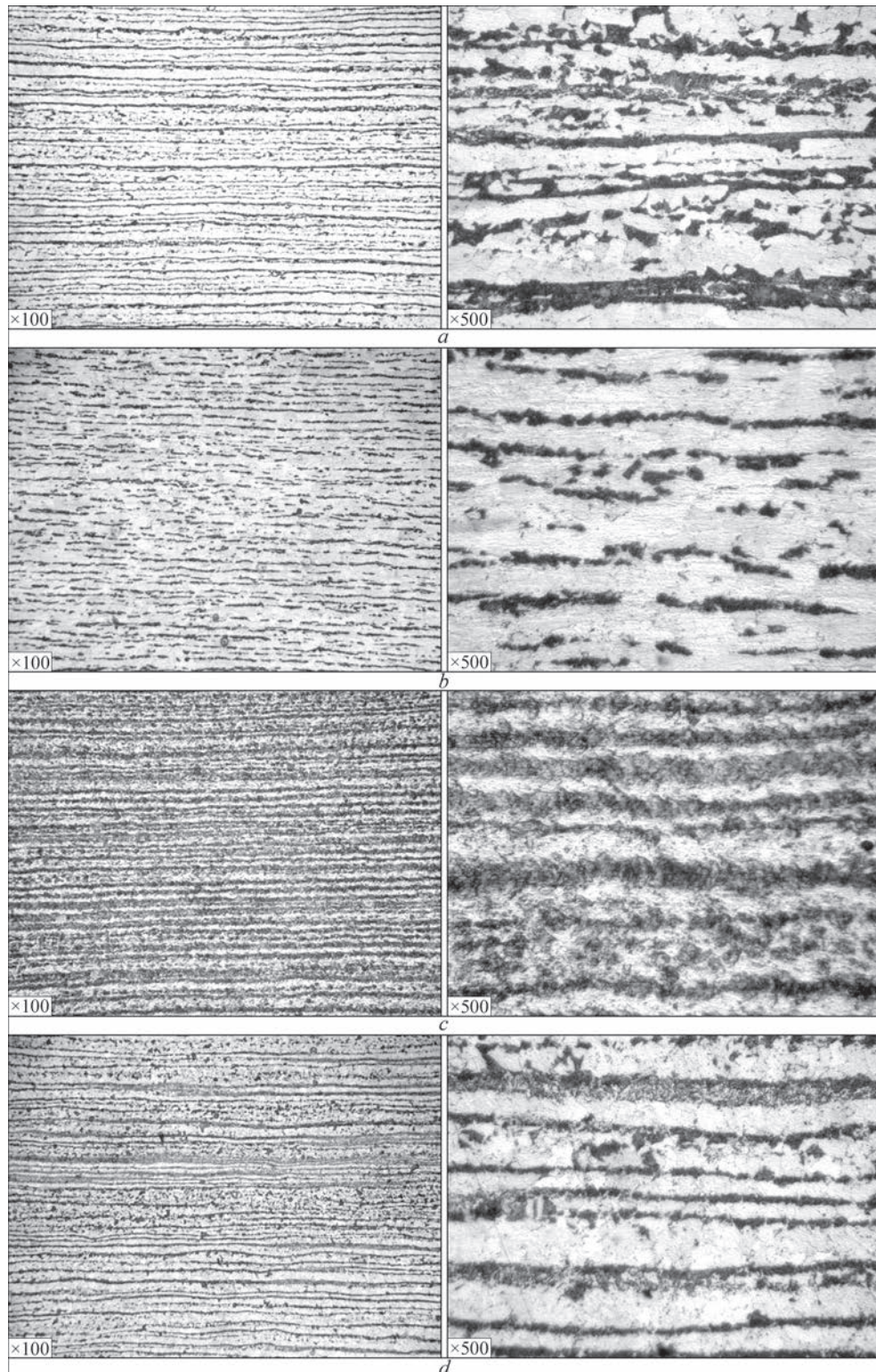


**Figure 2.** Microstructure of axial zone of investigated steels: *a* — steel B355J2+N, 20 mm thickness; *b* — steel B355J2+N, 25 mm thickness; *c* — steel P355J2+N, 20 mm thickness; *d* — steel S420NL2, 25 mm thickness

**Table 8.** Banding of structure of sheet rolled steels S355J2+N, P355Zh2 and S420NL according to DSTU 8974:2019 [20]

Standard, grade of steel, thickness	Banding evaluation
DSTU EN 10025-2 S355J2+N, $t = 20$ mm	Figure 8(4), scale 3, row B ( $\times 100$ )
DSTU EN 10025-2 S355J2+N, $t = 25$ mm	Figure 8(4), scale 3, row B ( $\times 100$ )
DSTU EN 10028-3 P355NL2, $t = 20$ mm	Figure 8(3), scale 3, row B ( $\times 100$ )
DSTU EN 10025-3 S420NL, $t = 25$ mm	Figure 9(5), scale 3, row C ( $\times 100$ )

of these steels (Table 8) shows that S355J2+N after normalized rolling has a much larger banding degree, than P355NL2 and S420NL.

Based on the analysis of the microstructure of the steels (Figure 2), it is seen that unlike S355J2+N, where pearlite is lamellar (Figure 2, *a, b*), in the steel P355NL2 after normalization, sorbite-like pearlite with disoriented grains is formed (Figure 2, *c*). In ferrite, a large amount of carbide precipitates is observed, which transforms the ferrite component into

a ferrite-carbide mixture. This leads to an increase in the hardness of ferrite of the steel P355NL2 compared to S355J2+N (Table 9) and a reduction in the mechanical heterogeneity of the structure. In the steel S355J2+N ( $t = 20$  mm, 25 mm), a larger difference between the values of hardness of ferritic and pearlitic components is observed, the content of carbides in ferrite is low (Table 9, Figure 2, *a, b*).

The steel S420NL occupies an intermediate position: in it both lamellar as well as sorbite-like pearlite

**Table 9.** Results of measurements of hardness of metal of sheet rolled steels S355J2+N, P355NL2 and S420NL

Standard, grade of steel, thickness, place of measurement	Hardness of microstructural components $HV(0.098\text{ N})$		Difference in ferrite and pearlite hardness, MPa	Integral hardness $HV(9.8\text{ N})$ , MPa
	Structural component	Hardness, MPa		
DSTU EN 10025-2 S355J2+N, $t = 20$ mm axial part	Ferrite	<u>1088; 1088; 1264; 1176</u> 1154	720	<u>1548; 1548; 1450; 1470</u> 1504
	Pearlite	<u>1813; 1784; 1813; 1686</u> 1874		
DSTU EN 10025-2 S355J2+N, $t = 20$ mm surface part	Ferrite	<u>1284; 1245; 1264; 1274</u> 1266	713	<u>1450; 1499; 1499; 1480</u> 1482
	Pearlite	<u>1931; 1931; 1813; 1764</u> 1979		
DSTU EN 10025-2 S355J2+N $t = 25$ mm axial part	Ferrite	<u>1587; 1587; 1587; 1587</u> 1587	392	<u>1597; 1637; 1558; 1558</u> 1587
	Pearlite	<u>1891; 2009; 2009; 2009</u> 1979		
DSTU EN 10025-2 S355J2+N $t = 25$ mm surface part	Ferrite	<u>1528; 1646; 1646; 1528</u> 1587	304	<u>1529; 1539; 1666; 1588</u> 1580
	Pearlite	<u>1813; 1813; 1930; 2009</u> 1891		
DSTU EN 10028-3 P355NL2, $t = 20$ mm axial part	Ferrite	<u>1646; 1744; 1617; 1646</u> 1663	294	<u>1646; 1852; 1627; 1752</u> 1719
	Sorbite-like pearlite	<u>1970; 1852; 2009; 1999</u> 1957		
DSTU EN 10028-3 P355NL2, $t = 20$ mm surface part	Ferrite	<u>1499; 1548; 1617; 1499</u> 1540	214	<u>1646; 1646; 1656; 1558</u> 1626
	Sorbite-like pearlite	<u>1617; 1744; 2009; 1646</u> 1754		
DSTU EN 10025-3 S420NL, $t = 25$ mm, axial part	Ferrite	<u>1303; 1480; 1401; 1480</u> 1416	593	<u>1784; 1833; 1612; 1950</u> 1795
	Pearlite	<u>2009; 2009; 2009; 2009</u> 2009		
	Sorbite-like pearlite	<u>2244; 2519; 2254; 2421</u> 2359	943	
DSTU EN 10025-3 S420NL, $t = 25$ mm, surface part	Ferrite	<u>1324; 1480; 1372; 1372</u> 1387	390	<u>1637; 1735; 1735; 1656</u> 1691
	Sorbite-like pearlite	<u>1715; 1784; 1784; 1784</u> 1777		
	Pearlite	<u>2225; 2401; 2450; 2254</u> 2332	945	

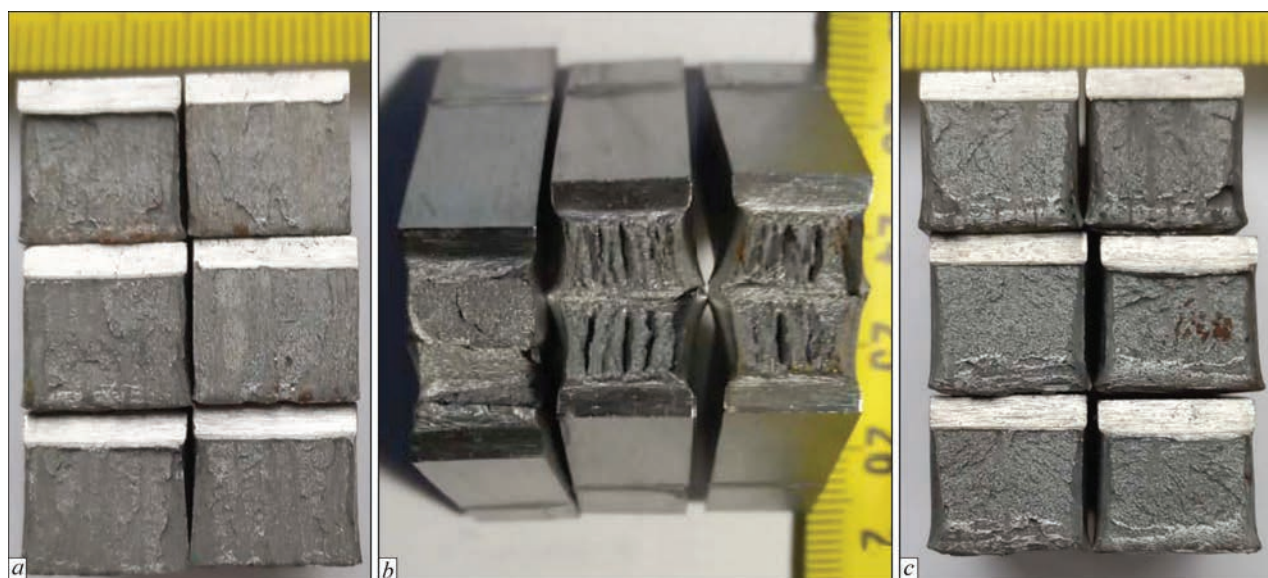
**Table 10.** Evaluation of contamination of sheet rolled steels S355J2+N, P355NL2 and S420NL [21] with nonmetallic inclusions

Standard, grade of steel, thickness	Contamination					
	By globular oxides			By sulfides		
	Size number	Series	Thickness, $\mu\text{m}$	Size number	Series	Thickness, $\mu\text{m}$
DSTU EN 10025-2 S355J2+N, $t = 20$ mm	0.5	Thin	From 3 to 8	0.5	Thin	From 2 to 4
DSTU EN 10025-2 S355J2+N, $t = 25$ mm	1.0					From 13 to 76
DSTU EN 10028-3 P355NL2, $t = 20$ mm	1.5					From 2 to 4
DSTU EN 10025-3 S420NL, $t = 25$ mm	0.5			Not revealed		

is formed (Figure 2, *d*), the precipitation of carbides in ferrite is absent. Mechanical heterogeneity of the structure (difference in hardness of ferrite and lamellar pearlite)  $HV\ 0.098N$  is somewhat lower, than for the steel S355J2+N,  $t = 20$  mm (Table 9). For sorbite-like pearlite, the difference in hardness with ferrite reaches 943HV, which is much larger than for the steel S355J2+N (Table 9). However, in this case, the negative impact of mechanical heterogeneity is lower due to a smaller banding of the rolled metal and a greater toughness of a sorbite-like pearlite than a lamellar one. For the steel S355J2+N, an increase in the pearlite component in the axial zone [7] is observed, which is associated with carbon diffusion to the center of the sheet. This leads to an increase in the integral hardness  $HV\ (9.8\ N)$  and the difference in hardness  $HV\ 0.098N$  of ferrite and lamellar pearlite (anisotropy of structure) for the axial zone (Table 9). Accordingly, in the axial zone, the minimum toughness of the metal across the thickness of the sheet should be expected.

Considering the fact that the studied steels are characterized by fine-dispersed nonmetallic inclusions that do not significantly affect the toughness of the metal (Table 10), it may be concluded that the main cause for the decrease in toughness in the plane  $X$ – $Y$  for the sheet rolled steel S355+N, subjected to normalized rolling, is the formation of expressed banded structure with the formation of fibers of ferrite and pearlite as a result of such treatment, which have a high anisotropy of mechanical properties (Figure 2, *a*, *b*, Table 9).

The presence of such anisotropy is the cause of brittle fracture during the test on impact bending in the plane  $X$ – $Y$  [10] for the steel after normalized rolling, during which its additional deformation in the austenitic area at temperatures close to the point  $A_{c3}$  is performed, which causes the formation of expressed fibrous structures. In the steels P355NL2 and S420NL subjected to normalization, as a result of reducing the level of banding and a decrease in mechanical anisotropy between ferrite and pearlite, as well as the formation of fine-grained structure of


**Figure 3.** Fractures of Charpy specimens of investigated steels: *a* — steel S355J2+N, 20 mm thickness, notch in the plane  $X$ – $Y$  (axial zone), test temperature  $T = 0$  °C; *b* — steel S355J2+N, 25 mm thickness, longitudinal specimen, testing temperature  $T = -20$  °C; *c* — steel S420NL2, 25 mm thickness, notch in the plane  $X$ – $Y$  (axial zone), testing temperature  $T = -30$  °C

sorbite-like pearlite with disoriented boundaries (Figure 2, *c*, *d*, Table 9), the toughness of metal in the plane  $X$ – $Y$  grows considerably and, respectively, a transition from brittle coarse-crystalline fracture [22] for the steel S355J2+N to a brittle-tough fracture for the steel P355NL2 and S420NL occurs (Figure 3, *a*, *c*). A significant anisotropy of mechanical properties between the fibers of ferrite and pearlite in the steel S355J2+N is also revealed in the layered metal fracture in the case of testing Charpy specimens, cut out along the rolled metal, on impact bending (Figure 3, *b*) as a result of a bulk stress state before the crack front [16].

It should be expected that due to a low content of nonmetallic inclusions in the steel after normalized rolling, deformation of the axial zone metal during welding will occur in the temperature range, where the material has a sufficient ductility, respectively, the layered fracture will be absent. Manifestation of brittle or quasi-brittle layered fracture may occur during the further operation of the welded structure at low temperatures in the presence of crack-like defects in the axial zone of the rolled metal in the case of action of tensile tests in the direction of thickness. Such initiating defects may be available delaminations of metal or separate elongated clusters of nonmetallic inclusions in steel. In this case, to prevent such layered delaminations, it is important to use a sheet rolled metal with the control of continuity and limit the content of sulphur  $S \leq 0.010\%$  and phosphorous:  $P \leq 0.015\%$ .

Thus, the structure of the steel S355J2+N [5] after normalized rolling is fibrous, with an expressed anisotropy, which is different from the structure obtained after normalization. Accordingly, this also applies to mechanical properties [10], such as toughness of metal in the rolling plane  $X$ – $Y$ . This means that to use the steels [5, 6] after normalized rolling for tanks or other critical structures (bridges, platforms, etc.) in assemblies, where the operation of metal in the direction of thickness should be taken into account, additional conditions must be applied [23, 24]. For cylindrical steel tanks, it is rational to limit the thickness of the sheet steel delivered after normalized rolling with the size  $t \leq 15$  mm, for which the standard [15] does not envisage the requirements for the Z quality group.

A high-temperature tempering, which simulated PWHT for the steel S355J2+N after normalized rolling does not significantly reduce banding and mechanical heterogeneity between ferrite and pearlite. Therefore after its end, an increase in impact toughness  $KCV_{X-Y}$  in the plane  $X$ – $Y$  is absent (Table 6). For the normalized steel S420NL, high-temperature tempering promotes further coagulation of carbides, which increases the volumetric fraction of sorbite-like pearlite and,

accordingly, reduces the mechanical heterogeneity between pearlite and ferrite. As a result, the transition temperature shifts into the region of lower temperatures: from  $T = -20$  °C to  $T = -30$  °C (Table 7).

## CONCLUSIONS

1. The use of normalized rolling does not provide the sheet rolled steel S355+N the state, equivalent to the normalization state. As a result of normalized rolling, due to the additional compression of the sheet in the temperature region near the temperature  $A_{c3}$ , a microstructure is formed in the steel, which has an expressed banding and in which the fibers of ferrite and pearlite are formed with a high anisotropy of mechanical properties. The formation of such a fibrous structure leads to brittle fracture of the metal in the plane  $X$ – $Y$  at a calculated temperature.

For the axial zone of the sheet, anisotropy of the structure is maximum. Accordingly, in this zone, the minimum toughness of the metal should be expected across the thickness of the sheet, and it can be considered as a probable location for lamellar crack formation.

2. Providing Z quality to the rolled steel in accordance with DSTU EN 10164:2009, which is determined during tension of the specimens in the direction perpendicular to the surface of the product, may be insufficient to prevent brittle layered fracture of the metal in the welded joints when using the steels after normalized rolling with a low sulphur content:  $S \leq 0.010\%$ . In this case, as an additional condition for resistance of the sheet rolled steels S355 and S420 to a brittle layered fracture, in addition to the rolled metal of the Z quality group, it is recommended to use such an indice as the minimum impact work, which is determined on the specimens with the notch in the rolling plane  $X$ – $Y$  (along the axis of the sheet)  $KCV_{X-Y}$  and the value of which, before the accumulation of static data, is proposed to be taken according to DSTU-N B EN 1993-1-10:201:  $KCV_{X-Y} \geq 27$  (40) J or according to DSTU EN 10025-2:2007 and DSTU EN 10025-3:2007, depending on the operating conditions, type of structure and degree of responsibility of welded assemblies. The temperature of testing specimens is determined taking into account the requirements of the relevant standard for designing metal structures of tanks, bridges, etc.

3. For metal structures of tanks of A group (wall, contour sheets of the bottom) under the condition of necessary providing the metal work in the direction of thickness, it is proposed to use the sheet rolled steels S355 and S420 in a state after normalization or normalization with a high-temperature tempering. In this case, the sulphur content in steel should not exceed

$S \leq 0.010$  %, and it is necessary to control the continuity for it. In the case of using steels in a state of normalized rolling for the wall and contour sheets of the bottom of tanks, it is rational to limit the thickness of the sheet with a size  $t \leq 15$  mm, for which the requirements to provide special properties in the perpendicular direction to the surface of the sheet are not envisaged.

*The authors express their gratitude to PJSC "Ukrstal Konstruktsiya" for support of the research works.*

## REFERENCES

1. DSTU 8803:2018: *Rolled plate from carbon steel of general quality Specifications* [in Ukrainian].
2. DSTU 8541:2015: *High-strength rolled steel. Specifications* [in Ukrainian].
3. Skorokhodov, V.N., Odesskij, P.D., Rudenko, A.V. (2002) *Building steel*. Moscow, Metallurgizdat [in Russian].
4. Biletsky, S.M., Golinko, V.M. (1983) *Industrial production of oversized welded structures*. Kyiv, Naukova Dumka [in Russian].
5. DSTU EN 10025-2:2007: *Hot rolled products of structural steels*. Pt 2: Technical delivery conditions for non-alloy structural steels.
6. DSTU EN 10025-3:2007: *Hot rolled products of structural steels*. Pt 3: Technical delivery conditions for normalized/normalized rolled weldable fine grain structural steels [in Ukrainian].
7. Matvienkov, S.A., Shebanits, E.N., Tarasenko, O.S. et al. (2012) Production of steel and rolled steel of S355...N grade for manufacture of metal structures for construction of NSC "Olimpiyskiy" in Kiev. *Metal i Litio Ukrainy*, 225–226(2–3), 35–38 [in Russian].
8. Faria, R., Gorni, A., Matsubara, D. et al. (2019) Influence of the normalizing rolling parameters on the toughness of a Nb, V and Ti microalloyed steel processed in the gerdau plate mill. In: *Proc. of Iron & Steel Technology Conf. – AISTech 2019, Association for Iron and Steel Technology, Pittsburgh, May 2019*. DOI: <https://doi.org/10.33313/377/191>.
9. Khaisterkamp, F., Hulka, K., Matrosov, Yu.I. et al. (1999) *Niobium-containing low-alloy steels*. Moscow, SP Internet Engineering [in Russian].
10. Broek, D. (1980) *Fundamentals of mechanics of fracture*. Moscow, Vysshaya Shkola [in Russian].
11. API 650 (2020) *Welded tanks for oil storage*. 13<sup>th</sup> Ed.
12. EN 14015-2017: *Specification for the design and manufacture of site built, vertical, cylindrical, flat-bottomed, above ground, welded, steel tanks for the storage of liquids at ambient temperature and above, CEN/TC 265, Secretariat: BSI*.
13. DSTU B V.2.6-183:2011: *Vertical cylindrical steel tanks for oil and oil products. Specifications*. Minregion Ukrainy [in Ukrainian].
14. DSTU-N B EN 1993-1-1:2010: *Eurocode 3. Design of steel structures*. Pt 1-1. General rules and rules for buildings [in Ukrainian].
15. DSTU EN 10164:2009: *Steel products with improved deformation properties perpendicular to the surface of the product. Technical delivery conditions* [in Ukrainian].
16. Girenko, V.S., Bernatsky, A.V., Rabkina, M.D. et al. (1987) Lamellar, lamellar-brittle and lamellar-ductile failure of welded joints. *Problemy Prochnosti*, 3, 70–76 [in Russian].
17. Laddha, S.S., Pandurang, S.S., Deepashri, D.N. (2016) Lamellar tearing: A failure case study. *J. of Failure Analysis and Prevention*, [https://www.researchgate.net/publication/304577342\\_Lamellar\\_Tearing\\_A\\_Failure\\_Case\\_Study](https://www.researchgate.net/publication/304577342_Lamellar_Tearing_A_Failure_Case_Study)
18. Poznyakov, V.D., Barvinko, A.Yu., Barvinko, Yu.P. et al. (2012) Cold resistance and lamellar fracture resistance of welded joints on steel 06GB-390. *The Paton Welding J.*, 3, 35–39.
19. DSTU EN 10028-3:2015: *Flat products made of steels for pressure purposes*. Pt 3: Weldable fine grain steels, normalized [in Ukrainian].
20. DSTU 8974:2019: *Metallographic method for determination of microstructure of sheets and bands* [in Ukrainian].
21. DSTU ISO 4967:2017: *Steel. Determination of content of nonmetallic inclusions. Metallographic method of evaluation using standard diagrams* [in Ukrainian].
22. DSTU 3715–98: *Metals. Types of rupture surfaces (fractures)* [in Ukrainian].
23. Girenko, V.S., Bernatskii, A.V., Rabkina, M.D. et al. (1987) Lamellar, lamellar-brittle, and lamellar-ductile failure of welded joints. *Strength of Materials*, 19, 372–378.
24. DSTU-N B EN 1993-1-10:2012: *Eurocode 3. Design of steel structures*. Pt 1-10. Properties of crack resistance and strength through the rolled stock thickness [in Ukrainian].

## ORCID

A.Yu. Barvinko: 0000-0002-5719-0576

## CONFLICT OF INTEREST

The Authors declare no conflict of interest

## CORRESPONDING AUTHOR

A.Yu. Barvinko

E.O. Paton Electric Welding Institute of the NASU  
11 Kazymyr Malevych Str., 03150, Kyiv, Ukraine.

E-mail: tanksweld@gmail.com

## SUGGESTED CITATION

A.Yu. Barvinko, Yu.P. Barvinko, A.M. Yashnyk (2023) Use of structural steels in storage tank construction after normalized rolling. *The Paton Welding J.*, 6, 8–17.

## JOURNAL HOME PAGE

<https://patonpublishinghouse.com/eng/journals/tpwj>

Received: 03.04.2023

Accepted: 17.07.2023

DOI: <https://doi.org/10.37434/tpwj2023.06.03>

## NARROW-GAP TIG WELDING OF THICK STEEL 20

S.V. Akhonin, V.Yu. Bilous, R.V. Selin, V.V. Pashynskiy, S.L. Shvab

E.O. Paton Electric Welding Institute of the NASU  
11 Kazymyr Malevych Str., 03150, Kyiv, Ukraine

### ABSTRACT

Arc welding of joints of carbon steels 20–100 mm thick can be performed both by consumable and nonconsumable electrode, using shielding gases or flux. In order to increase the efficiency of welding operations, multilayer narrow-gap welding (NGW) with filler wire feeding can be used for metals of medium and large thicknesses. This study deals with application of tungsten electrode NGW process with and without superposition of a controlling magnetic field for welding samples from steel 20 of 40 mm thickness. Results of investigations of the macro- and microstructure and microhardness of the welded joints are given. It was found that application of an external controlling magnetic field for NGW of steel 20 joints ensures a higher quality of the welded joints.

**KEYWORDS:** narrow-gap argon-arc welding, tungsten electrode, steel 20, controlling magnetic field, structure, microstructure, microhardness

### INTRODUCTION

Arc welding of joints of carbon steels 20–100 mm thick can be performed both by consumable and nonconsumable electrode with application of shielding gases or flux. At present tungsten electrode welding is believed to be a reliable, but an unproductive process of arc welding of thick butt joints. One of the methods to improve the productivity of welding operations for different metals of medium and large thickness is narrow-gap multilayer welding, namely NGW with filler wire feed. Its special feature is the shape of edge preparation in the form of a rectangular slot, in which one bead is deposited on the other by the arc process across the entire width of the gap. It results in formation of a metal layer, which fills the gap to a certain height. Successive performance of these operations leads to filling the entire volume of the gap by the deposited metal [1, 2]. The main advantages of NGW are a significant reduction of the required quantity of the deposited metal (compared to treatment of edges of a regular shape), reduction of filler wire consumption, weld width, and HAZ width, as well as decrease of welding stresses and strains [2]. NGW of steel parts is mainly performed with application of consumable electrode welding technology [3]. To produce sound welded joints, it is necessary to ensure reliable melting of the side walls at NGW and fusion of the weld metal with the base metal [5, 6]. In consumable electrode welding deformed wire or welding with filler wire oscillation, and welding with filler wire rotation are used [3, 7, 8]. The process of consumable electrode NGW has such an advantage over tungsten electrode NGW, as a higher productivity [4].

PWI developed a technology of tungsten electrode NGW which has proven itself well for welding titanium and some other nonferrous metals [1, 9]. Successful realization of this process requires overcoming certain difficulties, the main of which is ensuring reliable melting of the groove side walls. To ensure reliable melting of the side walls, it is necessary to redistribute the thermal energy between the edges being welded. With this purpose both mechanical displacement of the tungsten electrode and external magnetic field can be used at NGW [10]. As carbon steels have their own magnetic field and high magnetic properties, application of an external controlling magnetic field for NGW becomes complicated, as the own magnetic field of the parts being welded, can be superposed on the external controlling magnetic field, formed by the magnetic system of the welding head.

### OBJECTIVE OF THE WORK

Was to study the possibility of performance of tungsten electrode NGW with an external controlling magnetic field of welded joints of 40 mm carbon steel.

### INVESTIGATION METHODS AND MATERIALS

Welding of 40 mm thick samples from steel of grade 20 to GOST 1050–88 was conducted to study the possibility of tungsten electrode NGW performance. Filler wire of 1.6 mm diameter of Sv-08G2S grade was used for welding. Welding was conducted both without an external controlling field, and with an external controlling magnetic field. The process schematic is shown in Figure 1. Welding was performed by 5 mm tungsten electrodes of EVI-1 grade. VDU501 welding power source was used. Welding current was 460–500 A, arc voltage was 12 V, rate of feeding the filler metal of 1.6 mm Sv-08G2S wire

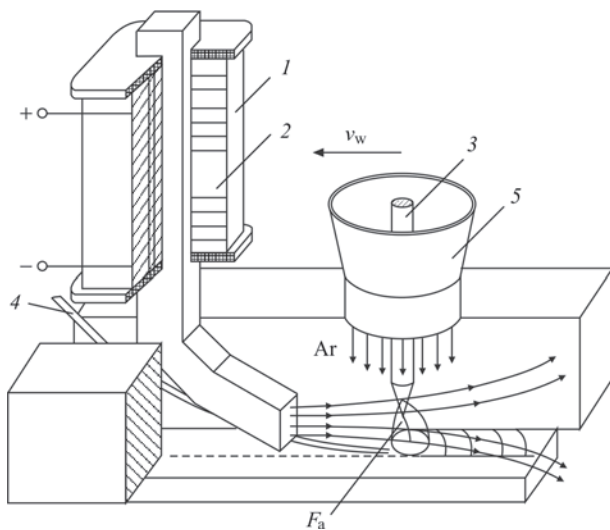


**Figure 1.** Schematic of the process of tungsten electrode NGW with application of an external controlling magnetic field: 1 — electromagnet coil; 2 — electromagnet core; 3 — tungsten electrode; 4 — filler wire; 5 — protective nozzle

into the weld pool was on the level of 20–25 g/min. The set arc voltage was maintained by an automatic system, which adjusted the arc voltage. Welding arc deflection to the side walls was ensured by superposition of an external magnetic field of 10–20 Hz frequency, which is generated by an external electromagnet (Figure 1). The welding process and tungsten electrode position in the groove were controlled by a videorecording system (Figure 2). Figure 2 shows the schematic of sample set-up for NGW, the substrate for sample set-up was also made from steel 20. Length of samples for welding was equal to 600 mm.

### INVESTIGATION RESULTS

Tungsten electrode NGW is characterized by participation of a large fraction of filler metal in weld metal formation, in our experiments it was equal to ~ 90 %, so that the properties of metal of NGW welded joints are determined mainly by the properties of filler wire material and influence of the external controlling magnetic field.

Metallographic investigation of transverse macrosections did not reveal any pores in the metal of the weld produced with an external controlling magnetic field. The metal of the weld made without an external controlling magnetic field and without redistribution of thermal energy of the welding arc, contained lacks of fusion, lacks of penetration and individual pores were observed.

Photographs of transverse macrosections of the produced welded joints are given in Figure 3.

Conducted metallographic investigations of joints made by NGW without application of an external controlling magnetic field with filler material feeding at the rate of 20–25 g/min showed that the welds had great depth of penetration of the lower wall of the

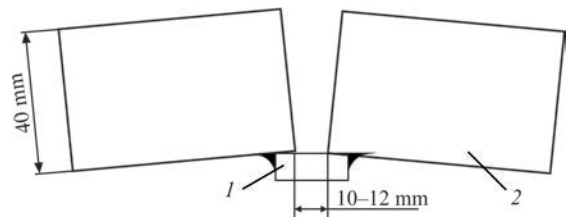


**Figure 2.** Schematic of sample set-up for tungsten electrode narrow gap welding: 1 — substrate; 2 — samples to be welded

groove and small width in the lower part, the welds had lacks of penetration and lacks of fusion (Figure 3, *a*). Penetration of the vertical side walls turned out to be nonuniform, as was the shape of the deposited layers, which is related to appearance of such defects as lacks of penetration and lacks of fusion. Application of a magnetic field for welding arc deflection ensured uniform penetration of the side walls and sound weld formation (Figure 3, *b*). Deposited layers have a smooth concave surface, which is indicative of reliable fusion of the filler and base metal. Penetration of the base metal and the previous bead is small. X-ray inspection of the welded joints produced using an external controlling magnetic field in the optimal modes did not reveal any lacks of penetration, lacks of fusion or pores in the metal of the weld, made with application of an external controlling magnetic field.

Alongside the influence of an external controlling electromagnetic field ((ECEMF) on the welded joint macrostructure, of considerable interest is evaluation of the impact of such a treatment on its microstructure. Presence of such an impact was established in many investigations, in particular works [11, 12, 14] give a review of treatment variants and possible mechanisms of the magnetic field influence on the alloy microstructure. Note that there is no single generally accepted mechanism describing the influence of the field. This is related to the fact that there exist many variants of treatment technology and it is applied for

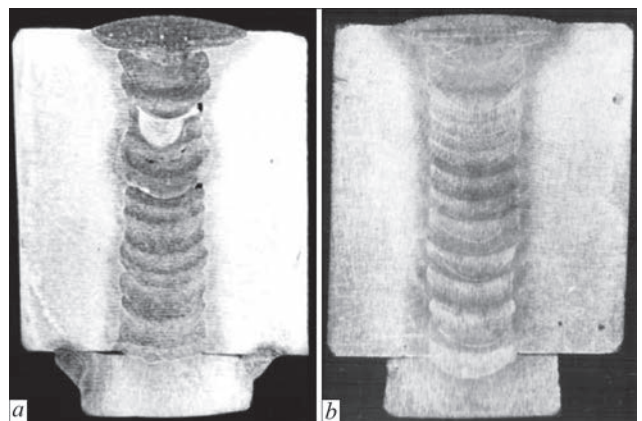


**Figure 3.** Transverse macrosections of joints of carbon steel 20 produced by tungsten electrode NGW: *a* — without an external controlling magnetic field; *b* — with an external controlling magnetic field

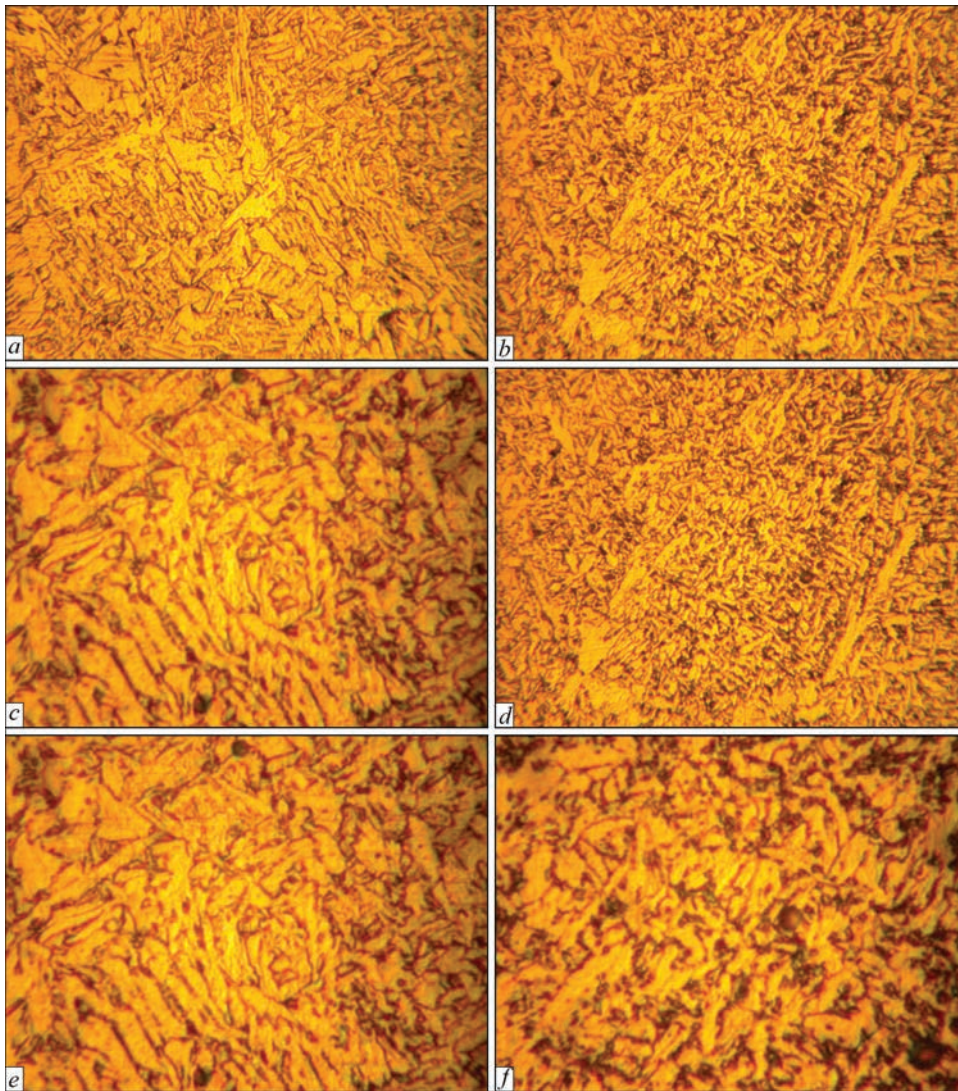


**Figure 4.** Microstructure of metal of the weld without the impact (*a, c, e*) and with the impact (*b, e, f*) of an external magnetic field: *a, b* —  $\times 200$ ; *c, d* —  $\times 500$ ; *e, f* —  $\times 1250$

alloys of different chemical composition with different physical properties (ferromagnetic and nonferromagnetic materials). Therefore, there can be several variants of the influence mechanism, depending on such factors as specific power of the field, frequency, duration and temperature range, in which treatment is conducted. However, the most certain fact is that ECEMF superposition leads to structure refinement.

Figure 4 gives the microstructure of weld metal, not subjected to the impact (ECEMF) and of the weld made under the conditions of the field application. One can see that a homogeneous dispersed structure forms in both the cases at magnification  $\times 200$  (Figure 4, *a, b*). No obvious difference between the structures is revealed. However, at magnifications  $\times 500$  (Figure 4, *c, d*), it can be seen that ECEMF impact makes the structure more dispersed. Another feature of ECEMF impact becomes obvious when magnification  $\times 1250$  is used (Figure 4, *e, f*). It consists in that the grain morphology also changes in addition to struc-

ture refinement, and they transform from elongated (Figure 4, *e*) into equiaxed ones (Figure 1, *f*). Such an influence of the field was earlier revealed when studying the crystallization of nonferromagnetic material (tin bronze) [13], but the data of this analysis suggest that this effect is of a more general nature.

Manifestation of this effect is also visible at analysis of the fusion zone structure (Figure 2).

At magnification of  $\times 50$  (Figure 5, *a, b*) a primary dendritic structure of the metal is revealed in the fusion zone, which in both the cases is similar and ECEMF effect is not obviously manifested, but at magnifications  $\times 500$  (Figure 5, *c, d*) and  $\times 1250$  (Figure 5, *e, f*) one can see that the microstructure becomes more dispersed and pearlitic colonies practically disappear, being replaced by a uniformly distributed carbide phase.

Microhardness distribution of the metal of welded joints from steel 20 made both with and without ECEMF impact was conducted, using PMT-2 microhardness meter with 100 g load (Figure 6).

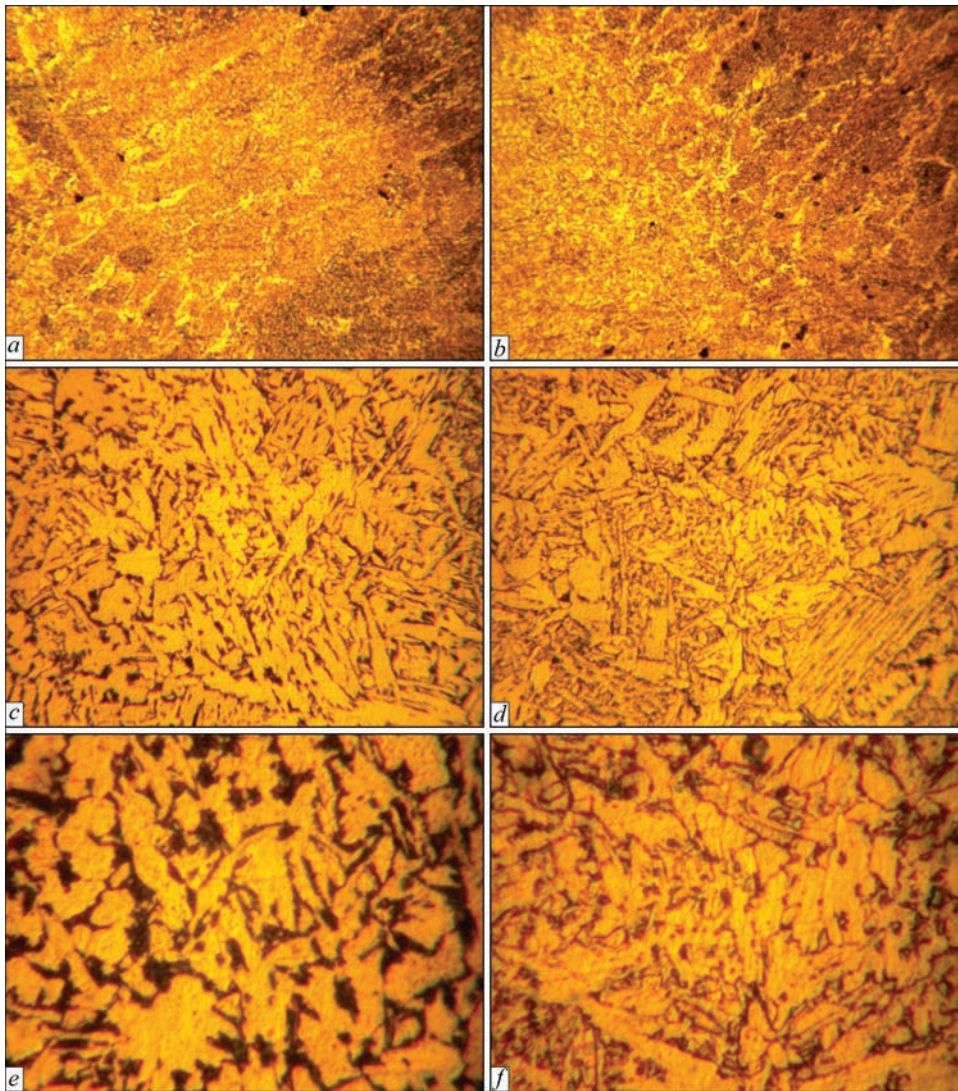


**Figure 5.** Microstructure of metal of the fusion zone without the impact (*a, c, e*) and with the impact (*b, d, f*) of an external controlling magnetic field: *a, b* —  $\times 50$ ; *c, d* —  $\times 500$ ; *e, f* —  $\times 1250$

Microhardness values of base metal (steel 20) are on the level of 1700 MPa (Figure 7 and Figure 8). In the metal microhardness values are on the level of 2000 MPa on average, which, in its turn, is most prob-

ably related to formation of a new hardening structure. Microhardness of metal in the weld produced without the magnetic field impact is on the level of 2300 MPa (Figure 7), and that of the metal of the weld, produced under the impact of an external magnetic field is on the level of 1900 MPa (Figure 8). This may be related to the fact that during external magnetic field application a more fine-grained structure forms with a

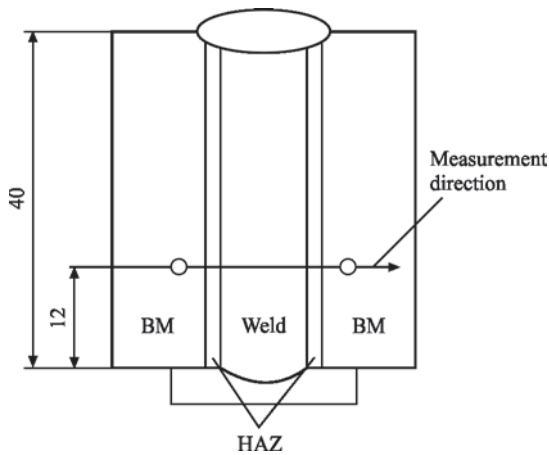


**Figure 6.** Schematic of measurement of microhardness distribution in the welded joint of steel 20 produced by NGW with 1.6 mm Sv-08G2S filler wire

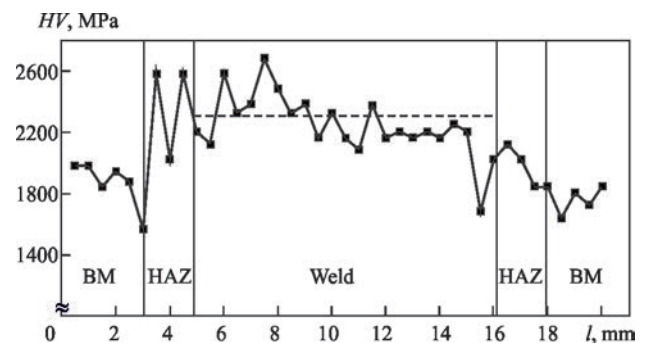


**Figure 7.** Microhardness distribution in the welded joint of steel 20, produced by NGW with 1.6 mm Sv-08G2S filler wire, without ECEFM impact in as-welded condition

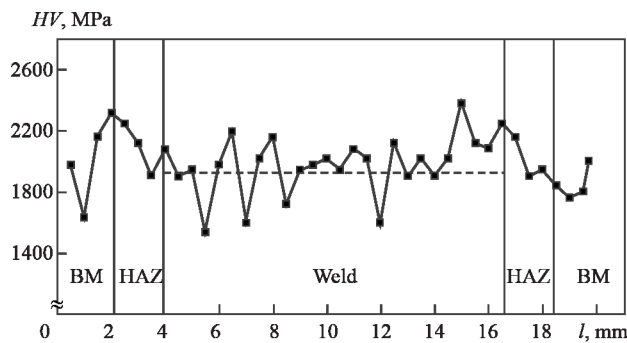


**Figure 8.** Microhardness distribution in the welded joint of steel 20 in as-welded condition, produced by NGW with 1.6 mm Sv-08G2S filler wire and ECEMF impact

changed morphology of the cementite phase. Carbide particles do not form colonies with lamellar morphology, but they are uniformly distributed in the ferrite. As a result, the weld metal produced by such a method has higher ductility and lower microhardness than the same sample produced without the influence of the external magnetic field.

## DISCUSSION OF THE RESULTS

Technology of tungsten electrode NGW with an external controlling magnetic field, which has earlier proven itself well for welding titanium and some other nonferrous metals can be applied for welded joints made from magnetic steels, such as steel 20 of 40 mm and greater thickness. Magnetic control of redistribution of thermal energy of the welding arc fulfills its function — welding arc deflection and anode spot shifting to the required value, which ensures absence of lacks of penetrations, lacks of fusion, and pores in the welds. Side wall penetration is uniform with good weld formation. In welds made without application of magnetic control and without redistribution of the arc thermal energy, numerous defects are recorded, namely lacks of penetration and lacks of fusion. Application of NGW with magnetic control of the welding arc also allows increasing the deposition rate and raising the feed rate of filler metal of 1.6 mm Sv-08G2S wire into the weld pool to the level of 35 g/min. The authors failed to perform deposition by the process of tungsten electrode NGW without magnetic control with such a feed of filler metal. Thus, application of magnetic control of the welding arc allows somewhat compensating the main disadvantage of tungsten electrode argon-arc welding — the low deposition rate. More over, investigations of welded joint microstructure and establishing the microhardness distribution in the metal of steel 20 welded joints produced both under the impact of ECEMF, and without it, led to the conclusion that, on the whole, the level of microhardness in the weld with ECEMF impact is characterized by a high uniformity, without any significant gradi-

ents or excess hardening of the weld zone, compared to hardness distribution in a sample produced without ECEMF impact. This allows expecting a higher resistance of welded joint metal to the impact of dynamic and cyclic loads.

Thus, ECEMF application during welding not only allowed preventing formation of weld macrostructure defects, but also had a positive impact on its microstructure. Further investigations should be aimed at establishing the dependence of microstructural characteristics on ECEMF parameters, in order to enhance the observed effects.

## CONCLUSIONS

1. Joints from 40 mm thick steel 20 were welded using the technology of tungsten electrode NGW with an external controlling magnetic field, which had earlier proven itself well for welding titanium and some other nonferrous metals.

2. Investigations of welds produced by tungsten electrode NGW with application of an external controlling magnetic field showed a practically complete absence of lacks of penetration, lacks of fusion and pores in the welds with uniform penetration of the side walls and good weld formation.

3. Performed studies lead to the conclusion about the higher quality of steel 20 welded joints, produced by tungsten electrode NGW with an external controlling magnetic field with filler material feed at the level of 20–25 g/min, compared to tungsten electrode NGW without an external controlling magnetic field.

4. Application of an external controlling electromagnetic field during narrow-gap welding of joints of steel 20 had a positive influence on the joint microstructure. The joint microstructure became more dispersed, pearlitic colonies disappeared, being replaced by a uniformly distributed carbide phase, which is accompanied by achieving a uniform microhardness distribution in the weld metal.

## REFERENCES

1. Akhonin, S.V., Belous, V.Yu., Romanyuk, V.S. et al. (2010) Narrow-gap welding of up to 110 mm thick high-strength titanium alloys. *The Paton Welding J.*, **5**, 34–37.
2. Malin, V. (1987) *Monograph on narrow-gap welding technology*. WRC, Bulletin 323.
3. Hori, K., Haneda, M. (1999) Narrow gap arc welding. *J. of J.W.S.*, **3**, 41–62.
4. Jun, J.H., Kim, S.R., Cho, S.M. (2016) A study on productivity improvement in narrow gap TIG welding. *J. of Welding and Joining*, **34**(1), 68–74.
5. Dak, G., Khanna, N., Pandey, C. (2023) Study on narrow gap welding of martensitic grade P92 and austenitic grade AISI 304L SS steel for ultra-supercritical power plant application. *Archiv. Civ. Mech. Eng.*, **23**, 14–24. DOI: <https://doi.org/10.1007/s43452-022-00540-3>

6. Luo, Y., Zhang, Z.L., Zhou, C.F. et al. (2017) Effect of oscillation parameters of narrow groove MAG welding on weld formation. *J. Hebei Univ. Sci. Technol.*, 38(6). DOI: <https://doi.org/10.7535/hbkd.2017yx01002>
7. Nguyen, D.H. (2014) *Research on droplet transfer and welding process of oscillation arc narrow gap GMAW*. Master's Thesis, Harbin Institute of Technology, Harbin, China.
8. Fang, D.S. (2017) *Study on the characteristics of three-wire indirect arc and its thick-wall narrow gap welding process under gas protection*: Ph.D. Thesis, Dalian University of Technology, Dalian China.
9. Shoichi, M., Yukio, M., Koki, T. et al. (2013) Study on the application for electromagnetic controlled molten pool welding process in overhead and flat position welding. *Sci. Technol. Weld. Join.*, 18, 38–44. DOI: <https://doi.org/10.1179/1362171812Y.0000000070>
10. Belous, V.Yu., Akhonin, S.V. (2007) Influence of controlling magnetic field parameters on weld formation in narrow-gap argon-arc welding of titanium alloys. *The Paton Welding J.*, 4, 2–5.
11. Xinyu, B., Yonglin, M., Shuqing, X. et al. (2022) Effects of pulsed magnetic field melt treatment on grain refinement of Al–Si–Mg–Cu–Ni alloy direct-chill casting billet. *Metals*, 12(7), 1080. DOI: <https://doi.org/10.3390/met12071080>
12. Yujun, H., Hongjin, Z., Xuede, Y. et al. (2022) Research progress of magnetic field regulated mechanical property of solid metal materials. *Metals*, 12, 1988. DOI: <https://doi.org/10.3390/met12111988>
13. Pashynskaya, E.G., Pashynskiy, V.V. (1998) Effect of weak-pulsed magnetic field on structure and properties of Cu–Sn base alloy. *Physics of Metals and Metallography*, 6, 670–674.
14. Belous, V.Yu., Akhonin, S.V. (2011) Formation of narrow-gap welded joints on titanium using the controlling magnetic field. *The Paton Welding J.*, 4, 19–22.

#### ORCID

S.V. Akhonin: 0000-0002-7746-2946,  
V.Yu. Bilous: 0000-0002-0082-8030,  
R.V. Selin: 0000-0002-2990-1131,  
V.V. Pashynskiy: 0000-0003-0118-4748,  
S.L. Shvab: 0000-0002-4627-9786

#### CONFLICT OF INTEREST

The Authors declare no conflict of interest

#### CORRESPONDING AUTHOR

V.Yu. Bilous  
E.O. Paton Electric Welding Institute of the NASU  
11 Kazymyr Malevych Str., 03150, Kyiv, Ukraine.  
E-mail: [belousvy@gmail.com](mailto:belousvy@gmail.com)

#### SUGGESTED CITATION

S.V. Akhonin, V.Yu. Bilous, R.V. Selin,  
V.V. Pashynskiy, S.L. Shvab (2023) Narrow-gap TIG  
welding of thick steel 20. *The Paton Welding J.*, 6,  
18–23.

#### JOURNAL HOME PAGE

<https://patonpublishinghouse.com/eng/journals/tpwj>

Received: 16.05.2023

Accepted: 17.07.2023

WORLD TRADE FAIR FOR WELDING-ENGINEERING —  
JOINING, CUTTING, SURFACING



# LET'S JOIN THE WORLD!

11. – 15. September, 2023

REGISTER NOW!

www.schweissen-schneiden.com





DOI: <https://doi.org/10.37434/tpwj2023.06.04>

# PROPERTIES OF COATINGS PRODUCED BY HVOF SPRAYING OF COMPOSITE POWDERS BASED ON AMORPHIZING FeMoNiCrB ALLOY

N.V. Vihilianska<sup>1</sup>, C. Senderowski<sup>2</sup>, K.V. Yantsevych<sup>1</sup>, **O.I. Dukhota**<sup>3</sup>

<sup>1</sup>E.O. Paton Electric Welding Institute of the NASU  
11 Kazymyr Malevych Str., 03150, Kyiv, Ukraine

<sup>2</sup>Warsaw University of Technology  
Pl. Politechniki 1, 00661, Warsaw, Poland

<sup>3</sup>National Aviation University  
1 Lubomyr Husar Prosp., 03058 Kyiv, Ukraine

## ABSTRACT

Applying the method of HVOF spraying with the use of mechanically-alloyed powders based on the amorphizing FeMoNiCrB alloy with the additions of (Ti, Cr)C and FeTiO<sub>3</sub> compounds, the coatings with amorphous crystalline heterophase structure were produced. The coatings of FeMoNiCrB–(Ti, Cr)C and FeMoNiCrB–FeTiO<sub>3</sub> systems have a dense fine-grained structure with a porosity of 2.4 and 1.2 % and a hardness of 5510 ± 250 and 4410 ± 190 MPa, respectively. The study of corrosion resistance and resistance to fretting corrosion of the developed coatings was conducted. It is shown that the use of composite powders based on FeMoNiCrB alloy with the addition of (Ti, Cr)C and FeTiO<sub>3</sub> compounds as spraying materials allows increasing the protective properties of the coatings compared to the coating of FeMoNiCrB alloy. It was found, that in the case of producing composite FeMoNiCrB–(Ti, Cr)C and FeMoNiCrB–FeTiO<sub>3</sub> coatings on the steel base St3, the corrosion resistance of the specimens in the solutions of 3 % NaCl, 10 % H<sub>2</sub>SO<sub>4</sub> and 10 % KOH is increased by 7.3, 9; 3.9, 5.3 and 9.5, 9.7 times, respectively. FeMoNiCrB–(Ti, Cr)C and FeMoNiCrB–FeTiO<sub>3</sub> coatings have a fairly high resistance to fretting corrosion, which is 4.6 and 5.8 times higher than the resistance of titanium OT4-1 alloy. The obtained results indicate the prospect of using HVOF spraying of the developed FeMoNiCrB–(Ti, Cr)C and FeMoNiCrB–FeTiO<sub>3</sub> coatings to strengthen and restore surfaces operating in aggressive environments and those subjected to fretting corrosion.

**KEYWORDS:** HVOF spraying, amorphous phase, amorphous iron-based alloy, composition coating, corrosion resistance, fretting corrosion

## INTRODUCTION

Compared to crystalline materials, materials with an amorphous structure as a result of absence of the grain boundaries and dislocations have such properties as high strength, high elasticity limit, wear and corrosion resistance [1]. Among the systems of amorphous metallic materials iron-based alloys are of great interest for application in industry, not only owing to their properties, but also due to relatively low cost and availability of the material [2]. More over, the lower cost or absence of Ni and Co in amorphizing iron-base alloy makes application of these alloys more cost-effective than that of standard nickel- and cobalt-based materials (such as self-fluxing alloys, Ni–Cr–B–Si, stellite alloys, etc.).

Application of amorphizing Fe-alloys, as materials for thermal spraying of coatings allows forming layers with amorphous and nanocrystalline surface on the part surface, which have protective properties. Coatings based on amorphous Fe-alloys are produced using the methods of plasma [3, 4], supersonic plasma [5], electric arc [6], detonation [7, 8], HVOF and HVOF [9, 10] processes. The produced coatings are

characterised by a combination of hardness, corrosion and wear resistance, ability to absorb neutrons and hydrophobicity, making them rather promising for application in different areas (defense, nuclear, oil and gas and other industries) [11].

Protective properties can be further improved by adding a small (up to 30 vol.%) quantity of ceramic particles (for instance, WC/Co, B<sub>4</sub>C, TiN, Al<sub>2</sub>O<sub>3</sub>, ZrO<sub>2</sub>, etc.) to the coating. Composite coatings of FeSiB–CrMo–TiN, FeCSiBPCrMoAl–B<sub>4</sub>C, FeCrMoCB–WC/Co, produced by plasma and HVOF spraying processes, have not only higher hardness, but also self-lubrication ability, demonstrating 2–5 times higher wear resistance compared to single-phase coatings [12–14]. It is shown [15] that addition of 20 wt.% ZrO to plasma coating based on FeCrMoCB increases the coating wear resistance two times under the conditions of sliding friction: its addition to plasma coating based on FCrMnBSi alloy improves the thermal protection properties [16]. Addition of 20 wt.% Al<sub>2</sub>O<sub>3</sub> to a coating of FeCrMoCB alloy spray-deposited by HVOF process, improves the wear and corrosion resistance of the coatings in 3.55 % NaCl environment by 2–3 times [17].

Copyright © The Author(s)

The objective of the work was investigation of the corrosion resistance and fretting corrosion resistance of composite coatings produced by high-velocity oxygen flame (HVOF) spraying by powders based on amorphizing FeMoNiCrB alloy, with addition of (Ti, Cr)C and FeTiO<sub>3</sub> hardening compounds to their composition.

## EXPERIMENTAL MATERIALS AND PROCEDURES

Used as materials for HVOF spraying of coatings was powder of amorphizing FeMoNiCrB alloy and composite cermet powders based on FeMoNiCrB alloy with strengthening additives of double carbide (Ti, Cr)C and iron titanate FeTiO<sub>2</sub>. Selection of strengthening components of the studied coatings was based on their corrosion resistance and tribological characteristics [18, 19]. Composite powders were produced by mechanical alloying in Activator 2SL planetary mill of powder mixtures, which consists of FeMoNiCrB alloy and additive of one of the following compounds: (Ti,Cr)C (solid solution of 24 vol.% Cr<sub>3</sub>C<sub>2</sub> in TiC) and FeTiO<sub>3</sub> (ilmenite). Content of strengthening components in the powder mixture was selected on the base of the recommendations on development of cermet coatings based on amorphous Fe-alloys, in keeping with which the optimal content of strengthening phases in cermet coating is 10–30 vol.% [12–17, 20]. Mechanical alloying (MA) resulted in formation of amorphous-nanocrystalline cermet powders based on oversaturated solid solution of Fe(Ni, Cr) with additives of strengthening phases. A detailed description of the process of mechanical alloying of powders of these compositions is given in work [12]. Table 1 gives the characteristic of powders, used in this work for HVOF-coatings.

HVOF spraying of coatings was performed in UVShGPN-M1 unit using the following technology parameters [22]: propane-butane pressure — 4 atm, oxygen pressure — 7 atm, air pressure — 6 atm, nitrogen pressure — 5 atm, spraying distance of 120 mm. To increase the strength of adhesion to the steel substrate FeMoNiCrB–(Ti, Cr)C and FeMoNiCrB–FeTiO<sub>3</sub> cermet coatings were sprayed on NiCr sublayer

(50–100 μm thickness), which was deposited by electric arc spraying process.

The structure of the coatings was studied by metallographic methods (NEOPHOT 32 microscope, fitted with an attachment for digital photography of SIGETA model); microdurometric analysis of the coatings was performed in microhardness meter PMT-3 at 50 g load on the indenter. X-ray diffraction analysis (XRD) was performed in DRON-3 diffractometer in CuK<sub>α</sub>-radiation with graphite monochromator at step displacement of 0.1° and 4c exposure time in each point 4c with further computer processing of the derived digital data. Phases identification was conducted using PSTM data base. Coating porosity was determined on metallographic sections by the method of image analysis (standard) ASTM B-276 using Image-Pro Plus.

Corrosion resistance of coatings deposited on samples from St3 500 μm thick were studied by potentiostatic method in P-5827M potentiometer at sweep rate of 2 mV/s in the solutions of 10 % H<sub>2</sub>SO<sub>4</sub>, 3 % NaCl and in 10 % KOH. These electrolyte were selected for studying the influence of the nature of the aggressive environment (different kind of anions) on the corrosion processes. Chlorine-silver electrode was used as the electrode, with platinum as an auxiliary electrode. Experimental values were used to plot the cathode and anode polarisation curves in the following coordinates:  $E = E_c = f(\lg i)$ , where  $E_c$  is the corrosion potential, V;  $i_c$  is the current, A/cm<sup>2</sup> [23, 24]. The corrosion current and corrosion potential were determined by the graphic method by the polarisation curves by extrapolation of tafel areas of the cathode and anode curves to  $E = E_c$ . Corrosion current values were used to calculate the massometric ( $K_w$ ) and depth ( $K_d$ ) corrosion values were calculated by formulas of [23]:

$$K_w = \frac{i \cdot A \cdot 1000}{n \cdot F},$$

where  $K_w$  is the weight index of corrosion, g/m<sup>2</sup>·h;  $I$  is the corrosion current, A/cm<sup>2</sup>;  $A$  is the atomic weight of metal, g/mol, (for iron and steel  $A = 56$ );  $n$  is the valence of metal ion, which moved into the solution (for iron  $n = 2$ );  $F$  is the Faraday number, 26.8 A·h/mole:

**Table 1.** Characteristics of powders for HVOF spraying of coatings

Composition, wt.%	Particle size, μm	Method of producing	Phase composition
FeMoNiCrB (36.2Fe–29.9Mo–23.6Ni–7.6Cr–2.7B)	<40	Melt atomisation by nitrogen	Fe(Ni, Cr), Fe <sub>2</sub> B, Mo <sub>2</sub> FeB <sub>2</sub> , CrB <sub>2</sub> solid solution
77FeMoNiCrB–23(Ti, Cr)C	<40	MA 1.5 h	Fe(Ni, Cr), Mo <sub>2</sub> FeB <sub>2</sub> , (Ti, Cr)C, TiC, Cr <sub>3</sub> C <sub>2</sub> solid solution, amorphous phase
75FeMoNiCrB–10FeTiO <sub>3</sub>	<40	MA 1.5 h	Fe(Ni, Cr), Mo <sub>2</sub> FeB <sub>2</sub> , FeTiO <sub>3</sub> solid solution, amorphous phase

$$K_i = K_w \frac{8.76}{\rho},$$

where  $K_i$  is the depth index of corrosion, mm/y;  $\rho$  is the metal density, g/cm<sup>3</sup> ( $\rho_{Fe} = 7.85$  g/cm<sup>3</sup>); 8.76 is the conversion factor for transition from the weight index of corrosion to calculation per 1 hour to depth index to 1 year, calculated from the number of hours per year (24 h × 365 = 8760 h) and divided by 1000.

Protective effect of coatings was evaluated using the corrosion deceleration coefficient  $\gamma$ :

$$\gamma = \frac{K_w(s)}{K_w(c)},$$

where  $\gamma$  is the corrosion deceleration coefficient;  $K_w(s)$  and  $K_w(c)$  are the weight indices of corrosion rate of steel and of coated steels in corrosive environments (g/m<sup>2</sup>·h).

Degree of protection from corrosion  $Z$  (%) was calculated by the following formula:

$$Z = \frac{K_w(s) - K_w(c)}{K_w(s)} \cdot 100 \%$$

Comparative characteristic of corrosion resistance was derived using a ten-point scale of assessment, based on application of the depth index of corrosion ( $K_d$ ) [23].

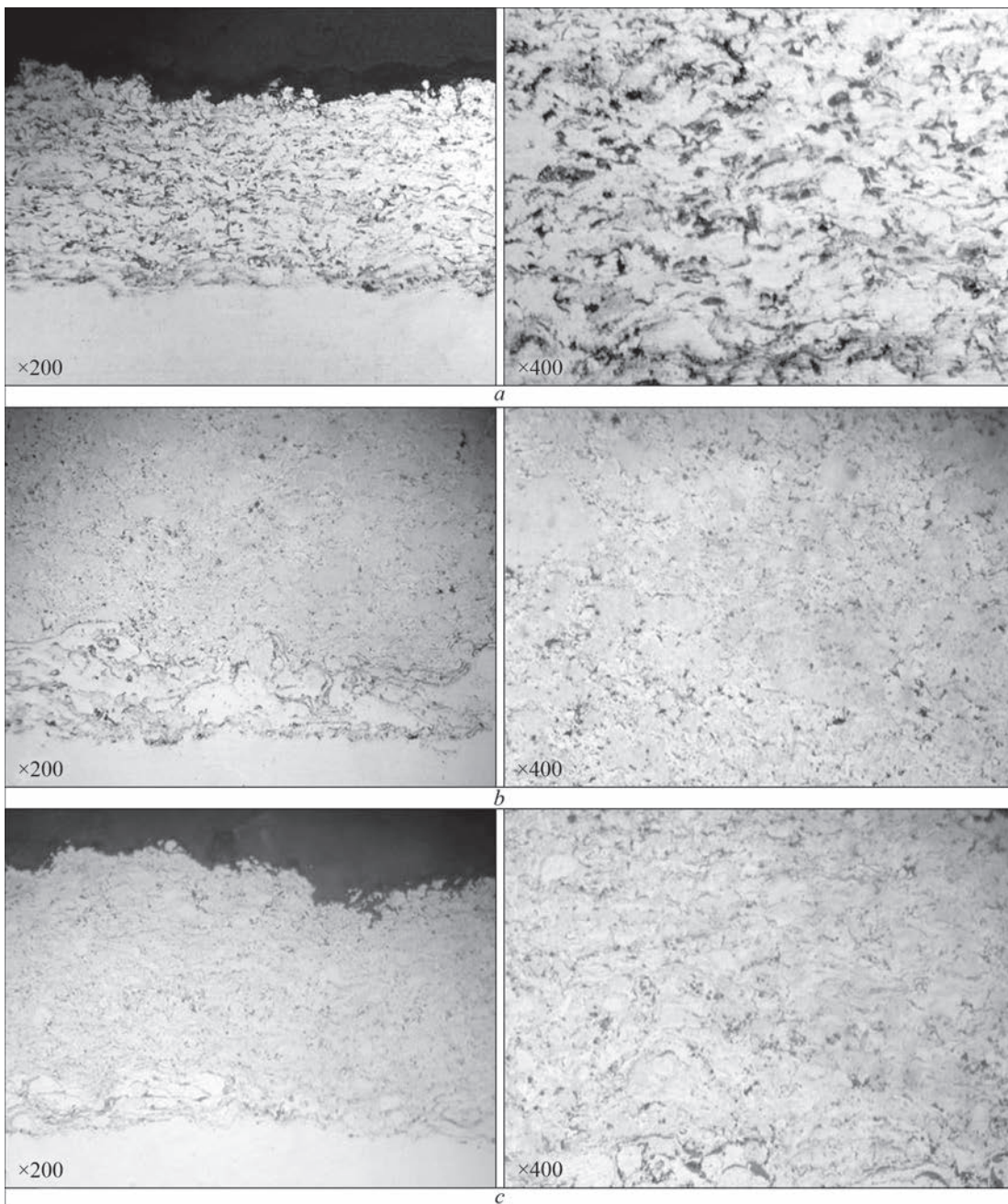


**Figure 1.** Microstructure of coatings produced by HVOF: *a* — FeNiCrMoB; *b* — FeNiCrMoB — (Ti, Cr)C; *c* — FeNiCrMoB–FeTiO<sub>3</sub>

Testing for evaluation of comparative wear resistance of the studied coatings was conducted under the conditions of fretting-corrosion wear. Coating thickness was 500  $\mu\text{m}$ , spraying was followed by machining with preservation of 300  $\mu\text{m}$  thickness, including the underlayer.

Conditions of vibrocyclic loading were as follows: amplitude of relative vibrational displacement of the samples  $A = 120 \mu\text{m}$ , specific load on the sample contact surfaces  $P = 20 \text{ MPa}$ , vibration frequency  $f = 25 \text{ Hz}$ , number of cycles of sample vibrational displacement (test base)  $n = 5 \cdot 10^5$  cycles. Samples were tested in air at temperature  $T = 293 \text{ K}$ . In each friction pair the samples with the studied coating were stationary, and countersamples from steel 45 quenched to the hardness of  $HRC \sim 48\text{--}50$  were mobile. OT4-1 titanium alloy was the basic variant for wear-resistant comparison. Sample wear was determined by the linear method after testing.

## INVESTIGATION RESULTS AND THEIR DISCUSSION

Investigations of the microstructure of HVOF coatings (Figure 1) showed that dense coatings of uniform thickness form at spraying of powders both from FeMoNiCrB alloy and FeMoNiCrB-(Ti, Cr)C and FeNiCrMoB-FeTiO<sub>3</sub> composite powders. Porosity and microhardness of coatings FeMoNiCrB, FeMoNiCrB-(Ti, Cr)C and FeNiCrMoB-FeTiO<sub>3</sub> are equal to 3.4, 2.4, 1.2 % and 4390, 5510 and 4410 MPa, respectively. Coatings have a fine-grained structure typical for HVOF, which is formed from completely molten particles, which spread and solidified, and partially deformed particles, having an oval or close to the

spherical shape. Interlayers of a dark-gray colour are observed on the boundaries of partially deformed particles, which is a result of interaction of the powder particles with oxygen and formation of oxide layers during spraying.

XRD analysis (Figure 2) revealed that multiphase coatings with an amorphous-crystalline structure form as a result of HVOF of powders based on FeMoNiCrB alloy.

Phase composition of the produced coatings is somewhat different from that of the initial powders. At spraying of crystalline FeMoNiCrB powder its partial amorphisation takes place, which is evidenced by the presence of a halo from the amorphous phase in the roentgenograph (Figure 2, *a*). At spraying of composite powders the interaction of the initial FeMoNiCrB alloy with the strengthening additives takes place with formation of Fe<sub>2</sub>Ti phase in FeNiCrMoB-(Ti, Cr)C coating (Figure 2, *b*) and of NiTi phase in FeNiCrMoB-FeTiO<sub>3</sub> (Figure 2, *c*). Iron oxides are present in all the coatings, and in FeMoNiCrB-(Ti, Cr)C and FeNiCrMoB-FeTiO<sub>3</sub> composite coatings they are found in a small quantity. It should be noted that due to formation of hard phase of titanium carbonitride in FeNiCrMoB-(Ti, Cr)C coating it has a somewhat higher (by 1100 MPa FeNiCrMoB) microhardness, compared to FeNiCrMoB coatings.

The characteristic of HVOF coatings based on FeMoNiCrB alloy is given in Table 2.

Investigations of the kinetics of electrode potential of FeMoNiCrB-based coatings showed that the stationary potential value is stabilised after 15–40 min.

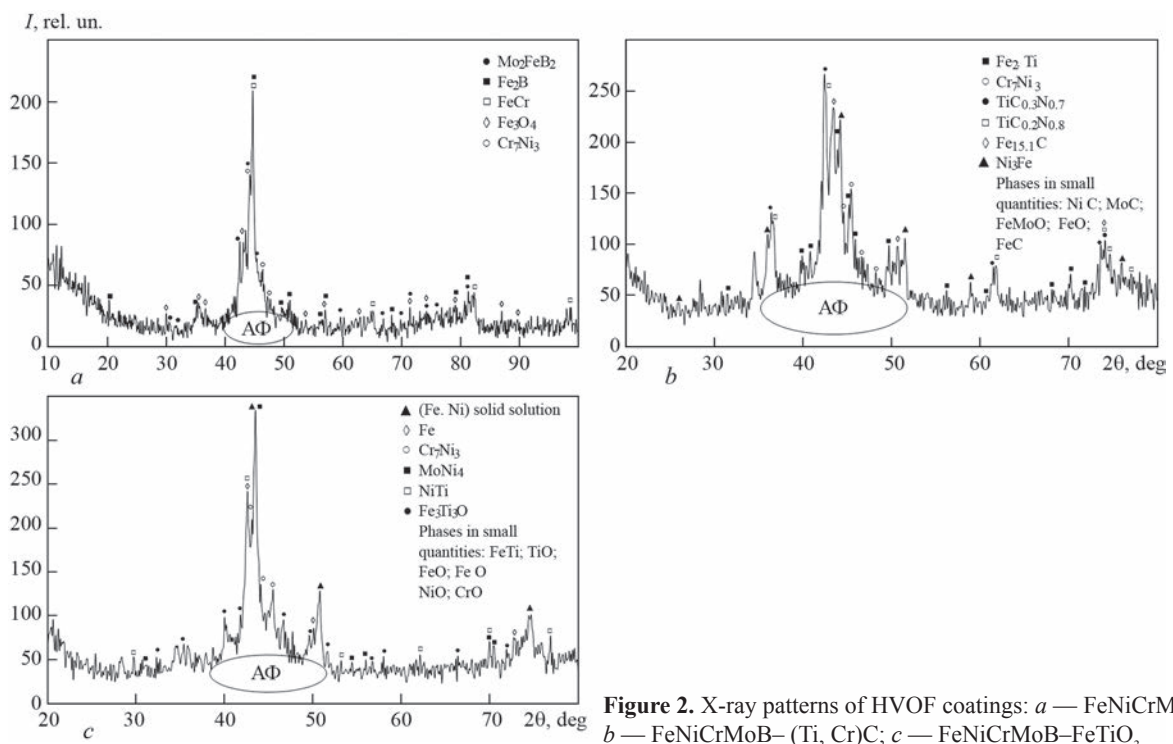


**Figure 2.** X-ray patterns of HVOF coatings: *a* — FeNiCrMoB; *b* — FeNiCrMoB-(Ti, Cr)C; *c* — FeNiCrMoB-FeTiO<sub>3</sub>

**Table 2.** Characteristics of coatings based on FeMoNiCrB alloy, produced by the method of HVOF spraying

Coating material	Porosity, %	Microhardness $HV_{0.05}$ , MPa	Phase composition
FeMoNiCrB	$3.4 \pm 0.7$	$4390 \pm 290$	$Mo_2FeB_2$ ; $Fe_2B$ ; $FeCr$ ; $Fe_3O_4$ ; $Cr_7Ni_3$ amorphous phase
FeMoNiCrB-(Ti, Cr)C	$2.4 \pm 0.4$	$5510 \pm 250$	$Fe_2Ti$ ; $Cr_7Ni_3$ ; $TiC_{0.3}N_{0.7}$ ; $TiC_{0.2}N_{0.8}$ ; $Fe_{15.1}C$ ; $Ni_3Fe$ ; amorphous phase; phases in small quantities: $Ni_3C$ ; $MoC$ ; $FeMoO_4$ ; $FeO$ ; $FeC_8$
FeMoNiCrB- $FeTiO_3$	$1.2 \pm 0.3$	$4410 \pm 190$	Solid solution (Fe, Ni); $Cr_7Ni_3$ ; $MoNi_4$ ; $NiTi$ ; $Fe_3Ti_3O_5$ ; amorphous phase; phases in small quantities: $FeTi$ ; $TiO$ ; $FeO$ ; $Fe_3O_4$ ; $NiO$ ; $CrO$

**Table 3.** Results of electrochemical tests of HVOF-coatings

Coating	3 % NaCl			10 % $H_2SO_4$			10 % KOH		
	$E_{\eta}$ , V	$E_c$ , V	$i_c$ , A/cm <sup>2</sup>	$E_{\eta}$ , V	$E_c$ , V	$i_c$ , A/cm <sup>2</sup>	$E_{\eta}$ , V	$E_c$ , C	$i_c$ , A/cm <sup>2</sup>
FeMoNiCrB	-0.43	-0.44	$6.5 \cdot 10^{-4}$	-0.2	-0.18	$5.8 \cdot 10^{-5}$	-0.44	-0.4	$5 \cdot 10^{-4}$
FeMoNiCrB-(TiCr)C	-0.38	-0.34	$4.3 \cdot 10^{-6}$	-0.06	-0.04	$4.2 \cdot 10^{-5}$	-0.50	-0.48	$4.2 \cdot 10^{-6}$
FeMoNiCrB- $FeTiO_3$	-0.34	-0.3	$2.9 \cdot 10^{-6}$	-0.06	-0.05	$2.5 \cdot 10^{-5}$	-0.56	-0.53	$4 \cdot 10^{-6}$
Uncoated St3 sample	-0.52	-0.5	$2 \cdot 10^{-5}$	-0.24	-0.22	$3 \cdot 10^{-3}$	-0.6	-0.58	$4 \cdot 10^{-5}$

On the coating surface the corrosion potential shifts to the positive side, compared to St3 sample, corrosion current decreases by one-two orders, and deceleration of both the cathode and the anode process takes place (Figure 3). In 10 %  $H_2SO_4$  solution a lowering of hydrogen overvoltage occurs on the coating surface, in 3 % NaCl solution and 10 % KOH solution inhibition of oxygen reduction process takes place (Figure 3). Irrespective of the coating composition, in 3 % NaCl solution the cathode and anode polarisation curves have practically the same shape, in 10 %  $H_2SO_4$  solution and in 10 % KOH solution passive areas appear on anode polarisation curves. No pittings or crevices are observed on the surface of coated samples after exposure to these solutions. After cleaning the surfaces become darker which is indicative of anodic dissolution process.

Analysis of the obtained results shows that for all the studied coatings the corrosion current in 3 % NaCl (Ph 7) and in 10 % KOH (pH 11) is by an order of magnitude higher than that in 10 %  $H_2SO_4$  (pH 2–3)

solution, i.e. the corrosion rate correlates with the solution pH. The corrosion resistance is also influenced by a change in the nature of depolarisation of the corrosion process (from hydrogen in the sulphate acid solution to predominantly oxygen one in 3 % solution of sodium chloride and in alkali solution).

Electrochemical studies in 3 % NaCl solution showed that in the coated samples the corrosion current decreases by an order compared to uncoated St3 samples (from  $2 \cdot 10^{-5}$  for steel to  $2.9\text{--}6.5 \cdot 10^{-6}$  A/cm<sup>2</sup> for coatings) (Table 3). Absence of passivation in 3 % NaCl solution can be due to the fact that this solution is aggressive with a high  $Cl^-$ , in the presence of which gradual driving of oxygen from the protective film on the electrode surface takes place, and by the impossibility of passive film formation. In 10 %  $H_2SO_4$  solution on the coating surface, the corrosion potential shifts to passive state region, corrosion current decreases by two orders ( $3 \cdot 10^{-3}$  for steel to  $2.5\text{--}5.8 \cdot 10^{-5}$  A/cm<sup>2</sup>) for coatings compared to uncoated St3 samples. Investigations of coatings in 10 % KOH solution showed that, compared to uncoated

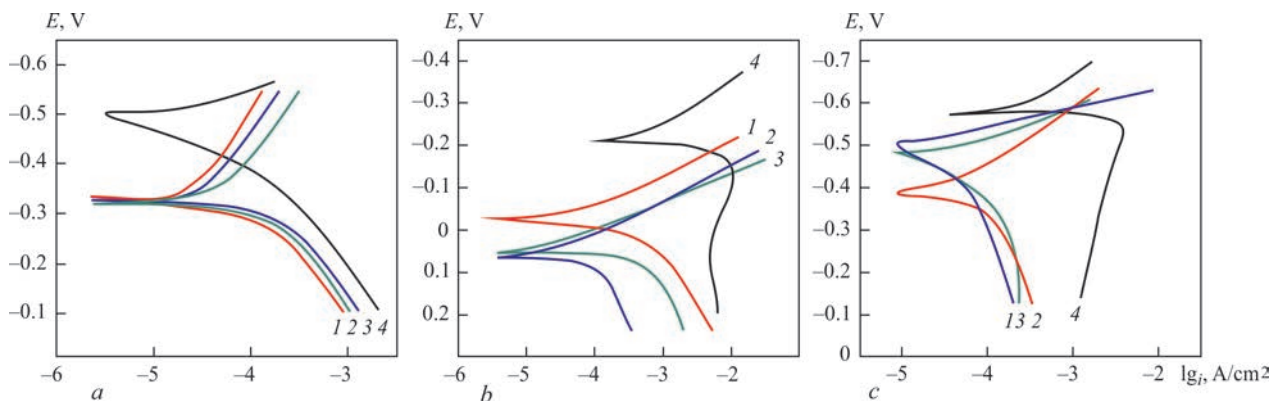


**Figure 3.** Polarisation curves of HVOF coatings in 3 % NaCl solution (a), in 10 %  $H_2SO_4$  solution (b); in 10 % KOH solution (c)

**Table 4.** Corrosion resistance of HVOF-coatings in 3 % NaCl solution

Coating	$K_w$ , g/m <sup>2</sup> ·h	$K_c$ , mm/year	$\gamma$	Z, %	Corrosion resistance rating
FeMoNiCrB	0.052	0.05	5.8	82.7	4
FeMoNiCrB-(TiCr)C	0.036	0.04	7.3	86.3	4
FeMoNiCrB-FeTiO <sub>3</sub>	0.031	0.032	9.0	89.2	4
Uncoated St3 sample	–	0.293	–	–	6

**Table 5.** Corrosion resistance of HVOF-coatings in 10 % H<sub>2</sub>SO<sub>4</sub> solution

Coating	$K_w$ , g/m <sup>2</sup> ·h	$K_c$ , mm/year	$\gamma$	Z, %	Corrosion resistance rating
FeMoNiCrB	0.18	0.16	3.6	72.2	6
FeMoNiCrB-(TiCr)C	0.16	0.15	3.9	74.3	6
FeMoNiCrB-FeTiO <sub>3</sub>	0.12	0.11	5.3	81.1	6
Uncoated St3 sample	–	0.59	–	–	7

**Table 6.** Corrosion resistance of HVOF-coatings in 10 % KOH solution

Coating	$K_w$ , g/m <sup>2</sup> ·h	$K_c$ , mm/year	$\gamma$	Z, %	Corrosion resistance rating
FeMoNiCrB	0.05	0.056	8.2	87.8	4
FeMoNiCrB-(TiCr)C	0.044	0.048	9.5	89.4	4
FeMoNiCrB-FeTiO <sub>3</sub>	0.042	0.047	9.7	89.6	4
Uncoated St3 sample	–	0.34	–	–	6

St3 samples, the corrosion current decreases by an order of magnitude (from  $4 \cdot 10^{-5}$  for steel to  $4\text{--}5 \cdot 10^{-6}$  A/cm<sup>2</sup> for coatings).

It was found that at application of composite powders with additives of (Ti, Cr)C and FeTiO<sub>3</sub> the corrosion resistance in the studied solutions increases 1.2–2.3 times, compared to a coating from FeMoNiCrB. The highest corrosion resistance is found in FeMoNiCrB-FeTiO<sub>3</sub> coating that may be related to its low porosity and presence of NiTi compounds and Fe<sub>3</sub>Ti<sub>3</sub>O complex oxide in its phase composition, which increase the corrosion resistance (Table 2).

Values of corrosion currents, calculated from polarisation curves, allowed calculation of the weight and depth indices of corrosion (Tables 4–6).

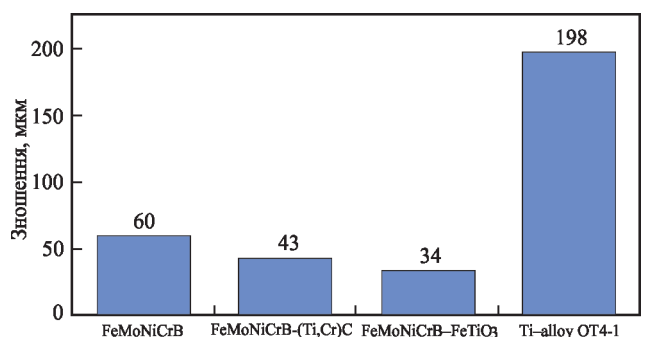
By ten point scale of corrosion resistance [24] amorphous coatings based on FeMoNiCrB alloy in 3 % NaCl solution and in 10 % KOH solution have resistance point 4 and belong to the “resistant” group, in 10 % H<sub>2</sub>SO<sub>4</sub> solution they have resistance point 6 and belong to “lower resistance” group.

Conducted electrochemical testing showed that at deposition of composition coatings based on FeMoNiCrB, the rate of St3 corrosion in 3 % NaCl solution, in 10 % H<sub>2</sub>SO<sub>4</sub> solution and in 10 % KOH solution decreases

by 7.3–9, 3.9–5.3 and 9.5–9.7 times, respectively. Degree of protection here is equal to 86.3–89.2, 74.3–81.1 and 89.4–89.6 %, respectively.

Results of the conducted investigations of HVOF coatings based on FeMoNiCrB alloy are indicative of their corrosion resistance in 3 % NaCl solution at the level of VT-6 alloy ( $i_c \sim 10^{-6}$  A/cm<sup>2</sup>) [25].

Results of investigations of the coatings for fretting corrosion resistance (Figure 4) showed that wear resistance of HVOF coatings from FeMoNiCrB, FeNiCrMoB-(Ti, Cr)C and FeNiCrMoB-FeTiO<sub>3</sub> is higher than that of OT4-1 titanium alloy by 3.3, 4.6 and 5.8 times, respectively. Such a high wear resistance of the


**Figure 4.** Results of investigations of HVOF-coatings for fretting corrosion resistance

coatings is achieved due to the specific structure of the coatings of heterogeneous type, where hard inclusions are uniformly distributed in a softer ductile matrix. Under the conditions of fretting corrosion and under the impact of high specific loads in service the ductile matrix is easily transferred to the connected surface, protects it from damage and promoted stress relaxation [26]. Presence of dispersed hard inclusions that take the main force load, results in the increase of fatigue fracture resistance of contacting materials.

In keeping with the results of the conducted investigations, the most fretting-resistant is FeNiCrMoB–FeTiO<sub>3</sub> coating, and the sequences of increase of HVOF coating resistance are as follows: FeMoNiCrB → FeNiCrMoB–(Ti, Cr)C → FeNiCrMoB–FeTiO<sub>3</sub>. Such a regularity is, obviously, related to the relative pore content in the coatings, as porosity decreases the coatings resistance under the conditions of friction without lubricants, considering that pores are stress raisers and microcrack nuclei.

Proceeding from the conducted investigations of protective properties, the produced composite amorphizing HVOF coatings based on FeMoNiCrB alloy can be proposed to improve the durability of the parts of machines and mechanisms, exposed to aggressive environments and prone to fracture at fretting-corrosion, in particular, for protection of titanium parts of aviation equipment.

## CONCLUSIONS

The method of high-velocity oxygen flame spraying of mechanically-alloyed powders based on amorphizing FeMoNiCrB alloy with additives of (Ti, Cr)C and FeTiO<sub>3</sub> compounds was used to produce dense heterogeneous coatings with not more than 3 % porosity. Results of phase analysis of FeMoNiCrB–(Ti, Cr)C and FeMoNiCrB–FeTiO<sub>3</sub> coatings demonstrate their amorphous-crystalline structure.

Corrosion resistance of thermally-sprayed composite coatings based on FeMoNiCrB alloy measured in the solutions of 3 % NaCl, 10 % H<sub>2</sub>SO<sub>4</sub> and 10 % KOH, by the deep corrosion indices exceeds St3 steel durability 7.3–9; 3.9–5.3 and 9.5–9.7 times, respectively, with the values of 0.032–0.04; 0.11–0.15 and 0.047–0.048 mm/y. By the index of corrosion current the obtained amorphous coatings have corrosion durability at the level of titanium alloy VT-6 ( $i_c \sim 10^{-6}$  A/cm<sup>2</sup>).

Determination of fretting-corrosion resistance of the coatings showed that wear resistance of FeMoNiCrB–(Ti, Cr)C and FeMoNiCrB–FeTiO<sub>3</sub> cermet coatings is 4.6 and 5.8 times higher than that of OT4-1 titanium alloy, making these coatings promising at application for strengthening the parts of aviation equipment components, prone to fretting-corrosion.

## REFERENCES

1. Stachurski, Z.H. (2011) On Structure and properties of amorphous materials. *Materials*, **4**(9), 1564–1598. DOI: <https://doi.org/10.3390/ma4091564>
2. Hashimoto, K. (2011) What we have learned from studies on chemical properties of amorphous alloys. *Applied Surface Science*, **257**(19), 8141–8150. DOI: <https://doi.org/10.1016/j.apsusc.2010.12.142>
3. An, Y., Hou, G., Chen, J. et al. (2014) Microstructure and tribological properties of iron-based metallic glass coatings prepared by atmospheric plasma spraying. *Vacuum*, **107**, 132–140. DOI: <https://doi.org/10.1016/j.vacuum.2014.04.021>
4. Yugeswaran, S., Kobayashi, A. (2014) Metallic glass coatings fabricated by gas tunnel type plasma spraying. *Vacuum*, **110**, 177–182. DOI: <https://doi.org/10.1016/j.vacuum.2014.04.016>
5. Li, G., Gan, Y., Liu, C. et al. (2020) Corrosion and wear resistance of Fe-based amorphous coatings. *Coatings*, **10**(1), 73. DOI: <https://doi.org/10.3390/coatings10010073>
6. Lin, J., Wang, Z., Lin, P. et al. (2014) Microstructure and cavitation erosion behavior of FeNiCrBSiNbW coating prepared by twin wires arc spraying process. *Surface and Coatings Technology*, **240**, 432–436. DOI: <https://doi.org/10.1016/j.surfcoat.2013.12.07>
7. Artemchuk, V.V. (2011) Structure and properties of Fe-based amorphous detonation coatings. *Visnyk Dnipro. Nats. Un-tu Zalozn. Transportu*, **36**, 39–44. DOI: <https://doi.org/10.15802/stp2011/8707>
8. Borysov, Yu.S., Borysova, A.L., Tsybalyista, T.V. et al. (2021) Producing and properties of detonation coatings based on FeMoNiCrB amorphizing alloy with addition of strengthening phases. *The Paton Welding J.*, **12**, 29–35. DOI: <https://doi.org/10.37434/as2021.12.05>
9. Ma, H.R., Chen, X.Y., Li, J.W. et al. (2016) Fe-based amorphous coating with high corrosion and wear resistance. *Surface Engineering*, **33**(1), 56–62. DOI: <https://doi.org/10.1080/02670844.2016.1176718>
10. Wang, G., Huang, Z., Xiao, P., Zhu, X. (2016) Spraying of Fe-based amorphous coating with high corrosion resistance by HVOF. *J. of Manufacturing Processes*, **22**, 34–38. DOI: <https://doi.org/10.1016/j.jmapro.2016.01.009>
11. Liu, L., Zhang, C. (2014) Fe-based amorphous coatings: Structures and properties. *Thin Solid Films*, **561**, 70–86. DOI: <https://doi.org/10.1016/j.tsf.2013.08.029>
12. Yugeswaran, S., Kobayashi, A., Suresh, K., Subramanian, B. (2013) Characterization of gas tunnel type plasma sprayed TiN reinforced Fe-based metallic glass coatings. *J. of Alloys and Compounds*, **551**, 168–175. DOI: <https://doi.org/10.1016/j.jallcom.2012.09.111>
13. Yoon, S., Kim, J., Kim, B.D., Lee, C. (2010) Tribological behavior of B<sub>4</sub>C reinforced Fe-base bulk metallic glass composite coating. *Surface and Coatings Technology*, **205**(7), 1962–1968. DOI: <https://doi.org/10.1016/j.surfcoat.2010.08.078>
14. Terajima, T., Takeuchi, F., Nakata, K. et al. (2010) Composite coating containing WC/12Co cermet and Fe-based metallic glass deposited by high-velocity oxygen fuel spraying. *J. of Alloys and Compounds*, **504**, S288–S291. DOI: <https://doi.org/10.1016/j.jallcom.2010.03.209>
15. Chu, Z., Yang, Y., Chen, X. et al. (2016) Characterization and tribology performance of Fe-based metallic glassy composite coatings fabricated by gas multiple-tunnel plasma spraying. *Surface and Coatings Technology*, **292**, 44–48. DOI: [10.1016/j.surfcoat.2016.03.024](https://doi.org/10.1016/j.surfcoat.2016.03.024)
16. Zhou, Z., Han, F.-X., Yao, H.-H. et al. (2021) Novel Fe-based amorphous composite coating with a unique interfacial layer improving thermal barrier application. *ACS Applied Ma-*

- terials & Interfaces*, 13(19), 23057–23066. DOI: <https://doi.org/10.1021/acsami.0c22868>
17. Yasir, M., Zhang, C., Wang, W. et al. (2015) Wear behaviors of Fe-based amorphous composite coatings reinforced by Al<sub>2</sub>O<sub>3</sub> particles in air and in NaCl solution. *Materials & Design*, **88**, 207–213. DOI: <https://doi.org/10.1016/j.matdes.2015.08.142>
  18. Umanskii, A.P., Konoval, V.P., Panasyuk, A.D. et al. (2007) Plasma coatings of (TiCrC)–(FeCr) composite powder alloys: Structure and properties. *Powder Metallurgy and Metal Ceramics*, **46(3–4)**, 133–138. DOI: <https://doi.org/10.1007/s11106-007-0022-8>
  19. Abdou, M.I., Ayad, M.I., Diab, A.S.M. et al. (2017) Influence of surface modified ilmenite/melamine formaldehyde composite on the anti-corrosion and mechanical properties of conventional polyamine cured epoxy for internal coating of gas and oil transmission pipelines. *Progress in Organic Coatings*, **113**, 1–14. DOI: <https://doi.org/10.1016/j.porgcoat.2017.08.003>
  20. Surzhenkov, A., Antonov, M., Goljandin, D. et al. (2013) Sliding wear of TiC–NiMo and Cr<sub>3</sub>C<sub>2</sub>–Ni cermet particles reinforced FeCrSiB matrix HVOF sprayed coatings. *Estonian J. of Engineering*, **19(3)**, 203–211. DOI: <https://doi.org/10.3176/eng.2013.3.03>
  21. Borysov, Yu.S., Borysova, A.L., Burlachenko, O.M. (2021) Composite powders based on FeMoNiCrB amorphizing alloy with additives of refractory compounds for thermal spraying of coatings. *The Paton Welding J.*, **11**, 38–47. DOI: <https://doi.org/10.37434/tpwj2021.11.07>
  22. Borysov, Yu.S., Vihilianska, N.V., Demianov, I.A. et al. (2022) Studies of coatings produced by high-velocity oxy-fuel spraying using cermet powder based on FeMoNiCrB amorphizing alloy. *The Paton Welding J.*, **2**, 33–36. DOI: <https://doi.org/10.37434/as2022.02.05>
  23. Pokhmurskyi, V.I., Khoma, M.S. (2008) *Corrosion fatigue of metals and alloys*. Lviv, SPOLOM [in Ukrainian].
  24. Alimov, V.I., Duryagina, Z.A. (2012) *Corrosion and corrosion protection of metals*. Donetsk, Skhidnyi Vydavnychyi Dim [in Ukrainian].
  25. Tomashov, N.D., Chernova, G.P., Kornienko, L.P. (1982) *Corrosion resistance of titanium in technological environments of chemical industry*. Moscow, NII Tekhim [in Russian].
  26. Hariharasakthisudhan, P., Rajan, B.S., Sathickbasha, K. (2020) Inspiration of reinforcements, manufacturing methods, and microstructural changes on wear behavior of metal matrix composites — a recent review. *Materials Research Express*, **7(1)**, 012006. DOI: <https://doi.org/10.1088/2053-1591/ab6918>

#### ORCID

N.V. Vihilianska: 0000-0001-8576-2095,  
 C. Senderowski: 0000-0002-0331-3702,  
 K.V. Yantsevych: 0000-0002-3975-7727,  
 O.I. Dukhota: 0000-0001-8091-1717

#### CONFLICT OF INTEREST

The Authors declare no conflict of interest

#### CORRESPONDING AUTHOR

N.V. Vihilianska  
 E.O. Paton Electric Welding Institute of the NASU  
 11 Kazymyr Malevych Str., 03150, Kyiv, Ukraine.  
 E-mail: [pewinataliya@gmail.com](mailto:pewinataliya@gmail.com)

#### SUGGESTED CITATION

N.V. Vihilianska, C. Senderowski, K.V. Yantsevych, O.I. Dukhota (2023) Properties of coatings produced by HVOF spraying of composite powders based on amorphizing FeMoNiG13 alloy. *The Paton Welding J.*, **6**, 24–31.

#### JOURNAL HOME PAGE

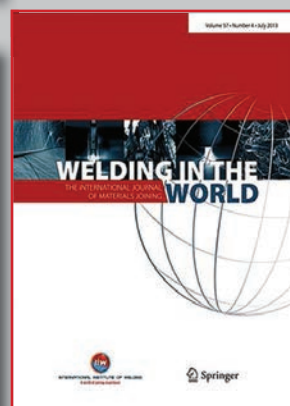
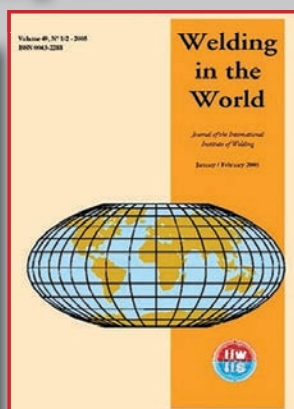
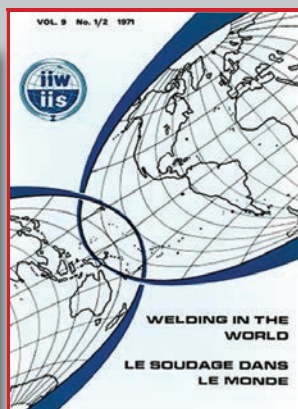
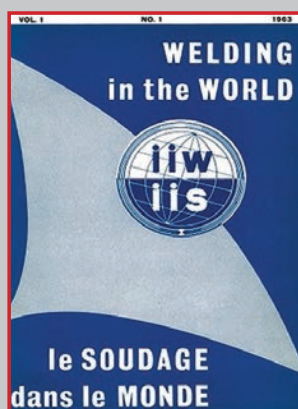
<https://patonpublishinghouse.com/eng/journals/tpwj>

Received: 03.05.2023

Accepted: 17.07.2023

## THE INTERNATIONAL INSTITUTE OF WELDING: 75 YEARS

The changing covers of *Welding in the World*



DOI: <https://doi.org/10.37434/tpwj2023.06.05>

# MATHEMATICAL MODELING OF RESIDUAL STRESS RELAXATION DURING PERFORMANCE OF POSTWELD HEAT TREATMENT

**O.V. Makhnenko, O.S. Milenin, O.F. Muzhychenko, S.M. Kandala,  
O.M. Savytska, G.Yu. Saprykina**

E.O. Paton Electric Welding Institute of the NASU  
11 Kazymyr Malevych Str., 03150, Kyiv, Ukraine

## ABSTRACT

In order to lower the level of residual stresses, welded joints of a number of structural steels are subjected to general or local postweld heat treatment by the high-temperature tempering mode. Mathematical modeling methods are widely used, alongside the experimental investigation methods, to satisfy the continuously growing requirements to welded joint quality and to optimize the welding technology. Mathematical modeling of the process of welded joint heat treatment is often performed using a simplified creep function by Norton–Bailey law at a fixed soaking temperature, but here the processes of ductile deformation taking place during slow prolonged heating and cooling, are ignored. The effectiveness of application of different models of temperature creep for mathematical modeling of the processes of relaxation of residual stresses in welded joints was studied in this work with the purpose of developing recommendations for their application for various characteristic cases of postweld heat treatment. Comparison of the results of modeling the process of stress relaxation performed on a number of examples, showed that the simplified creep function at short-term soaking during general furnace treatment can give an error compared to a more general creep model. Modeling of the local heat treatment technology revealed that the complex geometry of the component and poor choice of the heating element arrangement may lead to negative consequences, namely formation of new high residual stresses. Proper modeling of the processes of relaxation and redistribution of residual stresses in welded joints and structures as a result of general (furnace) or local post-weld heat treatment may optimize the process of furnace heat treatment and improve the quality and fatigue life of the welded structures.

**KEYWORDS:** postweld heat treatment, high-temperature annealing, residual welding stresses, stress relaxation, mathematical modeling, creep function

## INTRODUCTION

Provision of increasing industrial requirements to welded joint quality from point of view of their reliability is related with corresponding fundamental investigations of the main physical processes which determine quality of mentioned above products after manufacture and some period of operation. Methods of mathematical modeling and current information technologies have found wide application alongside the experimental investigations.

Welded joints of a series of structural steels (ferrite-pearlite, bainite, martensite classes), in particular, welded joints of large thicknesses are subjected to general (in furnace) or local heat treatment (HT) by high-temperature tempering mode to decrease the level of residual welding stresses [1, 2]. This technological operation is particularly necessary in the case when a structure is going to be operated at low temperatures, cyclic loads, in aggressive medium, i.e. when a role of residual stresses in provision of structural integrity can become very important [3, 4].

The modes of postweld HT are not always optimum. In series of cases of application of local or general tempering of welded joints the residual stresses

during heating can partially relax, but after that in cooling the new ones form if heating or cooling of joint material was nonuniform [5, 6] or thermal-physical properties of materials do not match as in the case of dissimilar joints and deposits [7, 8]. Therefore, development of the proper modes of postweld HT technology, in particular, using mathematical modeling methods, can allow significant decrease of material expenses related with provision of safe operation of critical equipment. Thus, the aim of the work is investigation of efficiency of application of different models of temperature creep for mathematical modeling of processes of relaxation of residual stresses in welded joints and development of recommendations on their application for different typical cases of postweld HT.

## METHODOLOGY

On the strain plasticity theory there is dependence between deformation and stresses for elastic-plastic body. Strain intensity for an isotropic body equals a sum of plastic and elastic strains intensities [9, 10]. Plastic strain, which increases with time at constant stress, is called a creep strain ( $\varepsilon^c$ ). Graphic presentation of dependence of plastic strain on time  $t$  of tests in case of effect of constant stresses and temperature is called a creep curve (Figure 1) [9].

In the general case of thermomechanical loading a nature and value of deformations of product is determined using the data on elasticity modulus, Poisson's coefficient, material yield point depending on temperature as well as rate of creep strain of material at set temperature depending on values of loads (stresses).

In welded elements subjected to HT the total effect of high temperatures and inner residual stresses provoke appearance and development of elastic-plastic strains. For mathematical model used in modeling of elastic-plastic deformation of material of welded joint it is assumed that increment of tensor of strain  $d\varepsilon_{ij}$  in a random point  $(x, y, z)$  in moment of time  $t$  is presented in form of sum [3]:

$$d\varepsilon_{ij} = d\varepsilon_{ij}^e + d\varepsilon_{ij}^p + d\varepsilon_{ij}^c, \quad (1)$$

where  $d\varepsilon_{ij}^e$  is the elastic component of strain tensor;  $d\varepsilon_{ij}^p$  is the component from instant plasticity and  $d\varepsilon_{ij}^c$  is the component of creep strain (diffusion plasticity). A function of material creep corresponding to Norton–Bailey [11] law is often used for modeling of a process of heat treatment of welded joints. It is a power dependence between the stress intensity  $\sigma_i$  and creep rate at fixed soaking temperature of HT:

$$\frac{d\varepsilon^c}{dt} = A\sigma_i^n, \quad (2)$$

or in modified shape with additional effect of soaking time  $t$  [12]

$$\frac{d\varepsilon^c}{dt} = A\sigma_i^n t^m, \quad (3)$$

where  $A$ ,  $n$ ,  $m$  are the coefficients which determine experimentally the characteristics of material at set temperature  $T = \text{const}$ .

Provided model is developed for prediction of accumulation of creep strain depending on time on stage I of non-steady-state creep and stage II of steady-state creep (Figure 1) that corresponds to the conditions of deformation during postweld HT. However, application of such creep model in modeling of the processes of relaxation of residual stresses does not consider creep processes taking place at temperatures lower than temperature of soaking in HT, i.e. in heating and cooling of material or in the zones of welded joint where temperature of material during local HT is lower than the set soaking temperature.

Let's consider a mathematical model of Arrhenius creep that considers accumulation of creep strain in a wide range of material temperature [13].

$$\frac{d}{dt} = B\sigma_i^n \exp\left(\frac{Q}{T(K)}\right) = B\sigma_i^n \exp\left(\frac{G}{T(^{\circ}\text{C}) + 273}\right), \quad (4)$$

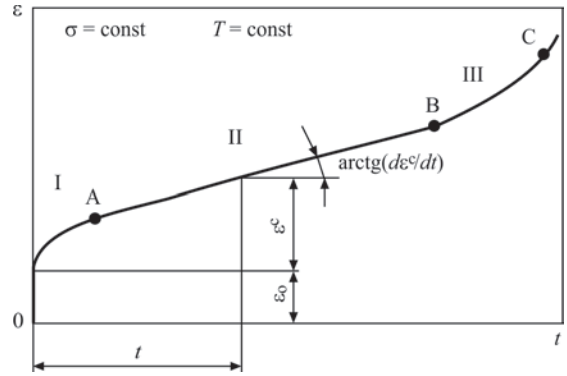


**Figure 1.** Creep curve: I — stage of non-steady-state creep; II — stage of steady-state creep; III — stage of failure;  $\varepsilon_0$  is the instant initial deformation

where  $Q$  is the energy of creep activation;  $k$  is the Boltzmann constant;  $T$  (K) is the absolute temperature by Kelvin scale;  $T$  ( $^{\circ}\text{C}$ ) is the temperature in Celsius degrees;  $B$ ,  $G$ ,  $n$  are the constants.

Provided creep model (4) at elevated temperatures is relatively general, it allows tracing deformation processes in HT. This model is effective in modeling of the processes of relaxation of residual stresses at local or furnace HT of welded structures in short-term soaking when uniform heating until the set soaking temperature is not provided on a volume of welded structure or assembly.

According to the provided models of high-temperature creep and known models of elastic-plastic deformation of material [3] it is possible to develop the mathematical models of joint development of elastic strains, instant plasticity and creep for high-temperature heating of elements as a result of postweld HT. Mostly in this case it is possible to use the current developments for solution of the problems of theory of elasticity and building mechanics based on wide application of finite elements method. A method of successive tracing allows taking into account the kinetics of development of stressed state not only from successively made welding passes, but also from operation of postweld HT. Reliability of the results obtained by described procedure to significant extent depends on output data on thermophysical and mechanical properties of material of tested object and parameters of heat and power effect.

Let's consider a series of examples of application of mathematical models of creep (1) and (4) in modeling of typical cases of postweld HT.

#### EXAMPLE No. 1. LONGITUDINAL WELDED JOINT OF CYLINDER SHELL OF IN-VESSEL CAVITY OF WWER-1000 REACTOR

In-vessel cavity (IVC) of nuclear reactor WWER-1000 is a welded cylinder shell from austenite steel 08Kh18N10T of outer diameter 3610 mm and wall

thickness 60 mm, that contains longitudinal and circumferential butt joints which can be produced by multipass submerged-arc welding with following HT for relaxation of residual stresses.

Distributions of the residual welding stresses [14] for longitudinal multipass welded joint (10–12 passes) of cylinder IVC shell were obtained using the mathematical modeling method. After welding a procedure of general (furnace) HT of welded joint was modeled for mode:  $T = 650\text{ }^\circ\text{C}$ , duration of soaking 10 h. For steel 08Kh18N10T at temperature  $T = 650\text{ }^\circ\text{C}$  the values of  $A$  and  $n$  coefficients in Norton–Bailey equation (2) were take as following [15]:

$$A = 6.07307 \cdot 10^{-14} \text{ MPa}^{-n}/\text{h}, n = 4.8351.$$

For this mathematical model parameters  $A$  and  $n$  were taken equal for the base and weld metal. Figure 2 shows a diagram of creep function for steel 08Kh18N10T at temperature  $T = 650\text{ }^\circ\text{C}$  and taken parameters  $A$  and  $n$ . It demonstrates that at high values of stress intensity (more than 100 MPa) formation of creep strains takes place with sufficiently high rate ( $0.0003\text{--}0.01\text{ h}^{-1}$ ). At low stresses the processes of their relaxation dramatically slow down.

Welded structure of IVC can be subjected to general furnace HT. Such HT can be modeled based on application of two fundamentally different approaches for determination of temperature distributions. First approach is simplified to the maximum and assumes that during heating, soaking and cooling the temperature of material is forcibly set equal to equilibrium on whole volume of welded assembly. Second approach takes into account possible nonuniformity of temperature distribution on structure thickness due to convective heating from surface.

The results of calculation of stress-strain state of IVC after welding and HT showed that the maximum axial stresses  $\sigma_{zz}$ , which equaled 200 MPa after welding, reduced to 48 MPa after HT. The maximum circumferential stresses  $\sigma_{\beta\beta}$  as a result of HT reduced from 174 to 50 MPa, radial  $\sigma_{rr}$  from 63 to 10 MPa.

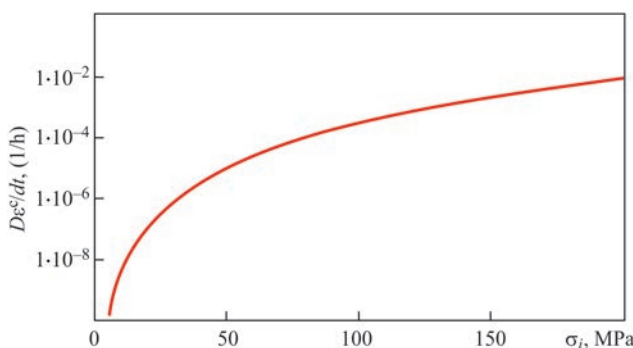


Figure 2. Creep function for 08Kh18N10T steel at  $T = 650\text{ }^\circ\text{C}$  temperature

Figure 3 shows the change of temperature of air in furnace volume, which correspond to the set parameters of HT as well as calculation results of kinetics of maximum temperature of heating of welded joint metal due to convective heat exchange and results of kinetics of relaxation of residual stresses  $\sigma_{zz}$  at different rates of heating and cooling. Coefficient of convective heat exchange on surface of welded joint with air in furnace volume was taken in a range  $\alpha = (1.5\text{--}$

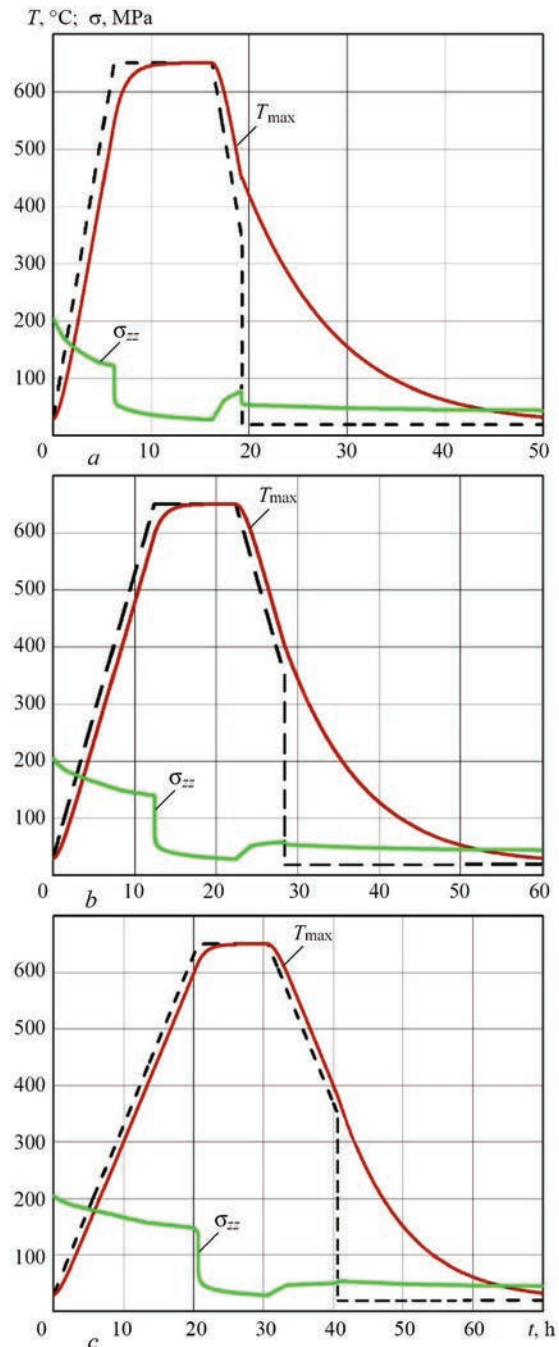
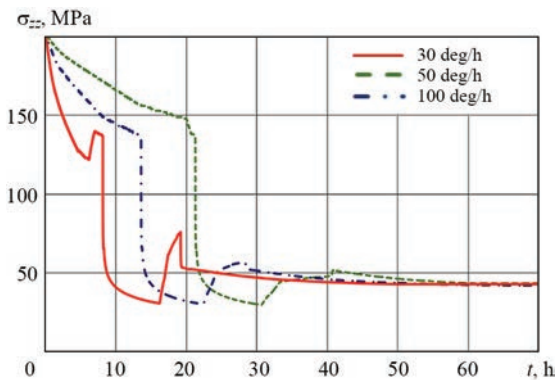


Figure 3. Change of air temperature in furnace (dashed line) and calculation results of kinetics of maximum temperature of heating of metal of welded joint and relaxation of maximum residual stresses (axial component  $\sigma_{zz}$ ) at different rates of heating and cooling: a — 100 deg/h; b — 50; c — 30



**Figure 4.** Kinetics of relaxation of maximum residual stresses  $\sigma_{zz}$  in HT in welded joint zone with different rates of heating and cooling (100, 50, 30 deg/h), soaking time 10 h,  $T_{\max} = 650$  °C, for model of convective heating in furnace

$3.0) \cdot 10^{-4}$  J/(mm<sup>2</sup>·s·deg) depending on temperature of heated metal.

Heating promotes relaxation of residual stresses due to instant plasticity and after heating to 650 °C during soaking this takes place due to the process of temperature creep. It should be noted that the developed simplified model uses an assumption that the creep process starts at soaking temperature. Thus, the creep process at 650 °C has sufficiently intensive start. Substantial stress relaxation takes place in course of first hour of soaking after that creep rate noticeably decreases. After cooling the level of residual stresses slightly rises due to increase of temperature dependence of material yield limit.

At considered variants of heating and cooling rates the welded joint of 60 mm thickness has uniform enough heating on thickness and differs by delay value at reaching the soaking temperature 650 °C. At sufficiently long period of soaking (10 h) that was taken in calculation the results by efficiency of relaxation of residual stresses for different heating and cooling rates virtually have no difference (Figure 4). Maximum  $\sigma_{zz}$ , which after welding were at 200 MPa level, reduce to 45–48 MPa after HT.

Figure 5 presents the dependence of efficiency of relaxation of residual welding stresses  $\sigma_{zz}$  on soaking time. The results of calculation in HT for a variant of convective heating in a furnace at heating rate up to 650 °C and cooling 100 deg/h show that soaking time is a very important parameter.

The difference in relaxation of residual stresses at 10 and 5 hours soaking is not large: residual stresses  $\sigma_{zz}$  decrease to 45 and 50 MPa, respectively. Efficiency of HT decreases at shorter soaking of 650 °C. At three h soaking  $\sigma_{zz}$  decreased to 60 MPa, for 2 h to 86 MPa.

Figure 6 provides a comparison of the results of modeling of relaxation of residual stresses  $\sigma_{zz}$  in HT in the case of forced uniform heating (approach 1) with the results of modeling of HT by heating due

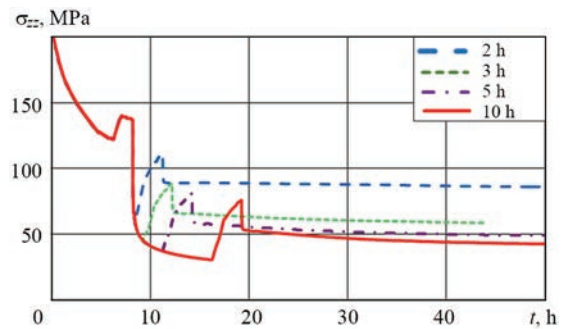


**Figure 5.** Kinetics of relaxation of maximum residual stresses  $\sigma_{zz}$  in HT in welded joint zone on soaking time (2, 3, 5, 10 h,  $T_{\max} = 650$  °C), at heating and cooling rate 100 deg/h for model of convective heating in furnace

to convection (approach 2) for soaking during 2 and 10 h at 650 °C, heating and cooling rate is 100 deg/h.

At sufficiently long-term soaking, when welded joint is completely heated on thickness, the results of numerical prediction of relaxation of residual stresses by simplified approach 1 are close to more accurate approach 2, which takes into account a level of heating on thickness and delay of heating to soaking temperature. Thus, at 10 h soaking the results of relaxation of the maximum residual stresses  $\sigma_{zz}$  (Figure 6), obtained by approaches 1 and 2, give 45 and 43 MPa, respectively. For short-term soaking (2 h) the simplified approach 1 gives significant error, namely 59 MPa against 86 MPa using more accurate approach 2, therefore, an error makes approximately 30 %.

## EXAMPLE No. 2. CIRCUMFERENTIAL WELDED JOINT OF PIPELINE FROM INCREASED STRENGTH STEEL OF PEARLITE CLASS

Welded joints of pipelines of power equipment are as a rule subjected to postweld HT. For example, welded joints of reactor coolant pipe (RCP) Du850 from steel 10GN2MFA (pearlite class) are made using manual or automatic welding. A weld root is made manually using argon-arc welding with filler wire 08G2S of

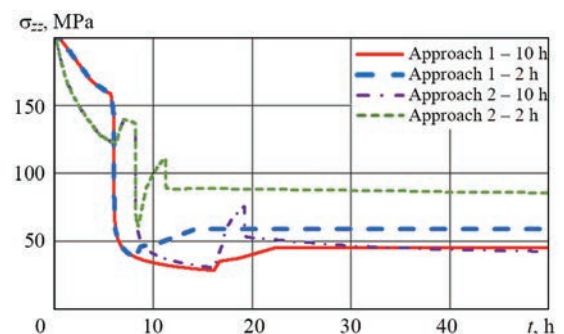


**Figure 6.** Comparison of conditions of forced uniform heating (approach 1) with heating due to convection (approach 2) in HT by the results of modeling of relaxation of maximum residual welding stresses  $\sigma_{zz}$  for different time of soaking 2 and 10 h,  $T_{\max} = 650$  °C, heating and cooling rate 100 deg/h

**Table 1.** Results of calculation of coefficients of creep functions (2) and (4) using experimental data [3]

$T, ^\circ\text{C}$	$A, 1/(\text{MPa}^n\cdot\text{h})$	$B, 1/(\text{MPa}^n\cdot\text{h})$	$G, \text{K}$
	$n = 6$	$n = 6$	$n = 6$
550	$0.43 \cdot 10^{-17}$	exp(41.28)	- 66394
600	$1.13 \cdot 10^{-15}$		
650	$1.73 \cdot 10^{-14}$		
700	$3.77 \cdot 10^{-12}$		

2–3 mm diameter, height of root pass is 6–8 mm. Filling of main part of the weld is carried out by manual welding with electrodes PT-30 of 4 mm diameter and wire Sv10GN1MA of 2 mm diameter is used at automatic welding. Welding is performed with preliminary and concurrent heating to 150 °C.

For determination of residual welding stresses there was carried out the mathematical modeling in 2D axially symmetric problem statement of the non-stationary heat conductivity and thermoplastic deformation in welding heating of a circumferential multi-pass welded joint (112 passes) of a cylinder shell with inner diameter  $D_{\text{inner}} = 850$  mm, thickness  $\delta = 60$  mm, mode of arc welding run  $I_w = 250$  A,  $U_w = 11.5$  V,  $v_w = 5.5$  mm/s,  $Q_1 = 520$  J/mm, coefficient of thermal efficiency equals 0.8.

There was obtained a sufficiently high level of circumferential component of residual stresses  $\sigma_{\beta\beta}$  up to 400–500 MPa, i.e. to a material yield limit and in a lo-

cal zone of final welding passes the maximum calculation circumferential stresses reach almost 690 MPa.

High-temperature tempering at 650 °C temperature is used after welding for the purpose of relaxation of residual stresses. Time of soaking at set temperature is 6–7 h, cooling to 200 °C in a furnace at set rate of cooling to 100 deg/h then free cooling to temperature 20 °C on air.

Two creep functions were used in modeling of the process of relaxation of residual stresses in HT for determination of possible difference of results and provision of necessary prediction accuracy. First — simplified (2), does not depend on temperature and acts only at reaching soaking temperature in HT. Second (4) — more general and depends on material temperature starting from temperature of 550°C and higher.

Coefficients of creep function for base material of RCP pipeline (steel 10GN2MFA) are determined based on processing of experimental data. Figure 7 provides the data of work [3] corresponding to the level of relaxation of tensile residual longitudinal stresses for soaking period 2 h HT after welding of plates of steel 10GN2MFA depending on tempering temperature  $T = 550\text{--}700$  °C. Table provides the results of calculation of constants  $A, B, G, n$  of creep functions (2) and (4) using these experimental data.

Simplified creep function can be obtained only based on data for soaking temperature  $T = 650$  °C in HT and present in form (2)

$$\text{at } n = 6, A = 1.73 \cdot 10^{-14} \text{ } 1/(\text{MPa}^n\cdot\text{h}).$$

Respectively the creep function in general depending on material temperature starting from 550 °C and higher can be approximated by typical dependence (4) with corresponding coefficients  $B, G, n$  from the Table 1.

Obtained results of modeling of residual stress relaxation in a zone of circumferential welded joint of RCP Du850 after HT and complete cooling to 20 °C indicate on sufficiently high level of efficiency of relaxation of residual stresses at set parameters ( $T = 650$  °C, soaking time 7 h). The level of maximum residual tensile stresses, namely circumferential component  $\sigma_{\beta\beta}$  and axial  $\sigma_{zz}$  one does not exceed 30–40 MPa, compression stresses on inner surface are somewhat higher from — 70 to — 80 MPa.

Comparison of accuracy of modeling of the process of stress relaxation using simplified creep function based on Norton–Bailey law for fixed soaking temperature and more general creep function are given on Figure 8. The comparison was carried out for efficiency of relaxation of residual circumferential stresses  $\sigma_{\beta\beta}$  in a zone of butt welded joint of RCP Du850 in HT depending on selection of creep

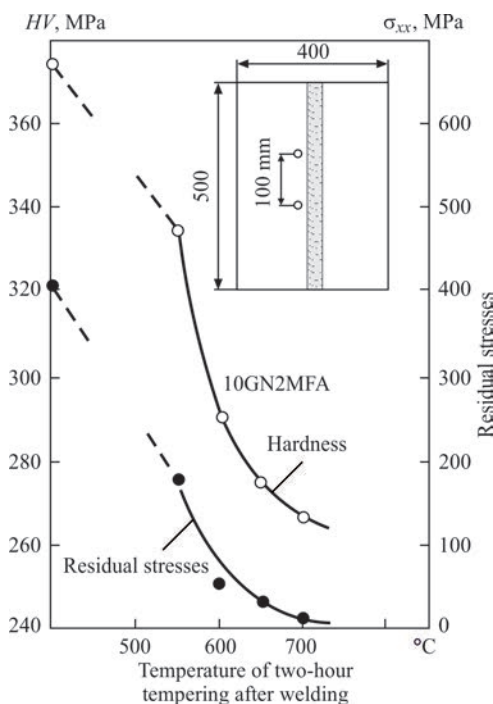


**Figure 7.** Effect of temperature of two-hour tempering after welding on level of residual stresses and hardness in zone of welded joint of steel 10GN2MFA [16]

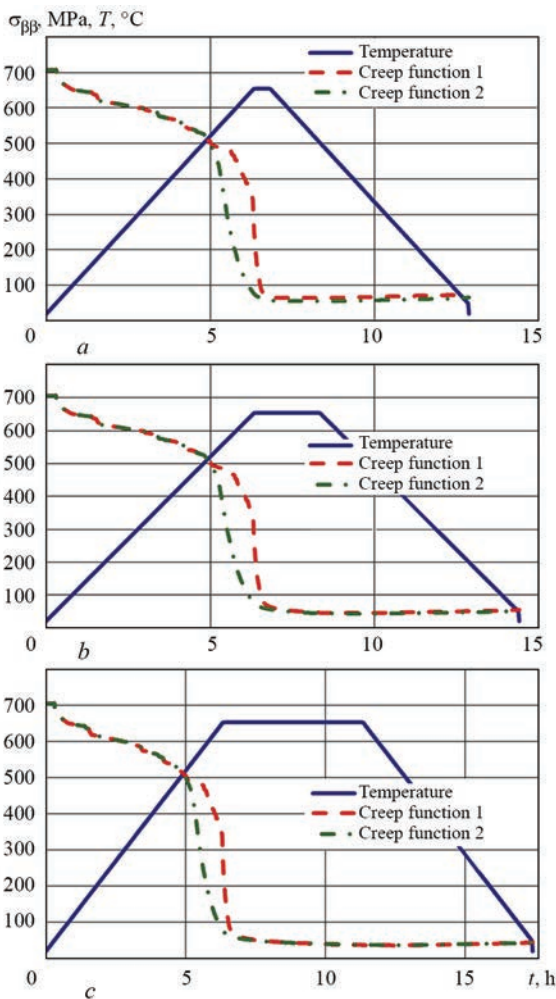


**Figure 8.** Dependence of efficiency of relaxation of residual stresses  $\sigma_{\beta\beta}$  (circumferential component) in zone of butt welded joint of RCP Du850 in HT on selection of creep function and time of soaking ( $T = 650\text{ }^{\circ}\text{C}$ ): *a* — 0.5; *b* — 2 and *c* — 5 h

function and time of soaking at  $T = 650\text{ }^{\circ}\text{C}$  (0.5; 2 and 5 h), heating and cooling rate 100 deg/h. It can be noted that depending on creep function there is a change of stress relaxation kinetics, namely at more general creep function the processes of relaxation due to creep start earlier at  $T = 550\text{ }^{\circ}\text{C}$  temperature, but at soaking the creep curves approach and almost match. The maximum residual stresses  $\sigma_{\beta\beta}$  decrease from 710 to 50 MPa in a welded joint zone. Only in the case of very short soaking (0.5 h) stress relaxation by simplified model does not have time to take place and difference in values of residual stresses after HT becomes noticeable — 50 and 65 MPa. Thus, the simplified creep function in the cases of very short soaking can give significant error in the results of modeling of relaxation of residual stresses relatively to the more general creep function which considers dependence of the creep process on temperature of heating and cooling stage. In the considered case the relative error made approximately 30 %.

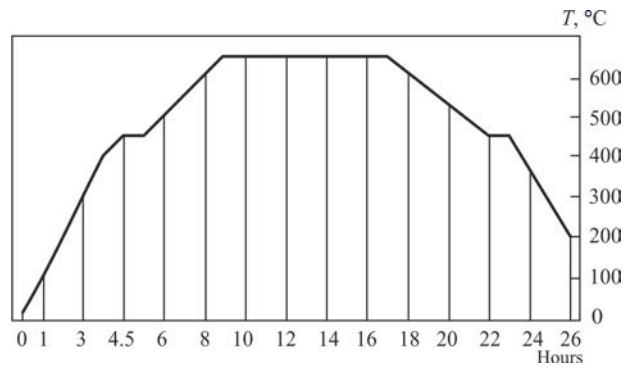


**Figure 9.** Diagram of HT by high-temperature tempering mode

**EXAMPLE No. 3. LOCAL HT OF WELDED JOINT No. 111 OF COLLECTOR TO NOZZLE Du1200 OF PGV-1000 STEAM GENERATOR**

Nozzle Du1200 of steam generator and collector is made from pearlite class steel 10GN2MFA. A weld is carried out manually or automatically, weld root is made manually using argon-arc welding with filler wire Sv08G2S, height of root pass is 6–8 mm. Filling of the main part of weld is carried manually using TsU or UONI-13/55 electrodes of 4 or 5 mm diameter and Sv08GSMT and Sv10GN1MA wires of 2 mm diameter and FTs-16 or AN-17 fluxes are used for automatic welding. Operations of intermediate and final high-temperature tempering (Figure 9) are carried out by circular heaters (Figure 10) for the purpose of relaxation of residual stresses related with assembly welding or local repair of separate defects by a scheme of multilayer filling of corresponding grooving of welded joint No. 111.

Additional heat sources that provide local HT of the welded assembly can be set by corresponding heat flow through heating surface or change of surface temperature in a heating zone, if the latter is performed by a set program as indicated for high-temperature tempering mode.

There was carried out a mathematical modeling of a problem of nonstationary heat conductivity and thermoplastic deformation in welding heating during

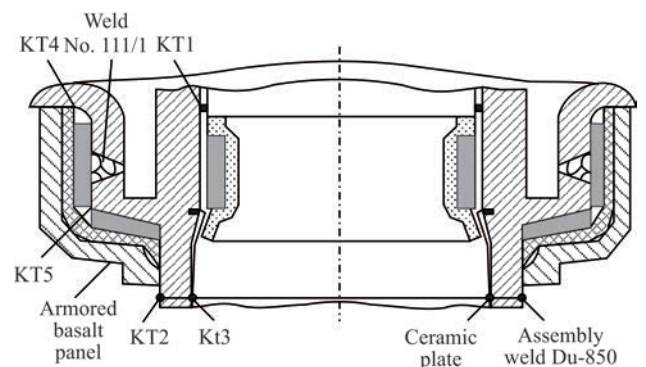


**Figure 10.** Scheme of installation of heaters and heat-insulating materials in sections of welded joint No. 111 in postweld HT (CP1 = CP5 — control points)

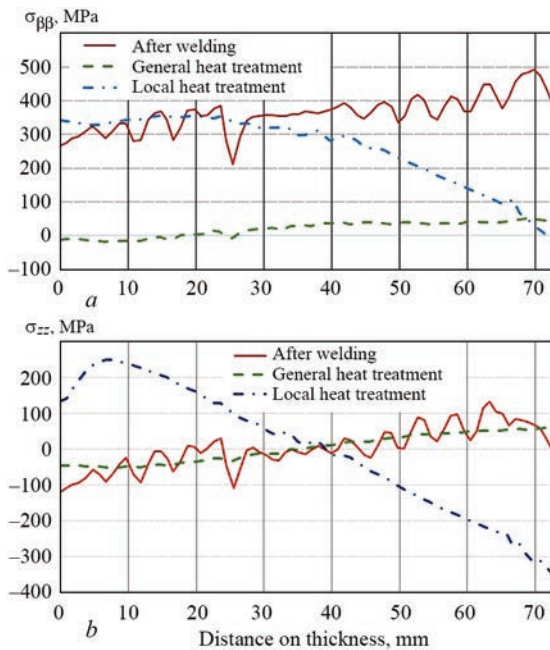


**Figure 11.** Distribution of residual welding stresses of axial  $\sigma_{zz}$  (a) and circumferential  $\sigma_{\beta\beta}$  (b) on thickness of welded joint No. 111 after welding and after general and local HT

performance of all ( up to 100) passes of groove filling of welded joint No. 111 and further complete cooling. As a result there were obtained the distributions of components of residual stresses which are rather non-uniform on welded joint thickness. Tensile circumferential stresses  $\sigma_{\beta\beta}$  (to 650 MPa) have the highest level. Axial residual stresses  $\sigma_{zz}$  are compression ones (to — 170 MPa) on inner surface of the joint and tensile ones on outer (to 350 MPa). Radial component  $\sigma_{rr}$  has tensile stresses to 200 MPa.

From point of view of failure resistance of welded joint No. 111 by stress-corrosion cracking mechanism the distributions of circumferential and axial residual

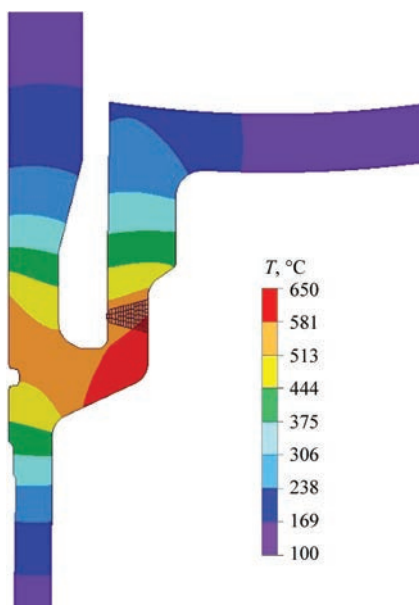


**Figure 12.** Distribution of temperature in process of soaking in local postweld HT

stresses on the joint inner surface are particularly important. After assembly welding rather high circumferential residual tensile stresses (to 300 MPa) and axial compression stresses were determined in the indicated zone. Taking into account geometry complexity of the assembly of welded joint No. 111, technological operation of local postweld HT can not only decrease the level, but also promote formation of new residual stresses.

During performance of this investigation, similar to previous examples, there were used two approaches for modeling of temperature distributions during postweld HT. Thus, the first simplified approach corresponds to the conditions of general furnace HT, when whole welded joint is forcedly uniformly heated according to set HT mode. The second approach corresponds to the real conditions of heat treatment, i.e. in a zone of heater installation (Figure 10) the surface temperature changes in time  $t$  (beginning from start of heater operation) by diagram of HT mode (Figure 9). The rest of assembly surface has an insulation or heat exchange with environment by Newton–Richmann law.

Performance of general HT of welded joint No. 111, modeling of which is provided by uniform heating (approach 1) of the assembly to soaking temperature 650 °C results at soaking time 8 h to significant relaxation of residual stresses, namely the level of all components of residual stresses reduced from 100 MPa and lower (Figure 11).

In modeling of relaxation and redistribution of residual stresses in welded joint No. 111 the obtained results are different in essence when performing local HT by means of application of heat flows from the heater from assembly surface (approach 2). First of all, heating using locally located heaters does not provide uniformity of distribution of temperature in the zone of welded joint in the process of soaking due to complex assembly geometry (Figure 12). As a result, significant nonuniform heating promotes formation of new residual stresses, distribution and level of which dramatically differ from residual stresses after welding (Figure 11).

After local HT the circumferential welding residual stresses  $\sigma_{\beta\beta}$  on the inner joint surface virtually do not change and reach the level of 350 MPa and sufficiently high after welding circumferential residual tensile stresses at 400 MPa level reduce to 0–100 MPa (Figure 11, a) on the outer surface. Axial residual stresses  $\sigma_{zz}$  on inner surface which after welding were the compression stresses at — 100 MPa level become the tensile stresses and reach the level of 200–300 MPa after local HT and on outer surface have compression values to — 300 MPa (Figure 11, b).

Thus, the local high-temperature tempering with nonuniform distribution of temperature in a zone of welded joint under conditions of sufficiently rigid assembly of welded joint No. 111 results in some decrease of circumferential residual stresses on the weld outer surface, however a new zone of high axial tensile stresses is formed on the inner joint surface.

Provided results as for investigation of efficiency of technology of local HT of welded joint No. 111 showed that improper selection of a place for heater positioning in local HT can result in negative consequences, namely formation of the new residual tensile stresses in the dangerous zones of welded assembly. Low efficiency of considered technology of postweld HT and probably even its negative effect on integrity of welded joint No. 111 indicate the necessity of optimization of technology of local HT including, in particular, mathematical modeling methods.

## CONCLUSIONS

1. In case of general furnace HT of welded structure the heat processes can be modeled based on application of two different approaches. The first, more economical by realization approach assumes that in heating, soaking and cooling the material temperature is set forcedly uniform by welded assembly volume according to given mode of heat treatment. The second one more accurate approach considers the possible nonuniformity of structure temperature distribution as a result of heating and cooling from surface due to convection with ambient air in the furnace.

2. Comparison of the results of modeling of relaxation of residual welding stresses in HT in case of forced uniform heating with the results of HT modeling due to convection showed that in case of long enough soaking in HT, when the welded joint has time for complete heating on thickness, the first approach provides the results on relaxation of residual stresses very close to the second one, which considers the level of heating on thickness and delay of heating to soaking temperature. In case of short soaking time the first approach can give significant error.

3. Modeling of process of HT of welded joints is often based on a simplified function of material creep by Norton–Bailey law as power dependence between stress intensity and creep strain rate at fixed soaking temperature. More general mathematical models of creep, for example, Arrhenius model, can take into account accumulation of creep strain in a wide range of material temperatures and allow tracing the deformation processes not only at soaking temperature, but at lower temperatures of material and can be effective in modeling of the processes of relaxation of residual stresses in local HT of welded structures or in the case

of the general furnace heat treatment at short soaking time, when uniform heating to set soaking temperature is not provided by volume of welded structure or assembly.

4. Comparison of the results on efficiency of relaxation of residual stresses showed that the calculation kinetics of stress relaxation changes depending on creep function. Thus, in the case of more general creep function the relaxation processes start earlier due to creep in heating, however in process of soaking the creep curves by simplified and general models approach and almost match. In case of very short soaking the simplified creep function can provide significant error in the results of modeling of residual stresses relaxation in relation to more general creep function which considers dependence of creep process on temperature on heating and cooling stages. In the considered case of HT of RCP butt welded joint Du850 the relative error made 30 %.

5. Study of efficiency of a technology of local HT of the welded joints showed that complex assembly geometry and improper selection of heaters location can result in negative consequences, namely formation of the new residual tensile stresses in the dangerous zones of welded assembly. It is related with significant inhomogeneity of temperature distribution at local heating of the assembly. It is relevant to carry out optimization of the new technologies of local HT involving mathematical modeling methods in order to increase efficiency of a technology of postweld local HT and elimination of its possible negative effect on integrity of welded joints.

## REFERENCES

1. Korolkov, P.M. (2006) Heat treatment of welded joints. Kyiv, Ekotekhnologiya [in Russian].
2. (2007) *ASME Boiler & Pressure Vessel Code VIII Div 2e an International Code*. New York, The American Society of Mechanical Engineers.
3. Makhnenko, V.I. (2006) *Safe service life of welded joints and assemblies of modern structures*. Kyiv, Naukova Dumka [in Russian].
4. (2013) *Guide to methods of assessing the acceptability of flaws in metallic structures*. The British Standards Institution. BS7910:2013.
5. Makhnenko, O.V., Kansala, S.M., Basystyuk, N.R., Cherkashyn, M.V. (2021) Mathematical modeling of residual stresses in WWER-1000 elements after heat treatment. *The Paton Welding J.*, **3**, 10–16. DOI: <https://doi.org/10.37434/as2021.03.02>
6. Stepanov, G.V., Kharchenko, V.V., Babutsky, A.I. et al. (2006) Stress-strain state of unit of collector welding-up to branch pipe of steam generator vessel during local heat treatment. *Problemy Prochnosti*, **6**, 43–50 [in Russian].
7. Makarenko, A.A., Makhnenko, O.V. (2022) Mathematical modeling of residual stresses in composite welded joints of WWER-1000 reactor vessel cover with CSS nozzles. *The Paton Welding J.*, **1**, 33–40. DOI: <https://doi.org/10.37434/as2022.01.05>

8. Makhnenko, O.V., Kostenevych, O.S. (2020) Impact of technological parameters of arc deposition of an anticorrosion layer in the vessel of WWER-1000 reactor on residual stress distribution. *The Paton Welding J.*, **12**, 2–14. DOI: <https://doi.org/10.37434/as2020.12.01>
9. Rabotnov, Yu.N. (1966) *Creep of structure elements*. Moscow, GIFML [in Russian].
10. Iliyushin, A.A. (2004) *Transactions (1946–1966)*. Vol. 2: Ductility. Moscow, Fizmatlit [in Russian].
11. Katanakha, N.A., Semenov, A.S., Getsov, L.V. (2013) Unified model of long-term and short-time creep and identification of its parameters. *Problemy Prochnosti*, **4**, 143–157 [in Russian].
12. Betten, J. (2008) *Creep mechanics*. Berlin, Heidelberg, New York, Springer. DOI: <https://doi.org/10.1007/978-3-540-85051-9>
13. Naumenko, K., Altenbach, H. (2007) *Modeling of creep for structural analysis*. Berlin, Heidelberg, New York, Springer. <https://www.springer.com/gb/book/9783540708346>
14. Makhnenko, O.V., Mirzov, I.V., Porokhonko, V.B. (2016) Modeling of residual stresses, radiation swelling and stressed state of in-service WWER-1000 reactor baffle. *The Paton Welding J.*, **4**, 32–38. DOI: [doi.org/10.15407/tpwj2016.04.03](https://doi.org/10.15407/tpwj2016.04.03)
15. Margolin, B.Z., Gulenko, A.G., Kursevich, I.P., Buchatskii, A.A. (2006) Modeling for fracture in materials under long-term static creep loading and neutron irradiation. Pt 2: Prediction of creep rupture strength for austenitic materials. *Strength of Materials*, **38(5)**, 449–457.
16. Hrivnak, I. (1984) *Weldability of steels*. Moscow, Mashinostroenie [in Russian].

**ORCID**

O.V. Makhnenko: 0000-0002-8583-0163,  
 O.S. Milenin: 0000-0002-9465-7710,  
 O.F. Muzhychenko: 0000-0002-4870-3659,  
 S.M. Kandala: 0000-0002-2036-0498,  
 O.M. Savytska: 0000-0002-9363-6184,  
 G.Yu. Saprykina: 0000-0003-1534-7253

**CONFLICT OF INTEREST**

The Authors declare no conflict of interest

**CORRESPONDING AUTHOR**

O.V. Makhnenko  
 E.O. Paton Electric Welding Institute of the NASU  
 11 Kazymyr Malevych Str., 03150, Kyiv, Ukraine.  
 E-mail: [makhnenko@paton.kiev.ua](mailto:makhnenko@paton.kiev.ua)

**SUGGESTED CITATION**

O.V. Makhnenko, O.S. Milenin,  
 O.F. Muzhychenko, S.M. Kandala, O.M. Savytska,  
 G.Yu. Saprykina (2023) Mathematical modeling  
 of residual stress relaxation during performance  
 of postweld heat treatment. *The Paton Welding J.*, **6**,  
 32–40.

**JOURNAL HOME PAGE**

<https://patonpublishinghouse.com/eng/journals/tpwj>

Received: 10.05.2023

Accepted: 17.07.2023

## SUBSCRIPTION-2023



«The Paton Welding Journal» is Published Monthly Since 2000 in English, ISSN 0957-798X, [doi.org/10.37434/tpwj](https://doi.org/10.37434/tpwj).

«The Paton Welding Journal» can be also subscribed worldwide from catalogues subscription agency EBSCO.

If You are interested in making subscription directly via Editorial Board, fill, please, the coupon and send application by Fax or E-mail.

12 issues per year, back issues available.

\$384, subscriptions for the printed (hard copy) version, air postage and packaging included.

\$312, subscriptions for the electronic version (sending issues of Journal in pdf format or providing access to IP addresses).

Institutions with current subscriptions on printed version can purchase online access to the electronic versions of any back issues that they have not subscribed to. Issues of the Journal (more than two years old) are available at a substantially reduced price.

The archives for 2009–2021 are free of charge on [www://patonpublishinghouse.com/eng/journals/tpwj](http://www://patonpublishinghouse.com/eng/journals/tpwj)

**Address**

11 Kazymyr Malevych Str., 03150, Kyiv, Ukraine  
 Tel./Fax: (38044) 205 23 90  
 E-mail: [journal@paton.kiev.ua](mailto:journal@paton.kiev.ua)  
[www://patonpublishinghouse.com/eng/journals/tpwj](http://www://patonpublishinghouse.com/eng/journals/tpwj)

DOI: <https://doi.org/10.37434/tpwj2023.06.06>

## ELECTRON BEAM MELTING OF TITANIUM ALLOYS FOR MEDICAL PURPOSES

V.O. Berezos, D.S. Akhonin

E.O. Paton Electric Welding Institute of the NASU

11 Kazymyr Malevych Str., 03150, Kyiv, Ukraine

### ABSTRACT

The established regularities of the processes of alloying element evaporation and crystallization at electron beam melting were the base for determination of the melting modes and optimization of the technology of producing defect-free and chemically homogeneous ingots of a promising Ti-6Al-7Nb titanium alloy for medical purposes, having a homogeneous fine-grained structure without any traces of zonal segregation. Microstructural studies showed that Ti-6Al-7Nb alloy is a two-phase  $\alpha+\beta$  titanium alloy of martensitic type, in which 1–2 mm thick precipitates of  $\alpha$ -phase are observed on the boundaries of primary  $\beta$ -grains, and in the grain body formation of a platelike (widmanstaetten) morphology of  $\alpha$ - and  $\beta$ -phase precipitates is found, the length of which inside the grains is equal to 10–40  $\mu\text{m}$ . Such a structure ensures the best combination of the alloy mechanical characteristics, namely high values of strength (905 MPa) and ductility (13.5 %), which meet the requirements of international standards for titanium alloys for medical purposes.

**KEYWORDS:** titanium alloys, electron beam melting, medicine, evaporation, chemical composition, structure, mechanical properties

### INTRODUCTION

Functional reliability of medical implants and structures, applied in orthopedics, traumatology, stomatology and other medical fields, primarily depends on a set of service properties, which are exhibited by the material under the real conditions of its service in a living body and the impact of this material on the surrounding tissues, biological liquids and the body as a whole [1–4]. At present, the main materials, used in implant manufacture, are metal alloys (titanium and cobalt), stainless steels, polymers and ceramics [5]. Despite intensive application of polymers and ceramic materials in implant products, metallic materials preserve their leading role (Figure 1). The best of the modern metallic biomaterials is titanium and alloys on its base.

Modern medicine uses a wide range of titanium alloys, varying by their chemical composition and mechanical parameters. Al, V, Mo, Mg, Cr, Si, Sn are the most often used of them as alloying elements.

However, vanadium poses a certain danger in titanium alloys. In the main Ti-6Al-4V medical alloy the content of toxic vanadium is just 4 % by weight, while in stainless steels the mass concentration of toxic nickel and chromium (in total) is more than 30 %.

Today traditional Ti-6Al-4V is replaced by new medical alloys, such as Ti-6Al-7Nb, Ti-13Nb-13Zr and Ti-12Mo-6Zr, not containing vanadium, which has, even though an insignificant, but toxic influence on live tissues.

Ti-6Al-7Nb alloy (international designation UNS R56700) is a special high-strength titanium alloy with excellent biocompatibility for surgical implants [6], developed for application for medical and surgical purposes.

Alloying is one of the efficient methods to improve the mechanical properties, and since niobium belongs to the same group as vanadium does, it usually acts as an  $\alpha$ - $\beta$  stabilizing element (similar to Ti-6Al-4V alloy). Although its properties are almost identical to those of Ti-6Al-4V, vanadium was replaced by niobium as a  $\beta$ -stabilizer, which increases the biocompatibility [7–9]. Ti-6Al-7Nb is one of the titanium alloys, which consists of hexagonal  $\alpha$ -phase (aluminium-sta-

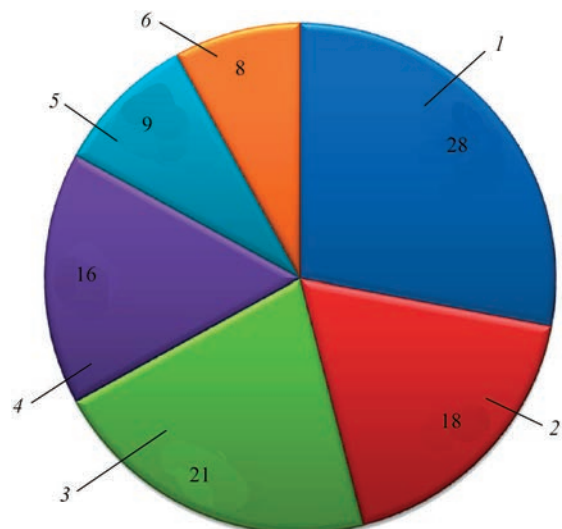


**Figure 1.** Main materials used for implant manufacture, %: 1 — titanium alloys; 2 — medical steels; 3 — cobalt alloys; 4 — polymers; 5 — ceramics, 6 — other materials

**Table 1.** Mechanical characteristics of titanium alloys

Alloy	$\sigma_{0.2}$ , MPa	$\sigma_y$ , MPa	$\sigma^{-1}$ , MPa	$E$ , MPa	$\delta$ , %	$\psi$ , %
BT1-0	320	400	170	$11.1 \cdot 10^4$	25	–
Ti–6Al–4V	795	860	400	$11.5 \cdot 10^4$	10	25
Ti–6Al–7Nb	793	862	–	–	–»–	–»–
Bone	250	–	200	$2.5 \cdot 10^4$	0.5	–

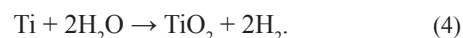
bilized) and regular bulk-centered  $\beta$ -phase (niobium-stabilized). The alloy is characterized by additional advantages as to mechanical properties, has higher corrosion resistance and bioresistance, compared to Ti–6Al–4V alloy [10, 11].

Mechanical characteristics of Ti–6Al–7Nb alloy are given in Table 1, in comparison with those of other titanium alloys.

Ti–6Al–7Nb alloy is traditionally twice or three times remelted under vacuum to obtain a highly homogeneous composition of the ingot. The ingot is subjected to hot pressing or treatment of the round or flat rods by the traditional methods of titanium alloy treatment. Over the recent years, research work has been performed to produce medical products from Ti–6Al–7Nb titanium alloy, using different 3D printing technologies, such as SLM and EBM [12, 13].

The biocompatibility of Ti–6Al–7Nb alloy is high, and it can be applied in manufacture of implant-devices: artificial hip and knee joints, bone plates, screws for fracture fixation, heart valve prosthesis, pacemakers and artificial hearts [5, 10, 11].

As noted above, the determinant characteristic of materials for medical purposes is their biological compatibility with the human body, alongside the required physical-mechanical characteristics. This necessitates the use of technological processes, ensuring a higher degree of refining from impurities (sulphur, arsenic, phosphorus, lead, tin, copper, etc.) and gases in manufacture of such materials and products from them. Therefore, for a wide introduction of titanium alloys in medicine, it is necessary not only to develop new titanium-based materials with higher service properties, but further on to improve production of the existing titanium semi-finished products. Any imperfections of chemical and structural homogeneity in titanium alloys lead to lowering of the strength and fatigue life of the products. Producing titanium alloys involves difficulties, caused by the high sensitivity of titanium to interstitial impurities, particularly, to oxygen, nitrogen, hydrogen, and carbon, and by interaction with many chemical elements, resulting in formation of solid solutions or chemical compounds. For instance, oxygen, nitrogen and hydrogen can react with titanium to form different chemical compounds, as a result of the following reactions:



High activity of titanium leads to running of physical-chemical processes of interaction with gases even in the solid state. Therefore, the intermetallic inclusions (hydrides, nitrides, oxides) may form both during the ingot production, and at different stages of technological processing to manufacture finished products.

More over, one of the main structural imperfections of the titanium alloys is the presence of non-metallic inclusions [14]. Nonmetallic inclusions can penetrate into the finished product from the charge materials during melting, and can be formed at heat treatment of the finished product. Titanium actively interacts not only with gases, but also with other elements, including alloying components of the alloys, so that local enrichment of individual volumes of the ingots by alloying elements can lead to formation of intermetallic inclusions, for instance,  $\text{Ti}_3\text{Al}$ ,  $\text{TiAl}$ , etc.

At present not all the methods of manufacturing titanium ingots allow producing sound metal, and at violation of the technological process of titanium ingot production defects are found in the ingots, lowering the metal quality. Thus, solving the problem of producing sound ingots of high-strength titanium alloys from different charge materials is rather urgent.

Nowadays the most efficient refining of the metals and alloys is realized when conducting the processes of their vacuum melting. Electron beam melting (EBM) is the most efficient vacuum metallurgy process to produce the alloys, including the refractory and highly reactive ones with super low content of gases, low-melting impurities and nonmetallic inclusions. EBM enables regulation of the ingot melting rate in a wide range, due to an independent heating source that, in its turn, allows controlling the duration of the metal staying in the liquid overheated state. EBM is a technology, allowing practically completely ensuring removal of high-melting inclusions of high and low density [14]. Thus, EBM allows a significant improvement of the quality of titanium alloy ingots [14, 15].

A peculiarity of the work on producing materials and products for medical purposes is the fact that application of electron beam technologies allows, alongside metal refining, also obtaining the required physical-mechanical properties.

The majority of the titanium alloys, however, have a high content of alloying elements that complicates their production by EBM. Therefore, when producing titanium ingots for medical purposes there is the problem of ensuring the specified chemical composition of the ingot, as melting in relatively deep vacuum promotes selective evaporation of alloying elements with a high vapour pressure [16, 17]. This problem primarily concerns aluminium, as it has one of the highest values of vapour pressure, and this element is present in practically all the titanium alloys [14, 18]. Concentration of elements in an ingot with vapour pressure below that of titanium vapour, niobium in this case, can be even somewhat increased.

### CALCULATION OF TECHNOLOGICAL MODES OF MELTING

In order to analyze the influence of EBM technological parameters and chemical composition of the initial charge on chemical composition of the produced ingots, the mathematical model of the processes of alloy component evaporation during EBM [17] was used to determine the dependencies of the alloying element content in 110 mm ingot of Ti-6Al-7Nb titanium alloy on the melting rate at different chemical composition of the initial charge  $[Al]_0$ ,  $[Nb]_0$ .

Analysis of the obtained calculation results shows that losses of alloying elements for evaporation depend on their physical-chemical properties. While aluminium content during melting decreases (Figure 2), niobium content increases, on the contrary (Figure 3), compared to the content of these elements in the initial charge.

Such behaviour of alloying elements during melting is explained by the fact that aluminium vapour pressure at the specified temperature is higher than that of titanium vapour, while niobium vapour pressure is lower than that of titanium vapour. Consequently, in keeping with Langmuir law [19, 20], titanium evaporation rate is lower than that of aluminium evaporation and higher than that of niobium evaporation. Therefore, aluminium concentration in EBM ingot decreases, accordingly, compared to its concentration in the initial charge, and niobium concentration becomes higher.

Studying the behaviour of such alloying element as aluminium is critical for optimization of the process of EBM of Ti-6Al-7Nb titanium alloy. This is due to aluminium losses in EBM and considerable in-

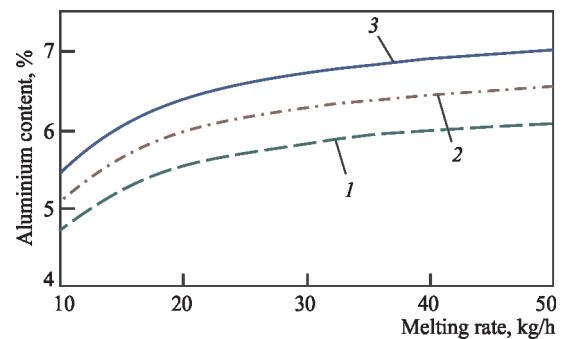


Figure 2. Dependencies of aluminium content in the ingot of Ti-6Al-7Nb alloy on melting rate at different content of aluminium  $[Al]_0$  in the initial charge, %: 1 — 6.5; 2 — 7.0; 3 — 7.5

fluence of aluminium on titanium alloy structure and mechanical properties.

Dependence of aluminium content in EBM ingot on melting rate is nonlinear. At a fixed composition of the initial charge at low melting rates (up to 30 kg/h) aluminium losses for evaporation are quite significant, and they strongly depend on the melting rate. So, for instance, at 7% content of aluminium in the initial charge, lowering of melting rate from 30 to 10 kg/h leads to increase of aluminium losses for evaporation from 0.72 to 1.92%, i.e. 2.7 times. At melting rates above 30 kg/h aluminium losses for evaporation are much smaller, and their dependence on the melting rate is rather weak. At increase of the melting rate from 30 to 50 kg/h aluminium losses for evaporation decrease from 0.72 to 0.45%, i.e. 1.6 times.

It should be noted that aluminium losses for evaporation strongly depend on the melting rate, i.e. the time of titanium staying in the liquid state, when aluminium intensively evaporates from the melt (Figure 4).

Despite the relatively weak dependence of aluminium losses for evaporation on aluminium concentration in the initial charge (Figure 4), a detailed analysis of the dependence of these losses on aluminium content in the initial charge showed (Figure 5) that the higher the aluminium content in the initial charge, the greater are the aluminium losses for evaporation.

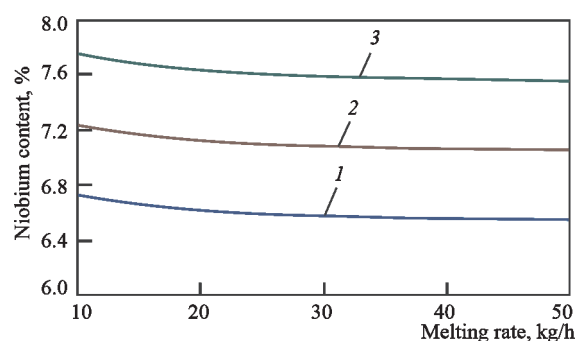
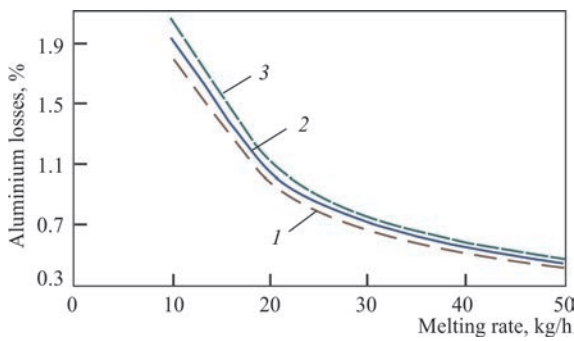


Figure 3. Dependencies of niobium content in an ingot of Ti-6Al-7Nb alloy on melting rate at different content of niobium  $[Nb]_0$  in the initial charge, %: 1 — 6.5; 2 — 7.0; 3 — 7.5



**Figure 4.** Aluminium losses for evaporation, depending on melting rate at different concentration of aluminium  $[Al]_0$  in the initial charge, %: 1 — 6.5; 2 — 7.0; 3 — 7.5

Analysis of aluminium losses for evaporation at each EBM stage (Figure 6) showed that, depending on the melting rate, at the end of the consumed billet, the relative losses of aluminium for evaporation are equal to approximately 25 % of the total losses of aluminium during EBM, the relative losses of aluminium for evaporation in the cold hearth are equal to 51 % of the total aluminium losses, and in the crucible they are close to 24 %. Such a distribution of aluminium losses between the melting stages weakly depends on the melting rate, and is due, primarily, to the area of the melt free surface at each melting stage, from which aluminium evaporates. This fact should be taken into account when designing the technological fixtures for producing ingots by EBM.

Conducted analysis of the process of aluminium evaporation during EBM shows that the main factors influencing aluminium concentration in EBM ingot are its content in the initial charge and the melting rate.

Results of calculations conducted by the mathematical model revealed that niobium concentration in Ti-6Al-7Nb alloy practically does not change in EBM ingot at the melting rate higher than 40 kg/h (see Figure 3). It should be noted that at melting rates of up to 30 kg/h niobium content in the ingot rises by 0.09–0.24 %, compared to its concentration in the initial charge that is associated with relatively high loss-

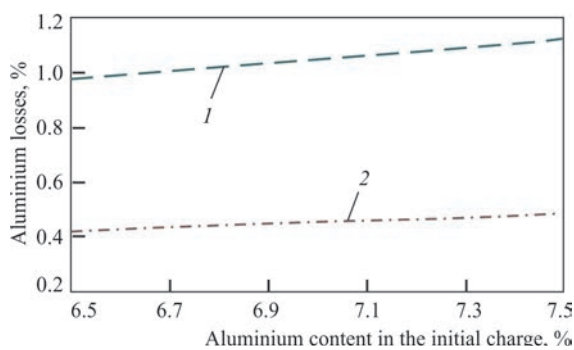


**Figure 5.** Aluminium losses for evaporation, depending on aluminium content in the initial charge at the following melting rate: 1 — 20; 2 — 50

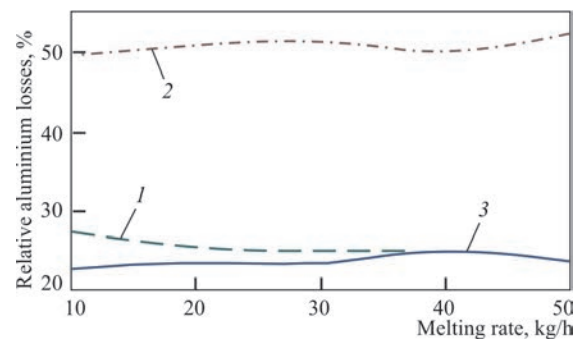


**Figure 6.** Relative losses of aluminium for evaporation at the consumable electrode end face (1), in the cold-hearth (2) and in the mould (3), depending on melting rate

es of aluminium for evaporation at these melting rates (see Figure 4).

Thus, results of the conducted investigations lead to the conclusion that to ensure the specified chemical composition of 110 mm ingot of Ti-6Al-7Nb titanium alloy for medical purposes the melting should be performed at the rate of 40–50 kg/h, and aluminium should be added to the initial charge in the quantity 0.5 % higher than the targeted aluminium concentration in the ingot.

In order to improve the technology of manufacturing ingots from titanium alloys for medical purposes, PWI performed work on producing ingots of an alloy of Ti-Al-Nb system. Ingots of 110 mm diameter were produced by the technology of cold-hearth EBM with portioned feed of liquid metal into a water-cooled mould.

## EXPERIMENTAL PART OF THE INVESTIGATIONS

Investigations of the processes of alloy component evaporation from the melt in vacuum were the base for calculations of the predicted chemical composition of the produced ingots, the results of which were used to adjust the charge billet components. Alloying components with high vapour pressure (Al) were blended taking into account the compensation of evaporation losses.

The charge billet was a slab reproduced from titanium sponge TG-100 with alloying components in the form of pure niobium and primary aluminium (Figure 7).

UE-208M electron beam unit was used to conduct experimental melts to produce 110 mm ingots of Ti-6Al-7Nb titanium alloy.

During melting the following technological parameters were monitored: accelerating voltage of electron beam guns, beam current, speed of feeding the initial charge into the melting zone, speed of ingot pulling out of the mould, and cooling water temperature.



**Figure 7.** Charge billet (a) and electron beam melting (b) of 110 mm ingot of Ti-6Al-7Nb titanium alloy

**Table 2.** Distribution of alloying elements and impurities along EBM ingot of Ti-6Al-7Nb titanium alloy, wt.%

Ingot part	Al	Nb	Ta	Fe	C	H	O	N
Upper	6.2	6.8	0.01	0.09	0.01	0.005	0.11	0.012
Middle	6.3	6.7	→→	0.10	→→	–	–	–
Lower	6.2	→→	→→	0.08	→→	–	–	–
UNS R56700	5.6–6.6	6.5–7.5	<0.5	<0.25	<0.03	<0.05	<0.20	<0.05

Numerical values of the technological parameters of melting used to produce 110 mm ingots of Ti-6Al-7Nb titanium alloy are as follows:

Melting rate, kg/h	40–50
Height of portions simultaneously poured into the mould, mm	10
Power in the mould, kW	16
Power in the cold hearth, kW	80

At the end of melting, shrinkage cavity removal was performed by gradual lowering of the power of heating the ingot upper end face in the mould.

The side surface of the produced ingots after cooling in vacuum to the temperature below 300 °C is clean, and there is no higher concentration of impurity elements in the form of oxidized or alpha layer (Figure 8). The depth of surface defects of corrugation type is 1–3 mm, defects in the form of tears, cracks or lacks of fusion are absent.

To assess the quality of metal of the produced ingots, chemical composition of the samples cut out along the sample from the upper, middle and lower parts was investigated. Results of analysis of chemical composition of the produced ingot metal showed that alloying element distribution along the ingot



**Figure 8.** Ti-6Al-7Nb titanium alloy ingot of 110 mm diameter

length is homogeneous, and corresponds to the grade composition (Table 2).

Considering the small dimensions of 110 mm ingot of Ti-6Al-7Nb titanium alloy, it was subjected to surface machining in a lathe. The surface layer was removed to the depth of not more than 3 mm to the side, and its end faces were machined (Figure 9).

Ingot macrostructure was studied on transverse templates, cut out from the ingot middle. The structure was revealed by etching the templates in 15 % solution of fluoric acid with addition of 3 % nitric acid at room temperature.

Ingot metal structure is dense, homogeneous, without any zones which etch differently over the ingot cross-section (Figure 10). No significant difference in the structure of the central and peripheral zones of the ingot was observed. No defects in the form of pores,



**Figure 9.** Machined ingot of Ti-6Al-7Nb titanium alloy

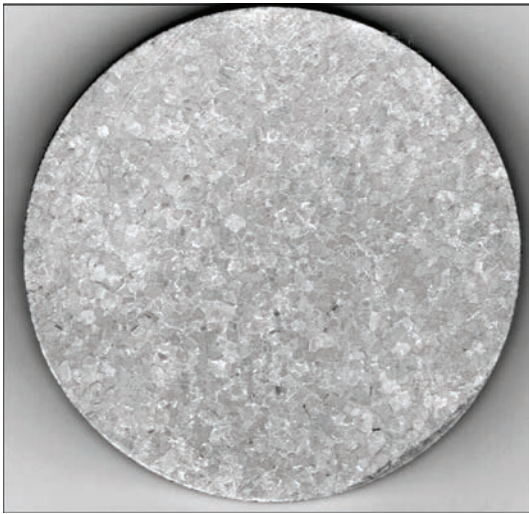


**Figure 10.** Macrostructure of cast metal of an ingot of Ti-6Al-7Nb titanium alloy

cavities, cracks, nonmetallic inclusions or alloying element segregation characteristic for VAR ingots was found.

The crystalline structure of the metal was the same along the entire ingot length, and it is characterized by crystals, the shape of which is close to the equiaxed one. Areas of columnar structure are absent.

The most important criterion of the quality of titanium alloy ingots is absence of nonmetallic inclusions in the metal, particularly in the form of nitrogen-containing alpha particles or titanium nitrides. At titanium remelting by cold-hearth EBM technology thermal and physical-chemical conditions are in place, which ensure removal of the above inclusions.

The method of ultrasonic flaw detection was used to investigate the presence or absence of internal defects in the form of nonmetallic inclusions, as well as pores or discontinuities in the titanium ingots. Investigations were conducted with application of ul-

trasonic flaw detector UD4-76 by echo-pulse method at contact variant of testing. Working frequency of analysis was equal to 1.25 MHz, which ensured the maximal signal-to-noise ratio. Multiple reflections of a small amplitude were observed when studying the ingots. This is typical for cast metal and is the result of signal reflection from the grain boundaries. Conducted analysis did not reveal any reflections, which could be interpreted as large nonmetallic inclusions, pores, or shrinkage cavities. Backwall pulse reflection was clearly visible on the scan (Figure 11). Noises are present in the area of introducing the probing signals, which are due to loose contact between the sensor and the ingot surface, which cannot be compensated by application of sealing lubricant.

Thus, conducted investigations showed that 110 mm EBM ingots of Ti-6Al-7Nb titanium alloy do not have any discontinuities, nonmetallic inclusions of more than 1 mm size, or dense clusters of finer inclusions.

The produced metal microstructure was studied in a light microscope. General view of the microstructure of Ti-6Al-7Nb titanium alloy produced by the developed EBM technology is given in Figure 12.

Metal of Ti-6Al-7Nb titanium alloy consists of equiaxed grains of 100–500  $\mu\text{m}$  size (Figure 12). A positive moment is formation of a homogeneous structure, without any manifestations of zonal segregation traces (Figure 12, *a*). This is indicative of the optimal mode of producing the ingot in electron beam melting. The grain boundaries have an  $\alpha$ -fringe, sometimes continuous, sometimes intermittent. The thickness of  $\alpha$ -fringe is 0.8–3.0  $\mu\text{m}$  (Figure 12, *d*). The intragranular structure of deep metal layers is lamellar, and it consists of  $\alpha$ -colonies of different size. The thickness of  $\alpha$ -plates is equal to 0.8–3.0  $\mu\text{m}$ . In-

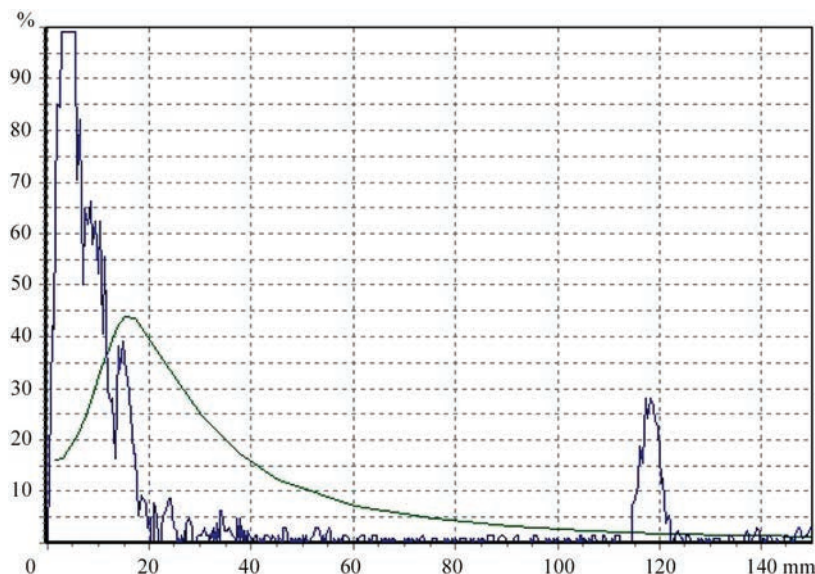


**Figure 11.** Scan of the central part of 110 mm ingot

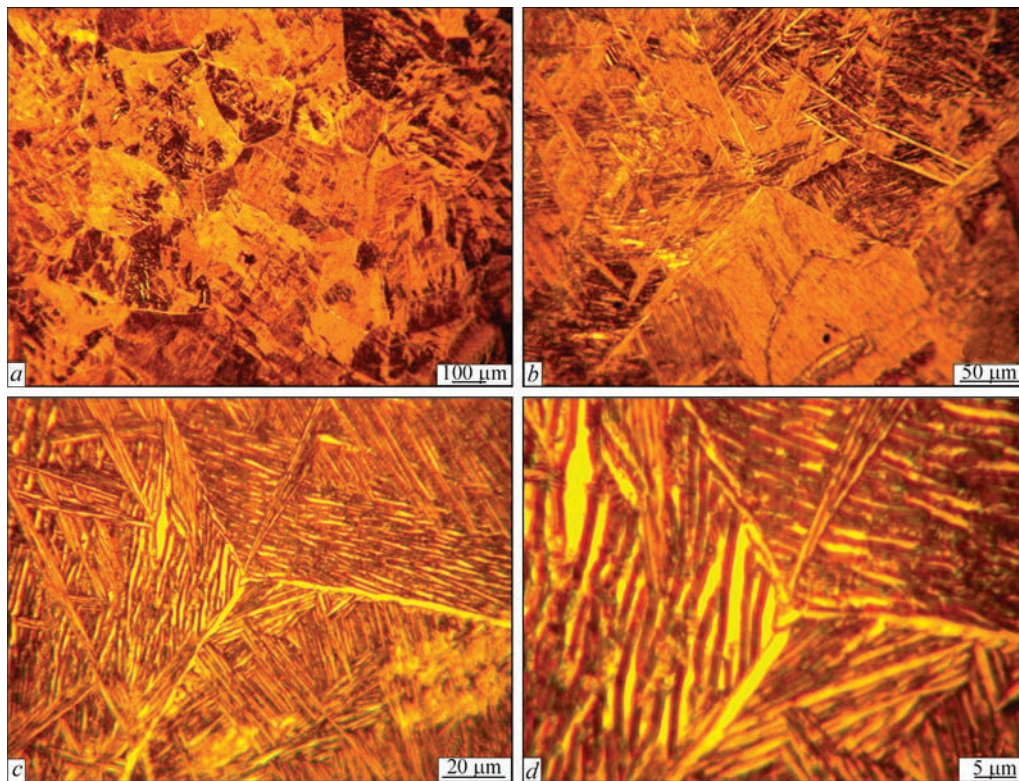


**Figure 12.** Microstructure of Ti-6Al-7Nb titanium alloy

**Table 3.** Mechanical characteristics of Ti-6Al-7Nb titanium alloy produced by EBM

Ti-6Al-7Nb	$\sigma_{0.2}$ , MPa	$\sigma_t$ , MPa	$\delta$ , %	$\psi$ , %	KCV, J/cm <sup>2</sup>
EBM	840.8	905.1	13.5	35.8	48.8
UNS R56700	793.0	862.0	>10	>25	–

terlayers of  $\beta$ -phase are located between the plates. The interlayer width is 0.3–1.0 mm.

Formation of lamellar (widmanstaetten) morphology of  $\alpha$ - and  $\beta$ -phase precipitates is observed in the grain body. The length of the phase packets inside the grains is equal to 10–40  $\mu\text{m}$  (Figure 12, *d*).

Thus, microstructural studies give grounds to consider that the alloy of the abovementioned composition is a two-phase titanium  $\alpha+\beta$ -alloy of martensitic type.

Standard samples for studying the mechanical characteristics were cut out of 110 mm ingot of Ti-6Al-7Nb titanium alloy produced by EBM (Table 3).

Obtained results were indicative of high ductility values of Ti-6Al-7Nb titanium alloy at preservation of the strength values. Such data can be explained by formation of an equiaxed fine-grained structure in EBM ingots. As one can see from the comparison table, values of mechanical characteristics of the produced samples fully meet the requirements of international standard UNS R56700, which is indicative of the high quality of the metal produced by the developed technology.

Thus, results of the performed work were used to develop an EBM technology of producing a

Ti-6Al-7Nb titanium alloy for medical purposes, the quality of which fully complies with the standard requirements as to its chemical composition, structure and mechanical properties.

## CONCLUSIONS

1. A technology of producing 110 mm ingots of Ti-6Al-7Nb titanium alloy for medical purposes by electron beam melting method was developed with process productivity of 40–50 kg/h and 16 kW power of electron beam heating in the mould.

2. The methods of mathematical modeling were used to determine the dependencies of alloying element content in 110 mm ingot of Ti-6Al-7Nb titanium alloy on the melting rate at different chemical composition of the initial charge, and it was established that the dependence of aluminium content in EBM ingot on the melting rate is nonlinear: at melting rates up to 20 kg/h aluminium losses for evaporation are higher than 1 % and they increase considerably at lowering of the melting rate, while at higher melting rates aluminium losses are equal to 0.5–0.7 %.

3. It was determined that the relative losses of aluminium for evaporation in the cold hearth are equal to

approximately 50 % of the total losses of aluminium during EBM, while at the end face of the consumable billet and in the mould they are 25 % each, which is due, primarily to the area of the melt free surface at each melting stage.

4. It is shown that the selected modes of electron beam melting ensure formation in Ti–6Al–7Nb titanium alloy of a homogeneous fine-grained structure without any manifestations of traces of zonal segregation.

5. It is also shown that the developed EBM technology is an efficient method to produce ingots of Ti–6Al–7Nb titanium alloy for medical purposes with a high-quality surface, homogeneous chemical composition and high mechanical properties.

## REFERENCES

- Kawahara, H. (1992) Cytotoxicity of implantable metals and alloys. *Bull. Jpn. Inst. Met. Mater.*, **31**, 1033–1039.
- Okazaki, Y., Ito, Y., Ito, A., Tateishi, T. (1993) Effect of alloying elements on mechanical properties of titanium alloys for medical implants. *Ibid.*, **57**, 332–337.
- Niinomi, M. (2000) Development of high biocompatible titanium alloys. *Func. Mater.*, **20**, 36–44.
- Niinomi, M. (2007) Titanium alloys for biomedical, dental and healthcare application. In: *Proc. of 11<sup>th</sup> World Conf. on Titanium (Kyoto, Japan 3–7 June 2007)*. The Japan Inst. of Metals, 1417–1424.
- Robert, B. Heimann (2020) *Materials for medical application*. De Gruyter STEM. DOI: <https://doi.org/10.1515/9783110619249>
- Fellah, Mamoun, Labaiz, Mohamed, Assala, Omar et al. (2014) Tribological behavior of Ti–6Al–4V and Ti–6Al–7Nb alloys for total hip prosthesis. *Advances in Tribology*, July, 1–13. DOI: <https://doi.org/10.1155/2014/451387>.
- Chlebus, E., Kuźnicka, B., Kurzynowski, T., Dybała, B. (2011) Microstructure and mechanical behaviour of Ti–6Al–7Nb alloy produced by selective laser melting. *Materials Characterization*, **62**(5), 488–495. DOI: <https://doi.org/10.1016/j.matchar.2011.03.006>
- Liu, Xuanyong, Chu, Paul K., Ding, Chuanxian (2004) Surface modification of titanium, titanium alloys, and related materials for biomedical applications. *Materials Sci. and Eng.: R: Reports*, **47**(3), 49–121. DOI: <https://doi.org/10.1016/j.mser.2004.11.001>
- López, M.F., Gutiérrez, A., Jiménez, J.A (2002) In vitro corrosion behaviour of titanium alloys without vanadium. *Electrochimica Acta*, **47**(9), 1359–1364. DOI: [https://doi.org/10.1016/S0013-4686\(01\)00860-X](https://doi.org/10.1016/S0013-4686(01)00860-X)
- Ajeel, Sami Abualnoun, Alzubaydi, Thair L., Swadi, Abdulsalam K. (2007) Influence of heat treatment conditions on microstructure of Ti–6Al–7Nb alloy as used surgical implant materials. *Eng. and Technology J.*, **25**(3), 431–442.
- Kobayashi, E., Wang, T.J., Doi, H. et al. (1998) Mechanical properties and corrosion resistance of Ti–6Al–7Nb alloy dental castings. *J. of Materials Sci.: Materials in Medicine*, **9**(10), 567–574. DOI: <https://doi.org/10.1023/A:1008909408948>
- Bolzoni, Leandro, Hari Babu, N., Ruiz-Navas, Elisa Maria, Gordo, Elena (2013) Comparison of microstructure and properties of Ti–6Al–7Nb alloy processed by different powder metallurgy routes. *Key Eng. Materials*, **551**, 161–179. DOI: <https://doi.org/10.4028/www.scientific.net/KEM.551.161>
- Oliveira, V., Chaves, R.R., Bertazzoli, R., Caram, R. (1998) Preparation and characterization of Ti–Al–Nb alloys for orthopedic implants. *Brazilian J. of Chemical Eng.*, **15**(4), 326–333. DOI: <https://doi.org/10.1590/S0104-66321998000400002>
- Paton, B.E., Trigub, N.P., Akhonin, S.V., Zhuk, G.V. (2006) *Electron beam melting of titanium*. Kyiv, Naukova Dumka [in Russian].
- Grechanyuk, N.I., Kulak, L.D., Kuzmenko, N.N. et al. (2017) Melting of ingots of Ti–Nb–Si–Zr system titanium alloys by the method of electron beam melting. *Suchasna Elektrometal.*, **2**, 17–20. DOI: <https://doi.org/10.15407/sem2017.02.03>
- Akhonin, S.V., Trigub, N.P., Zamkov, V.N., Semiatin, S.L. (2003) Mathematical modeling of aluminium evaporation during electron-beam cold-hearth melting of Ti6Al4V ingots. *Metallurgy and Materials Transact. B*, **34B**, 447–454.
- Akhonin, S.V., Severin, A.Yu., Berezos, V.A., Erokhin, A.G. (2013) Mathematical modelling of evaporation processes in melting of ingots of multicomponent titanium alloys in electron beam equipment with a cold hearth. *Advances in Electrometallurgy*, **4**, 288–295.
- Varich, I.Yu., Akhonin, S.V., Trigub, N.P., Kalinyuk, A.N. (1997) Evaporation of aluminium from titanium-based alloys during process of electron beam cold hearth melting. *Problemy Spets. Elektrometallurgii*, **4**, 15–21 [in Russian].
- Zhukhovitsky, A.A., Shvartsman, L.A. (1976) *Physical chemistry*. Moscow, Metallurgiya [in Russian].
- Schiller, Z., Hasing, U., Pantser, Z. (1980) *Electron beam technology*. Moscow, Energiya [in Russian].

## ORCID

V.O. Berezos: 0000-0002-5026-7366,  
D.S. Akhonin: 0009-0000-2054-4054

## CONFLICT OF INTEREST

The Authors declare no conflict of interest

## CORRESPONDING AUTHOR

V.O. Berezos  
E.O. Paton Electric Welding Institute of the NASU  
11 Kazymyr Malevych Str., 03150, Kyiv, Ukraine.  
E-mail: [titan.paton@gmail.com](mailto:titan.paton@gmail.com)

## SUGGESTED CITATION

V.O. Berezos, D.S. Akhonin (2023) Electron beam melting of titanium alloys for medical purposes. *The Paton Welding J.*, **6**, 41–48.

## JOURNAL HOME PAGE

<https://patonpublishinghouse.com/eng/journals/tpwj>

Received: 11.04.2023

Accepted: 17.07.2023

DOI: <https://doi.org/10.37434/tpwj2023.06.07>

# INFLUENCE OF HYDROGEN-METHANE GAS MIXTURES ON THE PHYSICAL AND CHEMICAL STRUCTURE OF POLYETHYLENE PIPES OF THE OPERATING GAS-DISTRIBUTION NETWORKS OF UKRAINE

M.V. Iurzenko<sup>1,2</sup>, M.O. Kovalchuk<sup>1</sup>, V.Yu. Kondratenko<sup>1</sup>, V.L. Demchenko<sup>1,2</sup>, K.G. Gusakova<sup>2</sup>, V.S. Verbovskiy<sup>3</sup>, G.V. Zhuk<sup>3</sup>, K.P. Kostogryz<sup>4</sup>, I.A. Gotsyk<sup>5</sup>

<sup>1</sup>E.O. Paton Electric Welding Institute of the NASU  
11 Kazymyr Malevych Str., 03150, Kyiv, Ukraine

<sup>2</sup>Institute of Macromolecular Chemistry of NASU  
48 Kharkiv Hwy, 02160, Kyiv, Ukraine

<sup>3</sup>Gas Institute of NASU  
39 Dekhtyarivs'ka Str., 03113, Kyiv, Ukraine

<sup>4</sup>“Naftogasbudinformatyka” Company  
5b Kudryavsky Uzviz, 04053, Kyiv, Ukraine

<sup>5</sup>“Regional Gas Company” LLC  
32/2 Princes of Ostroh Str., Kyiv, Ukraine

## ABSTRACT

The work is a study of the influence of mixtures of gaseous hydrogen with natural gas with the ratios of 10 % H<sub>2</sub>/90 % CH<sub>4</sub> and 20 % H<sub>2</sub>/80 % CH<sub>4</sub> on PE-80 polymer pipes. The paper presents the results of complex structural investigations of the material of polyethylene pipes from PE-80, which were used earlier in the operating gas distribution networks of Ukraine, after 6 months of their hydrogenation. The influence of gas mixtures on the material structure was established, which is manifested in reduction of the quantity of the crystalline phase, polyethylene crystallite dimensions and their orderliness. No changes in the chemical structure of the polyethylene pipe material were found.

**KEYWORDS:** polyethylene, PE-80, natural gas mixtures, hydrogen mixtures, hydrogen transportation

## INTRODUCTION

Existing ecological trends for substitution of natural gas as the main type of fuel for both industry as well as household consumers present new challenges for polymer materials science and science as a whole. In terms of armed aggression of the Russian Federation against Ukraine, the problem of using alternative fuel sources is currently more than relevant for both Ukraine and the world. In this work, the effect of mixtures of hydrogen with natural gas on the physical and chemical structure of the material of polyethylene pipes from PE-80 as the most widespread material in the operating gas distribution networks of Ukraine was studied. The presented results are the basis for a future large-scale study, whose aim is to study the possibility of transporting pure hydrogen and hydrogen mixtures with natural gas by gas distribution networks operating in Ukraine and the EU.

## MATERIALS

For complex studies, two gas mixtures of hydrogen with methane were used with the ratios of 10 % H<sub>2</sub>/90 % CH<sub>4</sub> and 20 % H<sub>2</sub>/80 % CH<sub>4</sub>. To study the

influence of gas mixtures on the structure of the material of polyethylene pipes using their full-scale specimens, a research bench was constructed (Figure 1). For research works, specimens of polyethylene pipes from PE-80 with an outer diameter of 63 mm, wall thickness of 3.6 mm, SDR 17.6 were selected, which served in operating gas pipelines during 15 years [1], produced by the companies LLC Plastkonstruktsiya (Figure 2, *a*) — marked further as ST1 and LLC Plastpipe (Figure 2, *b*) — marked further as ST2.

Rewelding with polyethylene thermistor plugs from PE-100 for pipes with an outer diameter of 63 mm and SDR range of 11–17 of Trans Quadro production was performed using the Optima 231 welding unit produced by LLC Terpolymergaz in accordance with acting standards and instructions for welding equipment [2].

For hydrogenation in the specified thermistor plugs piped transition pieces of the polyethylene PE-80 (with an outer diameter of 20 mm) — metal (with an outer diameter of 2/3 inches) with a milled thread were preliminary welded-in. The tightness of the joints was checked up pneumatically by a compressed air at a pressure of 8 bar.

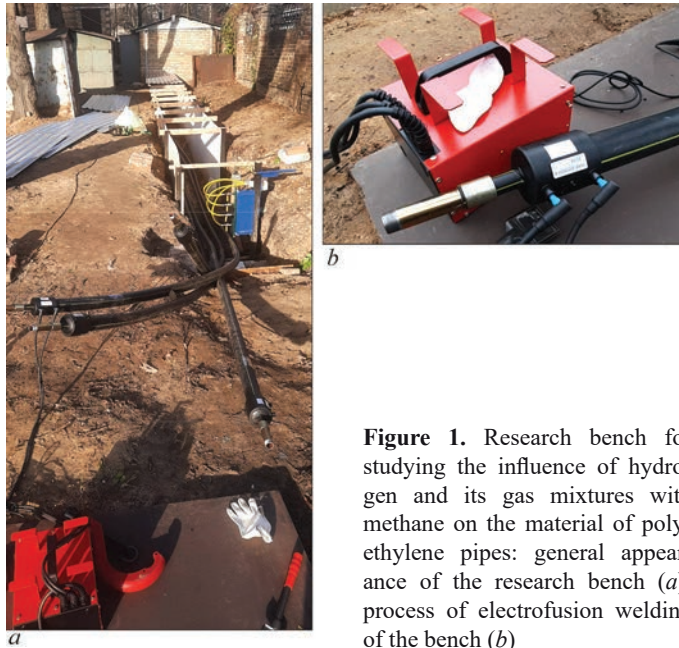


**Figure 1.** Research bench for studying the influence of hydrogen and its gas mixtures with methane on the material of polyethylene pipes: general appearance of the research bench (a); process of electrofusion welding of the bench (b)

## METHODS OF RESEARCH

For structural studies, from the walls of polyethylene pipes, specimens of 1 mm thick were cut out, as is shown in Figure 3.

Structural studies of the material of the inner surface of the wall of polyethylene pipes in a longitudinal direction to the main axis of the pipe were carried out by the method of wide-angle scattering of X-rays on reflection by means of the X-ray diffractometer XRD-7000 (Shimadzu, Japan) according to the X-ray Bragg–Brentano scheme on reflection of the primary beam by the tested specimen using  $\text{CuK}_\alpha$ -radiation ( $\lambda = 1.54 \text{ \AA}$ ) and a graphite monochromator. The study was carried out by the method of automatic step-by-step scanning in the mode of 30 kV, 30 mA in the interval of scattering angles ( $2\theta$ )  $3\text{--}60^\circ$  per exposure time of 5 s [3, 4]. The temperature of studies was  $20 \pm 2 \text{ }^\circ\text{C}$ .

The infrared spectroscopy of the material of the inner surface of the walls and the volume (at a depth of

1 mm from the inner surface of the wall) of polyethylene pipes was carried out on reflection in the Tensor 37 spectrometer with the Fourier transformation of the Bruker Corp. production (Germany) in the range of wavenumbers of  $600\text{--}3800 \text{ cm}^{-1}$  [5] at a temperature of  $20 \pm 2 \text{ }^\circ\text{C}$  in the mode for reflection on both sides of the specimens. According to the certificate of the device, the relative measurement error was  $<2 \%$ . At the second stage of works, polyethylene pipes, hydrogenated with gas mixtures, were dehydrogenated and purged with gaseous nitrogen.

To transport specimens of polyethylene pipes with the least influence of the environment, they were vacuum packed directly at the testing ground (Figure 4), then transported to laboratories in the box, which also excluded the action of light.

## RESEARCH RESULTS.

### 4.1. X-RAY STRUCTURAL ANALYSIS

Figure 5 shows the results of X-ray structural analysis of the material of polyethylene pipes before hydrogenation. The analysis of wide-angle X-ray diffraction patterns of the specimens of polyethylene pipe material showed that they all have an amorphous crystalline



**Figure 2.** Specimens of polyethylene pipes from PE-80: ST1 (a) and ST2 (b)



**Figure 3.** Direction of cutting out sections  $\gamma$  from the walls of polyethylene pipes for structural and thermophysical studies



Figure 4. Specimens of vacuum packed polyethylene pipes for structural studies

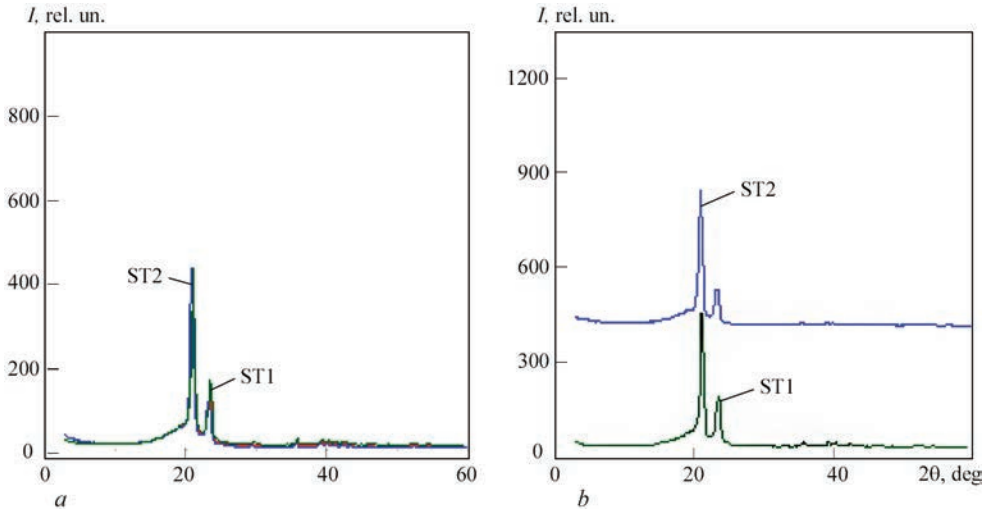


Figure 5. Wide-angle diffraction curves of X-ray structural analysis of the material of polyethylene pipes before hydrogenation (a) and their comparative diagram (b):  $I$ , rel. un. — relative intensity of reflected X-ray beam

structure, which is indicated by the presence of crystalline diffraction maxima on the background of imaginary amorphous halo with a vertex at  $2\theta_{\max} \approx 20^\circ$  [6].

The relative level of crystallinity ( $X_{cr}$ ) of the studied polymer specimens was calculated by the Matthew's method [7]:

$$X_{cr} = Q_{cr} / (Q_{cr} + Q_{am}) \cdot 100, \quad (1)$$

where  $Q_{cr}$  is the area of diffraction maxima that characterize the crystalline structure of the polymer;  $Q_{cr} + Q_{am}$  is the area of the entire diffraction pattern in the interval of scattering angles ( $2\theta_1 \div 2\theta_2$ ), in which the amorphous crystalline structure of the polymer is revealed.

The results of the calculation of the degrees of crystallinity of the material of polyethylene pipes are given in Table 1. The evaluation showed that for the specimen of the ST1 polyethylene  $X_{cr} = 63.18\%$ , and for the specimen and ST2  $X_{cr} = 62.38\%$ .

The evaluation of effective size of crystallites ( $L$ ) of the specimens was carried out by the Scherrer method [8]:

$$L = K\lambda(\beta \cos\theta_{\max})^{-1}, \quad (2)$$

where  $K$  is the constant associated with the shape of crystallites (their shape being unknown  $K = 0.9$ ), and  $\beta$  is the angular half-width (width at a half of the height) of the diffraction maximum, showed that the

average value  $L \approx 17.22$  nm and  $14.39$  nm for ST1 and ST2, respectively. The size of the crystallites by individual diffraction maxima for ST1 and ST2 specimens is given in Tables 2, 3, respectively, where FWHM is the full width at a half of the maximum (width of the spectral curve, measured between those points on  $Y$  axis, which are the half of the maximum amplitude), FWHM tot. is the total full width at a half of the maximum, FWHM instr. is the instrumental full width at a half of the maximum.

The results of X-ray structural analysis of the material of polyethylene pipes after 6 months of hydrogenation are shown in Figure 6. It was established that specimens of polyethylene pipes ST1 and ST2, which were under the action of gas mixtures, as well as the initial specimens, are characterized by amorphous crystalline structure, which is indicated by the presence of crystalline diffraction maxima on the background of an imaginary amorphous halo with a vertex at  $2\theta \approx 20^\circ$ . It was found that under the action of gas

Table 1. Degree of crystallinity of the material of polyethylene pipes, calculated according to the data of X-ray structural analysis

Specimen	$X_{cr}$ , %	$L$ , nm
ST1	63.18	17.22
ST2	62.38	14.39

**Table 2.** Sizes of crystallites according to diffraction maxima of ST1 pipe specimen

2θ, deg	d, Å	Attempts	FWHM tot., deg	FWHM instr., deg	FWHM of the specimen, deg	Size of crystallites, Å
21.100	4.2106	19324	0.4000	0.1303	0.2697	299.9
23.500	3.7858	10260	0.6000	0.1303	0.4697	172.9
29.700	3.0081	640	0.8000	0.1267	0.6733	122.2
35.800	2.5083	899	0.6000	0.1132	0.4868	171.6
39.300	2.2926	1127	0.8000	0.1074	0.6926	121.9
40.300	2.2380	2986	2.6000	0.1059	2.4941	43.0
42.500	2.1271	692	0.8000	0.1029	0.6971	122.4
46.400	1.9570	428	0.8000	0.0984	0.7016	123.3
52.600	1.7400	607	0.8000	0.1011	0.6989	126.9

**Table 3.** Sizes of crystallites according to diffraction maxima of ST2 pipe specimen

2θ, deg	d, Å	Attempts	FWHM tot., deg	FWHM instr., deg	FWHM of the specimen, deg	Size of crystallites, Å
20.900	4.2505	29650	0.6000	0.1313	0.4697	172.1
23.250	3.8259	7690	0.6000	0.1313	0.4697	172.8
35.550	2.5253	534	0.4000	0.1137	0.2863	291.6
39.100	2.3039	800	0.8000	0.1077	0.6923	121.9
40.050	2.2514	462	0.6000	0.1063	0.4937	171.9
40.950	2.2039	557	0.9000	0.1050	0.7950	106.8
42.300	2.1367	529	0.8000	0.1032	0.6968	122.3

mixtures in the material of polyethylene pipes, their crystalline structure changes, in particular, new crystalline peaks appear at  $2\theta_{max} \approx 15.9^\circ$ , as well as the intensity of peaks grows at  $2\theta_{max} \approx 29.5^\circ$  and  $35.5^\circ$ , which is associated with an increase in the crystallinity of polyethylene [9]. It was established that the relative degree of crystallinity  $X_{cr}$  of the material of polyethylene pipes ST1 and ST2, which were under the action of gas mixtures 10 % H<sub>2</sub>/90 % CH<sub>4</sub> and 20 % H<sub>2</sub>/80 % CH<sub>4</sub> respectively, is higher compared to the source material (Table 4).

The analysis of the results of X-ray structural analysis showed that under the action of gas mixtures, the crystalline structure changes, in particular, the average size of crystallites L is reduced (specimens of ST1 and ST1 10 % H<sub>2</sub>). For calculations, diffraction maxima at  $2\theta_{max} \approx 21.0^\circ$  and  $23.4^\circ$  were used. The size of crystallites and interplanar distances at individual diffraction maxima for the specimens of ST1 10 % H<sub>2</sub> and ST2 20 % H<sub>2</sub>, which were under the action of gas mixtures of 10 % H<sub>2</sub>/90 % CH<sub>4</sub> and 20 % H<sub>2</sub>/80 % CH<sub>4</sub> respectively, are given in Tables 5, 6.

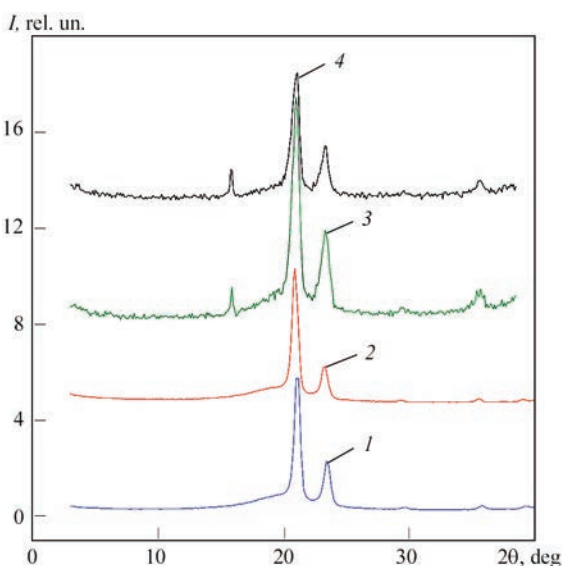
**4.2. INFRARED SPECTROSCOPY**

Figure 7 shows the spectra of infrared (IR) spectroscopy of the material from the inner surface and volume of walls of the specimens of ST1 (Figure 7, a), ST2 (Figure 7, b) pipe before hydrogenation.

It is seen that the absorption spectra for all the specimens are similar and typical of polyethylene. However, it is necessary to focus the attention here on the appearance of additional absorption lines on the spectra of the specimen material from the inner surface of the walls of ST1 and ST2 pipes compared

**Table 4.** Degree of crystallinity of the material of polyethylene pipes, calculated according to data of X-ray structural analysis

Specimen	$X_{cr}$ , %	L, nm
ST1	63.18	17.22
ST2	62.38	14.39
ST1 10 % H <sub>2</sub>	68.91	13.19
ST2 20 % H <sub>2</sub>	76.01	15.81



**Figure 6.** Comparative diagram of wide-angle diffraction curves of X-ray structural analysis of material of polyethylene ST1 and ST2 pipes before and after hydrogenation: 1 — ST1; 2 — ST2; 3 — ST1 10 % H<sub>2</sub>; 4 — ST2 20 % H<sub>2</sub>

**Table 5.** Sizes of crystallites according to diffraction maxima of ST1 specimen 10 % H<sub>2</sub>

2θ, deg	<i>d</i> , Å	Attempts	FWHM tot., deg	FWHM instr., deg	FWHM of the specimen, deg	Size of crystallites, Å
17.250	5.1386	8	0.2000	0.1303	0.0697	1153.7
22.400	3.9658	821	0.7000	0.1303	0.5697	142.3
24.750	3.5943	321	0.8000	0.1303	0.6697	121.5
37.050	2.4246	61	0.8000	0.1110	0.6890	121.7

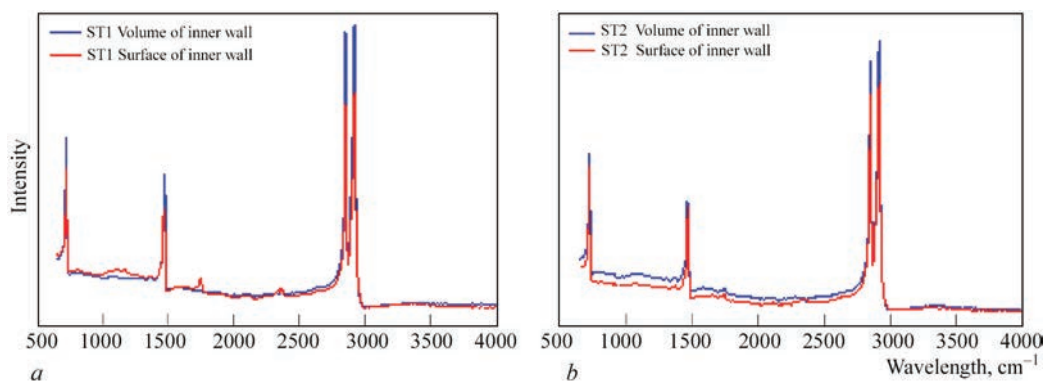
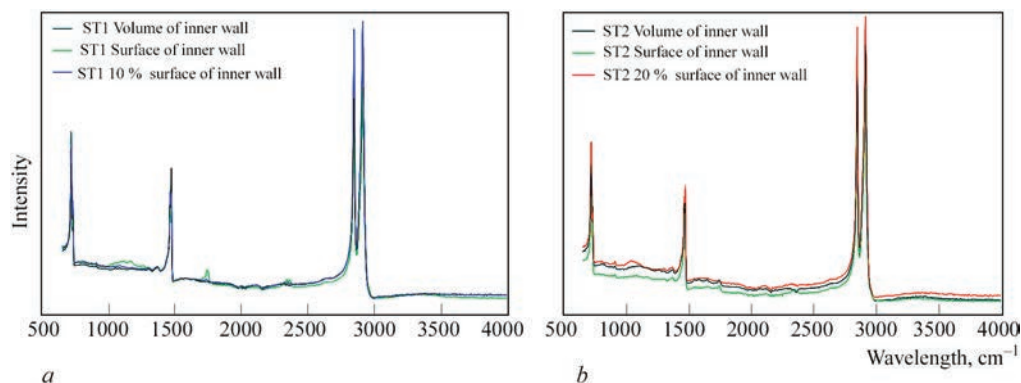
**Table 6.** Sizes of crystallites according to diffraction maxima of ST2 specimen 20 % H<sub>2</sub>

2θ, deg	<i>d</i> , Å	Attempts	FWHM tot., deg	FWHM instr., deg	FWHM of the specimen, deg	Size of crystallites, Å
17.250	5.1355	21	0.2000	0.1303	0.0697	1153.7
22.450	3.9571	269	0.4000	0.1303	0.2697	300.5
24.700	3.6012	149	0.6000	0.1303	0.4697	173.3
37.050	2.4245	47	0.8000	0.1110	0.6890	121.7
39.000	2.3076	6	0.4000	0.1078	0.2922	288.7

to the spectra of the material from the volume of the walls of these pipes. The presence of absorption lines near the wavelength of 2400 cm<sup>-1</sup>, which are responsible for oscillations of CO<sub>2</sub> groups, may be an artefact of measurements, which is associated with the environment and carbon dioxide present in it. The emergence of new abovementioned absorption lines in the specimens from the inner surface of the walls of ST1 and ST2 pipes and their absence in the specimens from the volume of the walls of these pipes may indicate a certain effect of natural gas, which for 15 years

was transported through these pipes, on the chemical structure of polyethylene, from which ST1 and ST2 pipes are manufactured. This fact should be taken into account during further studies of all the pipes after the next stages of work, i.e. after their hydrogenation.

The results of infrared spectroscopy after 6 months of hydrogenation are presented in Figure 8. From the comparative IR spectra before and after 6 months of hydrogenation of the specimens of all materials of polyethylene pipes, it is seen that the chemical structure of polyethylene did not undergo changes that follows


**Figure 7.** IR spectra of the material of the inner surface and volume of the walls of pipe specimens before hydrogenation: *a* — ST1; *b* — ST2

**Figure 8.** Comparative IR spectra of the material of the inner surface and volume of the walls of pipe specimens before and after hydrogenation: *a* — ST1 (10 % H<sub>2</sub>/90 % CH<sub>4</sub>); *b* — ST2 (20 % H<sub>2</sub>/80 % CH<sub>4</sub>)

from the absence of new peaks or displacement of existing peaks responsible for chemical bonds or groups of atoms. It is worth noting that after hydrogenation, the spectra from the surface of the inner wall of the pipe specimens being in operation, are similar to the spectra of the specimens of the material of these pipes from the volume, i.e., it can be said that the chemical structure of the material of the surface of these pipes became identical to the structure of the volume material.

Separately it should be noted that on the spectra of the specimens under the action of the gas mixture of 20 % H<sub>2</sub>/80 % CH<sub>4</sub>, the intensity of peaks in the wavelength range of 1000–1200 and 3300–3500 cm<sup>-1</sup>, which are responsible for the oscillations of the C–O–H and –OH groups grows, that can indicate a certain interaction of hydrogen molecules with polymer chains of polyethylene, probably of a dipole in nature with their lateral groups of atoms [10].

## CONCLUSIONS

In the work, complex investigations of the influence of gas mixtures of hydrogen with methane with two ratios of 10 % H<sub>2</sub>/90 % CH<sub>4</sub> and 20 % H<sub>2</sub>/80 % CH<sub>4</sub> on the physical and chemical structure of the material of polyethylene pipes from PE-80, which served in the operating gas distribution networks of Ukraine for 15 years were carried out.

It was established that pipe materials, that were in operation for 15 years have undergone certain structural changes, probably under the action of natural gas, which is manifested in the reduced number of crystalline phase and sizes of crystallites of polyethylene, as well as in the emergence of additional chemical groups in the material of the inner pipe surface.

The presence of influence of gas mixtures of 10 % H<sub>2</sub>/80 % CH<sub>4</sub> and 20 % H<sub>2</sub>/80 % CH<sub>4</sub> on the crystalline phase was established. A decrease in the sizes of polyethylene crystallites and their orderliness under the action of gas mixtures in the volume of pipes was found. At the same time, the emergence of crystallites of a new shape was found on the surface of the inner wall of the pipes. The influence of gas mixtures on the material of polyethylene pipes has a physical nature.

Changes in the chemical structure of the material of polyethylene pipes were not detected.

## REFERENCES

- Byrne, N., Ghanei, S., Manjarres Espinosa, S., Neave, M. (2023) Influence of hydrogen on vintage polyethylene pipes: Slow crack growth performance and material properties. *Inter. J. of Energy Research*, Vol. 2023, Article ID 6056999. DOI: <https://doi.org/10.1155/2023/6056999>
- Iurzhenko, M.V., Shestopal, A.M., Hochfeldel, V.L. at al. (2018) *Dictionary-handbook on welding and gluing of plastics*. Ed. by B.E. Paton. Kyiv, Naukova Dumka [in Ukrainian].
- Lipatov, Yu.S., Shilov, V.V., Gomza, Yu.P., Kruglyak N.E. (1982) *X-ray research methods of polymers*. Kyiv, Naukova Dumka [in Ukrainian].
- Kratky, O., Pilz, I., Schmitz, P.J. (1966) Absolute intensity measurement of small-angle X-ray scattering by means of a standard sample. *J. Colloid Interface Sci.*, 21(1), 24–34.
- Matkovska, M.V., Iurzhenko, Ye.P., Mamunya, V. et al. (2018) *Chapter 11. Structure and electrical/dielectric properties of ion-conductive polymer composites based on aliphatic epoxy resin and lithium perchlorate salt*. Springer Proceedings in Physics. Nanochemistry, Biotechnology, Nanomaterials, and Their Application, Cham, Switzerland, Springer International Publ., 177–203.
- Galchun, A., Korab, N., Kondratenko, V. et al. (2015) Nanostructurization and thermal properties of polyethylenes' welds. *Nanoscale Res. Lett.*, 10. DOI: <https://doi.org/10.1186/s11671-015-0832-4>
- Stoppel, V.I., Kercha, Yu.Yu. (2008) *The structure of linear polyurethanes*. Kyiv, Naukova dumka [in Russian].
- Ginye, A. (1961) *Radiography of crystals. Theory and practice*. Moscow, Fizmatgiz [in Russian].
- Demchenko, V., Iurzhenko, M., Shadrin, A. et al. (2017) Relaxation behavior of polyethylene welded joints. *Nanoscale Res. Lett.*, 12. DOI: <https://doi.org/10.1186/s11671-017-2059-z>
- Kloppfer, M.-H., Berne, P., Espuche, E. (2015) Development of innovating materials for distributing mixtures of hydrogen and natural gas. Study of the barrier properties and durability of polymer pipes. *Oil & Gas Science and Technology — Rev. IFP Energies Nouvelles*, 70(2), 305–315. DOI: <https://doi.org/10.2516/ogst/2014008>

## ORCID

M.V. Iurzhenko: 0000-0002-5535-731X,  
M.O. Kovalchuk: 0000-0003-2161-643X,  
V.Yu. Kondratenko: 0009-0003-3521-9639,  
V.L. Demchenko: 0000-0001-9146-8984

## CONFLICT OF INTEREST

The Authors declare no conflict of interest

## CORRESPONDING AUTHOR

M.V. Iurzhenko  
E.O. Paton Electric Welding Institute of the NASU  
11 Kazymyr Malevych Str., 03150, Kyiv, Ukraine.  
E-mail: 4chewip@gmail.com

## SUGGESTED CITATION

M.V. Iurzhenko, M.O. Kovalchuk, V.Yu. Kondratenko, V.L. Demchenko, K.G. Gusakova, V.S. Verbovskyi, G.V. Zhuk, K.P. Kostogryz, I.A. Gotsyk (2023) Influence of hydrogen-methane gas mixtures on the physical and chemical structure of polyethylene pipes of the operating gas-distribution networks of Ukraine. *The Paton Welding J.*, 6, 49–54.

## JOURNAL HOME PAGE

<https://patonpublishinghouse.com/eng/journals/tpwj>